Steels for nuclear reactors: Eurofer 97

Monteiro De Sena Silvares de Carvalho, Ines

DOI
10.4233/uuid:a3e32a8c-bc0a-497d-9666-15ec44f2e5c2

Publication date
2016

Document Version
Final published version

Citation (APA)
Monteiro De Sena Silvares de Carvalho, I. (2016). *Steels for nuclear reactors: Eurofer 97*. [Dissertation (TU Delft), Delft University of Technology]. https://doi.org/10.4233/uuid:a3e32a8c-bc0a-497d-9666-15ec44f2e5c2

Steels for nuclear reactors: Eurofer 97

Inês Carvalho

Steels for nuclear reactors:

Eurofer 97

Inês Carvalho

Steels for fusion reactors: Eurofer97

Proefschrift

ter verkrijging van de graad van doctor
aan de Technische Universiteit Delft,
op gezag van de Rector Magnificus prof. ir. K. Ch. A. M. Luyben,
voorzitter van het College voor Promoties,
in het openbaar te verdedigen op
vrijdag 23 september 2016 om 15:00 uur

door

Inês MONTEIRO DE SENA SILVARES DE CARVALHO
Master of Science,
University of Aveiro, Portugal
geboren te Viseu, Portugal

This dissertation has been approved by the
promotor: Prof. dr. ir. J. Sietsma
copromotor: Dr. H. Schut

Composition of the doctoral committee:

Rector Magnificus	Chairman
Prof. dr. ir. J. Sietsma	Delft University of Technology
Dr. H. Schut	Delft University of Technology
Dr. A. Fedorov	Nuclear Research and consultancy Group, The Netherlands

Independent members:

Prof. dr. C. Pappas	Delft University of Technology
Prof. dr. ir. L. Kestens	Ghent University, Belgium
Dr. M-F. Barthe	French National Research Center, France
Dr. E. Gaganidze	Karlusruher Institute of Technology, Germany

Reserve member:

Prof. dr. I. M. Richardson	Delft University of Technology

Dr. A. Fedorov and dr.ir. N. Luzginova have contributed greatly to the realization of this dissertation as supervisors.

This research was carried out under project number M74.5.10393 in the framework of the Research Program of Materials innovation institute (M2i) in the Netherlands (www.m2i.nl)

Published by Uitgeverij BOXpress || proefschriftmaken.nl
ISBN: 978-94-91909-40-5

Or did you not think so far ahead?
'Cause I've been thinkin' 'bout forever

— Frank Ocean

Contents

Chapter 4 Characterization of Eurofer97 in reference state by positron annihilation 71

Chapter 5 He implantations: the first step to understand defect creation in Eurofer97 81

Summary

These days, climate change and its consequences regularly make the news. Sea levels are rising, poles are defrosting, species are becoming extinct, the ozone layer is being destroyed and the earth's temperature is increasing. These symptoms convey a clear call to action: the preservation of the environment needs to be of the highest concern. In parallel, the world's population grows larger and energy consumption grows with it. With these worries in mind, more attention is put on how to be more earth-minded and environment friendly. Often, this attention has a common theme: the need for renewable energies. Large investments have been made towards the development of renewable sources of energy such as solar and wind power. However, the energy demand is so high that an extra source of power is needed, for which nuclear power is a candidate.

Nuclear power is already available from fission reactors. Unfortunately, the waste from fission reactors is highly radioactive and requires constant surveillance. Furthermore, in case of an accident uncontrolled chain reactions might take place. Fusion energy, once fully developed, will be the better option as no waste is produced (the materials that become active during operation can be recycled in 100 years' time) and no chain reactions will take place in the case of an accident, which makes fusion reactors inherently safer. But the development of fusion reactor puts a high demand on materials, as these must withstand high radiation levels, high transmutation rates, high temperatures and high thermo-mechanical stresses.

The material studied in this thesis is Eurofer97 steel, which will be used for structural components in fusion reactors. This work is focused on the evolution of irradiation induced defects, as well as on the synergy with transmuted He in the matrix once this steel is subject to operational conditions. As helium has a low solubility in ferrite and tends to form clusters that can persist in the matrix over long periods of time, the detriment of the mechanical properties of the steel is expected. The extreme conditions for the application of Eurofer97 make the development and characterization of structural materials for nuclear reactors important topics of research. At the moment it is not possible to irradiate Eurofer97 with a fusion spectrum. This practical limitation led to two parallel studies: on one hand Eurofer was He implanted in order to study the defects to which He is likely to bind to, on the

other hand Eurofer was neutron irradiated and the defect structures formed in the irradiation are identified. The questions raised for this experimental work are the following:

- Which defects are formed during He implantation of Eurofer97? How do these defect structures evolve at different temperatures?
- Which defect structures are formed during neutron irradiation of Eurofer97? How do these defect structures evolve at different temperatures?
- Mechanical properties are of the most importance for Eurofer97 steel. Can the measured irradiation hardening be explained on the basis of the defects observed in irradiated Eurofer97? How effective are these defects to impede the dislocation gliding?

The experimental work presented in this thesis is divided into three chapters. The first experimental chapter, chapter 4, provides information on the reference conditions of Eurofer steel (manufacturing conditions). For this work, a Eurofer sample was step annealed up to 1600 K and after each annealing step the defect structure was analyzed with positron annihilation Doppler broadening (PADB). The measurements were done after oven cooling of the samples, at room temperature. At 300 K Eurofer97 is in the as-received condition, with a tempered martensitic microstructure containing defects and carbides. As the annealings begin, the material microstructure changes to ferrite (α, bcc) up to an annealing temperature of 1100 K. As the temperature increases the density of defects present in the matrix is progressively reduced. In the annealing step from 1100 K to 1200 K the microstructure changes to austenite (γ, fcc). However, the oven cooling rate of 8 K/min promotes the formation of a martensitic microstructure upon cooling. At 1200 K the carbides present in the matrix will dissolve and grain growth is expected. The formation of a martensitic microstructure (bct) is accompanied by the formation of dislocations. After annealing at 1400 K and 1600 K, the martensitic microstructure (after cooling) persists. From the analysis of the PADB curves it is concluded that at 1200 K the majority of the defects present in Eurofer97 are annealed. By comparing the PADB results obtained for Eurofer97 with those of pure Fe at 300 K and after annealing at 1200 K for 1 h, it can be concluded that as the annealing temperature of

Eurofer97 increases, the concentration of defects present in the matrix becomes increasingly similar to that of pure Fe.

Chapter 5 shows the outcome of the helium implantation studies in Eurofer97, in order to reproduce the transmutation of He in the material. Eurofer97 was plasma and ion beam implanted. The implanted material was studied with PADB and thermal desorption spectroscopy (TDS).

For the plasma implantations, two sets of samples were studied: set A, with samples in the as-received condition, and set B, containing samples that were annealed at 1200 K for 1 h. The choice of the annealing temperature of set B is based on the results obtained with the work discussed in chapter 4. The implantations were done with an energy of 3 keV and doses of 10^{18}-10^{19} He/cm^2. Within each set, one of the samples was implanted at a low temperature (375 K) and the other at a higher temperature (450 K and 525 K, for sets A and B, respectively). Set A shows a decrease of the *S* and increase of the *W* parameter after implantation for both samples, explained by the filling of defects with He. The implantation temperature plays an important role by promoting the diffusion of He for depths above the positron probing range. This effect is accentuated for the samples implanted at higher temperatures and, considering that the low density of defects for the samples in set B, explaining the similar *S* and *W* values before and after implantation. The TDS study shows that the samples implanted at 375 K release the majority of the trapped He at temperatures below 1000 K, while the samples implanted at higher temperatures shows a greater release above that temperature.

The ion implantations were done at room temperature with energies of 350 keV, 500 keV and 2 MeV, and doses in the range 10^{14}-10^{17} He/cm^2. PADB measurements were performed on the implanted samples after step annealing to 1500 K. The PADB measurements were done at room temperature. The information obtained with the two analysis techniques, PADB and TDS, was correlated. After implantation, two types of defect structures are identified: vacancy clusters and helium-vacancy clusters (He_nV_m clusters). Vacancy clusters are annealed at temperatures below 800 K. In parallel, He_nV_m clusters with a helium-per-vacancy ratio ($\frac{He}{V}=\frac{n}{m}$) above ~ 4 dissociate (dissociation energies below ~ 2.4 eV) and He is released into the matrix. The released He can be detected by the quadrupole of the TDS system or be retrapped in defect clusters with higher dissociation energy. As the annealing temperature increases to 1000 K, the release of He from He_nV_m clusters with a He/V ratio in the range ~ 3 - 4 is expected. In the annealing step from 1000 K to 1200 K, the phase transition of Eurofer takes place. The phase transition is accompanied by a reorganization of the grain boundaries, which leads to a decrease of defect structures in the matrix. The calculated E^d values for this temperature step are in the range ~ 2.9 - 3.3 eV, identified in the literature as the dissociation of He_nV_m clusters with He/V ratio of ~ 1.8, likely to be He_2V. Above 1200 K Ostwald ripening and/or coalescence phenomena take place and the formation of bubbles (large defect clusters with a low He/V ratio) is expected. Starting at 1300 K the release of He from bubbles is expected. However, the phenomena involved are not clear, possibly being bubble dissociation and/or bubble diffusion mechanisms. The evolution of defects above described answers the first question raised for the experimental work: which defects are formed during implantation and how do they evolve with increasing temperature.

Overall, the TDS results obtained with plasma implanted samples are in agreement with that of the ion-beam implantations. The peaks of the TDS spectra observed at 900 K and 1200 K, and release of He above 1300 K, are common aspects to all implanted samples. In the spectra of the plasma implanted material, two additional peaks are observed: one at 600 K and another at 1100 K. These peaks are not clearly observed in the spectra obtained for the ion beam samples but their presence is under discussion. The similarities found in the TDS results indicate that although the implantation temperature plays an important role in the He release, the phenomena behind it are the same for plasma and ion-beam implanted samples.

Chapter 6 presents the work done with neutron irradiated Eurofer97. Eurofer97 was irradiated at three different conditions: 2.4 dpa and 333 K, 1.9 dpa and 573 K, and 8.0 dpa and 573 K. After irradiation, Eurofer97 steel was studied with transmission electron microscopy (TEM) and mechanically tested. The TEM micrographs allow the identification of the defects present in the matrix after irradiation and their evolution with temperature and dose. From the tensile measurements, conclusions are taken regarding the observed irradiation hardening and the obstacle strength, a parameter reflecting the effectiveness of the obstacle in stopping a dislocation in motion. The irradiation hardening study answers the third question raised for the research discussed in this thesis. The microscopy observations and the tensile measurements are correlated in this chapter.

After neutron irradiating Eurofer at 333 K with 2.4 dpa, black dots (irradiation induced defects) were observed with the laths. These defects have an average size of 7 nm. A study of the sample irradiated with 1.9 dpa at 573 K reveals the presence of irradiation damage as black dots and dislocation loops. Considering that dislocation loops can be misinterpreted as black dots due to their position in relation to the electron beam of the microscopy, no clear defect size distinction can be made. The distribution of defect dimension in this sample (independently of their character) has a bi-modal shape with a maxima located at 9 nm and at 17 nm. At the moment, no justification can be found for this size distribution.

A comparison of the defect sizes of the first two irradiation conditions leads to the conclusion that defect size increases with increasing temperature. This effect is likely associated with the higher irradiation temperature of 573 K that promotes the coalescence of defects and the aggregation of newly formed Frenkel pairs to the existing defects.

For the third irradiation condition, 8.0 dpa at 573 K, the defects observed are again black dots and dislocation loops. In this sample, the average size of the defects (independently of their character) is 4 nm. A comparison of the defect sizes of the second and the third irradiation conditions allows the conclusion that the defect size decreases with increasing irradiation dose, for a constant irradiation temperature. The decrease of defect size is related to the breaking of the dislocation loops by vacancies and interstitials generated by the increased number incoming neutrons. This section answers the second questions raised for the experimental work: which defects are formed during neutron irradiation and how do these evolve with temperature.

The tensile measurements of samples irradiated at 333 K show a hardening curve that reaches a plateau at a dose of ~ 0.3 dpa, lasting until 2.5 dpa. The plateau observed indicates that the thermal spike of defects initiated by the neutron irradiation of the matrix is not enough to allow the recovery of the material, leading to a saturation of the defects in the lattice. The tensile measurements of the samples irradiated at 573 K show a continuous increase of hardening up to 10 dpa and at that dose no hardening saturation is yet noticed. In this case, the continuous increase of hardening is explained by the increased irradiation temperature that promotes thermally activated recombination of defects and allows partial recovery of the material. The hardening rate of the samples irradiated at 333 K is 1.5x faster than the hardening rate at 573 K.

The obstacle strength value is a parameter of the irradiation hardening equation discussed in chapter 6. This parameter was calculated based on the defects observed with TEM, independently of the defect character. The method used relies on the calculation of the increase of yield strength after irradiation. This increase (irradiation hardening) was calculated using two methods to determine the inter-obstacle strength: one based on the dispersed barrier hardening model and the other based on the effective inter-particle spacing. In the analysis of the relation between irradiation defects on the yield strength the different types of defects (black dots, dislocation loops) are assumed to have the same effect, since no distinction can be made on the basis of the yield strength as a single parameter characterising the mechanical behaviour. For the same reason the effect of defect size cannot be analysed. By plotting the calculated yield strength for various obstacle strength values, it is concluded that the effective inter-particle spacing method leads to stable values of the obstacle strength parameter, with a value of 0.22. This indicates that the obstacle strength parameter is neither dependent on the size of the obstacle nor on the damage level of the sample. This value is in agreement with the work done by other authors. Using an obstacle strength value of 0.22, the irradiation hardening values can be explained in the light of the irradiation induced defects observed with TEM. This answers the second question answers the third question raised for the experimental work: can the irradiation hardening be explained on the basis of the defects observed with TEM and how effective are these defects in stopping the dislocation gliding.

The presence of He bubbles in the irradiated material was a point of interest, as the transmutation of He is detrimental for the mechanical properties of Eurofer. The TEM observations do not reveal the presence of bubbles in Eurofer. Using the ideal gas law, the number of formed He bubbles in a defined area similar to that observed with TEM was calculated. For the sample irradiated at 8.0 dpa, in which the highest transmutation values are expected, the number of bubbles expected to be observed in a volume of 1.5 x 10^{-14} cm^3 is 12. Considering that all interstitial He will leave the sample at the irradiation temperature, and that with increasing irradiation temperature some of the helium-vacancy clusters dissociate (as their dissociation energy is reached) before microscopic observation, the lack of bubbles in the TEM observations seems to be correct.

To further investigate the presence of He in the neutron irradiated Eurofer97, TDS measurements were carried out using TEM samples. Although the background signal interfered with the measurement of the 8.0 dpa, 573 K sample, it is possible to conclude that for the 1.9 dpa, 573 K sample less than 43 % of the transmuted helium during neutron irradiation is retained. This conclusion is in accordance with the idea that Eurofer97 is a step forward in the development of radiation resistant structural steels.

In conclusion, the work discussed in this thesis is a step forward in the identification of the defects formed during neutron irradiation. Furthermore, the dissociation of He from implanted material sheds light on the evolution of the He traps with increasing temperature. The irradiation hardening noticed for Eurofer97 is discussed based on the microscopy observations and a conclusion is reached regarding the strength of defects in stopping the dislocation gliding. The TDS results obtained with neutron irradiated Eurofer97, if developed further, can be an indicator for the comparison between He implantation and neutron irradiation and help improving helium transmutation calculations. This work aims to be an experimental contribution for the understanding of the behavior of Eurofer97 in a neutron fusion environment.

Chapter 1

Introduction

1.1 Future energy with reduced carbon emission

The scenario of future energy consumption is an alarming omen for the generations to come: as the world's population grows and the average living standard gets higher, the need for energy is ever increasing. It is expected that the energy demand will increase tremendously in the future, possibly quadrupling by 2100 [1].

Fossil fuels are the primary option when it comes to power generation as they are easily available. But at what cost should the use of fossil fuels continue? The global production of CO_2 has reached a record of 35.5 billion tonnes in 2013 [2] and the emission of pollutant gases has a measurable impact on the planet's temperature, affecting ecosystems around the globe.

As the public awareness of gas emissions and global warming increases, renewable energy has become a topic for extensive research. Take, for example, the commonness of wind turbines and solar cells, with the latter being available to the general public for installation in private houses. Although highly dependent on the weather and the ability to store the generated energy for later use, renewable energy technologies are definitely to be considered and to be made use of. But even so, renewable energies (and new technologies in general) take a long time being implemented due to the scale of the investments needed and the lack of related legislation [3].

The European Strategic Energy Technology Plan (SET-Plan) [3] has well-defined ambitions for the year 2020 (Horizon2020 program [4]) regarding the emission of greenhouse gases and energy production in Europe. Examples are the binding targets to reduce greenhouse gas emissions by 20%, to ensure 20% of renewable energy sources in the EU energy mix, and to reduce the EU primary energy use by 20%. The way defined to meet these targets is to reduce the costs of clean energy, and to invest in the energy technology sector [3]. The highest priorities are given to wind, solar and bio technologies, breakthroughs in CO_2 capture, generalizing efficient energy conversion systems in buildings and transport, and research in nuclear energy for fission and fusion energy. A varied energy mix is essential: it provides competitiveness between industries in the search of optimized technologies and lower costs for the final user.

1.2 Fusion energy technology

Although renewable energy sources are promising, the production of energy is not constant and depends on the weather conditions. Nuclear power is an ideal support for the necessary energy production. With a nuclear reactor it is possible to generate constant power and to provide a stable base load of energy. When using a nuclear reactor in parallel to renewable energies, it is possible to decrease the energy production of the nuclear power plant when sufficient renewable energy is available, or to increase it when the demand is higher. Besides that, nuclear energy does not produce gas emission and therefore does not aggravate global warming.

There are two methods to generate power from nuclear energy: fission reactions and fusion reactions. In nuclear fission there is splitting of nuclei promoted by the interaction of the nucleus with neutrons. The resulting nuclear masses are lower than the initial one and the difference is released as energy. The fuel used in fission reactions, which is the technology used in current nuclear power plants, is usually uranium or plutonium, both elements being radioactive and fissile. Fusion energy results from the fusion of two atom nuclei that, in an environment with a temperature of millions of degrees centigrade, collide at very high speed and form a new type of atom. As in the previous case, the resulting mass is lower than the total mass of the parent nuclei and the difference is released as energy.

The nuclear waste of fission power plants is primarily the leftover product after the nuclei of the fuel have split. This waste is highly radioactive and hot, requiring cooling and shielding. Its disposal is done at controlled locations that need to be under constant surveillance. On the contrary, no radioactive fuel waste will be produced in fusion technology. The only waste generated in fusion reactors consists of the materials of the reactor itself that become activated due to the interaction with neutrons. In this case, technological advances aim for the development of ‘low activation’ materials whose chemical composition is carefully selected so that they will not become radioactive. After decaying to low radioactivity level, the materials can be recycled.

Fusion energy is an interesting source of power for various reasons: the fuels are broadly available and are nearly unlimited, it does not yield greenhouse gases, it is safe (no chain reaction will take place in the case of an accident) and, with the proper choice of structural materials that allow the radioactivity decay in 100 years’ time, it will also be environmentally responsible [5]. Multiple institutions of the EU are working on fusion technology related topics and the common effort is essential to realize fusion electricity by 2050 [6]. Fusion technology is one of the key EU technology challenges for the next 10 years [3]. It has two main aims [5]: the preparation of ITER experiments (the international project to design and build an experimental fusion reactor) and the development of concepts to be used at DEMO (DEMOnstration power plant, the step between ITER and a commercial power plant).

Fusion energy is based on the fusion of deuterium and tritium. This reaction leads to the formation of neutrons and helium nuclei, and the release of 17.6 MeV of energy. The fusion reaction requires temperatures above 100 million degrees centigrade with minimal thermal loss. To sustain that temperature, the plasma must be kept away from the reactors walls via magnetic fields. The internationally preferred design of a fusion reactor is the tokamak, a doughnut shaped vacuum vessel used to contain the plasma with magnetic fields, making the plasma particles to run in spirals without touching the walls. Fusion energy is not a new research topic of interest and multiple tokomak facilities have been built over Europe to test the principles of fusion energy – JET, JT-60, ASDEX, Tore Supra, W7X [5]. These facilities enabled research to study design choices and plasma operation conditions, but questions regarding the neutron irradiation of materials and its consequences for the materials surrounding the fusion reaction – transmutation and retention of gases, alteration of mechanical properties, irradiation induced defects – still remain. Besides material related issues, substantial innovation is necessary regarding the magnets controlling the plasma, microwave and high power beam sources (used to heat the plasma), remote handling and fueling [5].

Fusion energy still has many challenges ahead. Steady plasma regimes of operation must be developed further [5]. To maximize the fusion reaction gain, minimum energy losses must be achieved. This challenge is correlated to materials development as the losses must comply to the acceptable heat loads of the plasma facing materials [5]. Neutron resistant materials are vital for the development of DEMO and a commercial power plant. Although Eurofer97 steel, the material discussed in this thesis, has shown reliable mechanical properties to be used as a structural steel, further developments are necessary to increase its operational temperature [5]. Since the final goal for the fusion reactor is to be self-sufficient and the amount of tritium available in nature is limited, the breeding of tritium is necessary. The design concepts for the ideal tritium breeding blanket will be demonstrated at ITER, with one of the blankets being based on lithium and beryllium pebbles and the other on a lithium-lead fluid [5]. Finally, the engineering aspect of fusion reactors is crucial – all components must be carefully designed to avoid incompatibilities and to enable safe management of the facility.

1.3 Fusion Energy materials development

The demands for fusion materials are high: materials must withstand high radiation levels, high transmutation rates, high temperatures and high thermo-mechanical stresses. Table 1.1 shows the relevant conditions under which the structural materials of the tokomak will be subjected to in ITER and DEMO [7–9]. Although the materials used in both reactors will have to support high transmutation levels of helium (He) and hydrogen (H), materials for DEMO must withstand 5 to 8 times higher levels of damage than at ITER. These extreme conditions make the development and characterization of plasma facing and structural materials very important topics for design and application at the reactors. Good physical and mechanical properties, such as good creep strength and fatigue resistance, minimum embrittlement due to transmutation products, corrosion resistance and low activation are necessary.

Table 1.1 *Material relevant conditions at ITER and DEMO [7–9].*

	ITER	**DEMO**
Fusion Power (GW)	0.5	2 – 2.5
Heat Flux (MW/m^2)	0.1 – 0.3	0.5
Neutron Flux (m^{-2}s^{-1})	10^{18}	10^{19}
Damage, displacements per atom (dpa)	3 - 10	50 – 80
Transmutation product rates at first wall	~ 30 - 100 appm He ~ 135 - 450 appm H	~ 500 - 800 appm He ~ 2250 - 3600 appm H

A cross section from ITER's vacuum vessel is shown in figure 1.1 (marked A). The first wall of the reactor, the part closest to the plasma, consists of blanket modules (BMs), marked B on the scheme. BMs will help to slow down the neutrons and to collect their released heat (their lost kinetic energy) with coolants. The BMs will contain lithium and, when the incoming neutrons are absorbed, a reaction will take, place resulting in a nucleus of tritium and a nucleus of helium. The bred tritium can then be removed from the blanket and inserted in the plasma as fuel [10]. While tungsten and beryllium are selected materials for the divertor and the first wall, respectively, high-strength copper alloy and stainless steel are used to construct the rest of BMs. In addition, ITER will also allow testing of the BMs that will be used at DEMO. In this case Eurofer97 steel is considered as a structural material for the EU Test Blanket Modules (TBMs). Eurofer97, the material discussed throughout this thesis, is the outcome of a joint effort of the European Union to develop a low activation steel to be used not in direct contact with the fusion reactions but as a second shielding [11,12]. Another important component is the divertor, marked as C in figure 1.1, which will withstand the highest thermoload of the reactor [10]. The role of the divertor is to clean the plasma by extracting heat, helium ash, and other impurities.

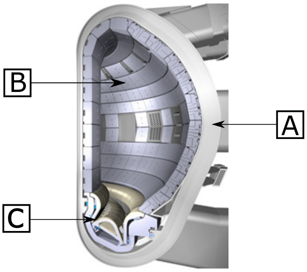

Figure 1.1 *Cross section of ITER's vacuum vessel [10]. Legend: A – vacuum vessel, B – blanket modules (BMs), C – divertor. The ITER vacuum vessel will measure 19.4 m across (outer diameter) and 11.4 m high.*

For DEMO, further developments must be achieved in plasma operation, heat exhaust, tritium self-sufficiency and neutron resistant materials [5]. An example of neutron resistant materials to be further developed is Eurofer97. Eurofer97 has an operating temperature in the range 620 – 820 K, the lower limit being due to irradiation embrittlement and the higher limit due to creep-fatigue strength [5,11]. Oxide Dispersion Strengthened (ODS) Eurofer, consisting of Eurofer97 with yttria oxide particles, was developed to increase the upper limit to 920 K [13]. Research conducted on Eurofer97 steel is of major importance not only because of its foreseen use in a fusion reactor but also because it will greatly help in the understanding of ODS Eurofer.

1.4 Thesis goals and outline

Eurofer97 has been irradiated at fission reactors to study the evolution of the microstructure and mechanical properties after being in a neutron environment. It is known that Eurofer has limited swelling from the outcoming gases of the fusion reaction and that the tensile hardening after irradiation is strongly dependent on the irradiation temperature. Although detailed mechanical tests have been performed [11,14–17], questions regarding the microstructural damage caused by neutrons, its relation to the produced gases and its relation to the evolution of the mechanical properties remain. The work in this thesis aims to answer these questions and to help define guidelines to the design and application of Eurofer97 as a structural component.

Neutron irradiation will create microstructural damage in the material. As neutrons hit the atoms in the lattice, the latter will be moved out of their original location, leaving a vacancy behind [18]. This knock-on atom has sufficient energy to remove other atoms from their position and form a cascade. The amount of damage created in the material is therefore related to the number of atoms being displaced and quantified as displacements per atom (dpa). Typical damage structures observed in irradiated material are dislocation loops and black dots, which are very small dislocation loops and defect clusters than can be seen but cannot be resolved with microscopy [19,20]. These defects have been studied with transmission electron microscopy (TEM) and the evolution of its size and density with increasing dose and temperature is observed.

The first studies presented in this thesis show helium implantations in Eurofer97 where the goal is to understand which kind of defects are associated with helium and how these evolve with temperature. Secondly, defects present in neutron irradiated Eurofer are observed and an attempt is made to relate them to alterations in the mechanical properties.

Chapter 2 provides background information on the microstructural consequences of neutron irradiation of steels, and the reflection of these in the mechanical properties. This chapter summarizes the expected microstructural defects after neutron irradiation and how these defects affect, for example, the strength of the material. Also in this chapter, the state-of-art research regarding the mechanical properties of Eurofer97 is reviewed. The focus is on the recent work on helium implantations and the evolution of irradiation defects with increasing temperature. Microscopy studies done in neutron irradiated Eurofer are also discussed and an overview of the changes observed in the mechanical properties of this material after neutron irradiation is given.

Chapter 3 treats the basic principles behind the experiments, from the chemical composition of Eurofer and the experimental procedure used for sample preparation to the experimental techniques used: positron annihilation Doppler broadening (PADB) and thermal desorption spectroscopy (TDS). In addition, an overview of the implantations and irradiation conditions is presented.

Chapter 4 presents the pre-implantation studies where knowledge regarding the as-received condition of Eurofer is collected. Before trying to understand the defects created by helium implantations and neutron irradiations, it is crucial to know the microstructure of the samples in the as-received condition: what kind of microstructural defects are expected, at which temperature do phase transitions take place and what is a typical reference measurement with the PADB and TDS techniques.

Chapter 5 shows the results obtained with the helium implanted samples. After implantation, the samples were measured with PADB and TDS, and the results obtained with the two techniques are correlated. By the end of the chapter an overview of the defect evolution with increasing temperature (up to 1500 K) is presented.

Chapter 6 shows the outcome of the neutron irradiation of Eurofer97 and the evolution of the mechanical properties. After analyzing irradiated Eurofer material with TEM, the density of defects is determined. With this value and knowing the increase of strength of the material after irradiation, a quantitative relation between defects characteristics, damage level and the yield strength is established.

Nomenclature

H	Hydrogen
He	Helium

BMs	Blanket modules
DEMO	Demonstration power plant
dpa	Displacements per atom
ODS	Oxide dispersion strengthened
PADB	Positron annihilation Doppler broadening
SET-Plan	European strategic technology plan
TBMs	Test blanket modules
TDS	Thermal desorption spectroscopy
TEM	Transmission electron microscopy

References

[1] L. Clarke, J. Edmonds, V. Krey, R. Richels, S. Rose, M. Tavoni, Energy Econ. 31 (2009) 64.

[2] J. Olivier, G. Maenhout, M. Muntean, J. Peters, Trends in Global CO2 Emissions, 2014.

[3] Comission of the European Communities, A European Strategic Energy Technology Plan (SET-Plan), 2007.

[4] Horizon 2020, http://ec.europa.eu/programmes/horizon2020/en (2015).

[5] European Fusion Development Agreement - EFDA, EFDA, Fusion Electricity: A Roadmap to the Realisation of Fusion Energy, 2012.

[6] EUROfusion, https://www.euro-Fusion.org/ (2015).

[7] R. Lässer, N. Baluc, J.L. Boutard, E. Diegele, S. Dudarev, M. Gasparotto, A. Möslang, R. Pippan, B. Riccardi, B. van der Schaaf, Fusion Eng. Des. 82 (2007) 511.

[8] P. Vladimirov, A. Möslang, J. Nucl. Mater. 329-333 (2004) 233.

[9] S.J. Zinkle, A. Möslang, Fusion Eng. Des. 88 (2013) 472.

[10] ITER, https://www.iter.org (2014).

[11] R. Lindau, A. Möslang, M. Rieth, M. Klimiankou, E. Materna-Morris, A. Alamo, A. F. Tavassoli, C. Cayron, A. M. Lancha, P. Fernandez, N. Baluc, R. Schäublin, E. Diegele, G. Filacchioni, J.W. Rensman, B.V.D. Schaaf, E. Lucon, W. Dietz, Fusion Eng. Des. 75-79 (2005) 989.

[12] N. Baluc, Phys. Scr. T138 (2009) 014004.

[13] G.R. Odette, M.J. Alinger, B.D. Wirth, Annu. Rev. Mater. Res. 38 (2008) 471.

[14] N. Luzginova, J.W. Rensman, M. Jong, P. ten Pierick, T. Bakker, H. Nolles, J. Nucl. Mater. 455 (2014) 24.

[15] E. Gaganidze, J. Aktaa, Fusion Eng. Des. 88 (2013) 118.

[16] O.J. Weiß, E. Gaganidze, J. Aktaa, J. Nucl. Mater. 426 (2012) 52.

[17] P. Spätig, G.R. Odette, G.E. Lucas, M. Victoria, J. Nucl. Mater. 307-311 (2002) 536.

[18] G. Was, Fundamentals of Radiation Materials Science, Springer Berlin Heidelberg, 2007.

[19] R. Konings, ed., Comprehensive Nuclear Materials, 1st ed., Elsevier Ltd, 2012.

[20] M. Klimenkov, E. Materna-Morris, A. Möslang, J. Nucl. Mater. 417 (2011) 124.

Chapter 2

Background

This chapter aims to overview the basics of irradiation damage and its effects on the mechanical properties of steels. Section 2.1 describes the fusion process and the relevance of studying Eurofer97 steel. Section 2.2 refers to the interaction of neutrons with the materials lattice and the damage structures created during irradiation. Section 2.3 debates on the advantages and disadvantages of ion implantations as a means to study the effects of neutron irradiation. Section 2.4 discusses the irradiation hardening and section 2.5 concerns the state of the art regarding He implantations and neutron irradiations in Eurofer97 steel.

2.1 The principle of fusion energy

Fusion reactions are the process that sustains the sun and the stars. To reproduce the fusion process on earth, nuclei of deuterium (^2H) and tritium (^3H) isotopes are brought very close together to overcome their repelling force (figure 2.1). The outcome of their fusion will be helium (^4He) nuclei, neutrons and the release of a large amount of energy. As for the availability of the fusion fuel, deuterium is a stable isotope that can be extracted from sea water [1]. Tritium, on the other hand, is radioactive and not naturally available in sufficient amounts. For the fusion reactors to be sustainable, tritium should be produced by neutrons from the fusion reaction in the breeding blankets to be installed in fusion power plants [1]. The deuterium-tritium reaction requires extremely high temperatures to take place (of the order of 150 million Kelvin). Because of that, the electrons and the nuclei of the isotopes separate and the gas becomes a plasma. As no material can withstand this high energy and the high temperature associated with it, the confinement of the reaction is done via magnetic fields [1] installed in the central section of the reactor.

In a nuclear fusion reactor the products of the fusion reaction (17.6 MeV of energy, helium and neutrons per fusion event) will be transferred to the materials confining the plasma and, to a lesser extent, to the structural materials of the reactor. It is crucial that the materials used can withstand high thermo-mechanical loads. Neutron irradiation will lead to microstructural damage and the helium gases can lead to swelling of the material matrix.

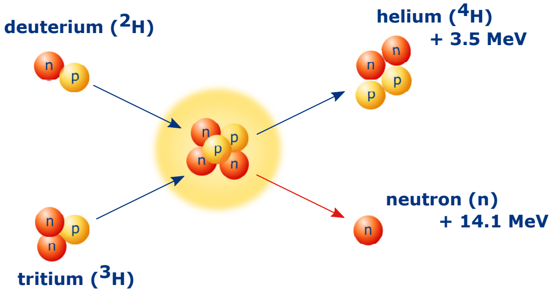

Figure 2.1 *Fusion of deuterium and tritium nuclei into a helium nucleus, a neutron and energy release.*

The construction of the first fusion reactor has already started and takes place in Cadarache, France. The project is called ITER and it is expected to produce the first plasma by 2020. A design drawing of ITER is shown in figure 2.2. The main goals of ITER are to prove that fusion energy is a viable source of energy, to test the magnetic confinement of the plasma, to verify tritium breeding concepts and to collect information to later improve the neutron shielding technology [1]. Tritium breeding will be tested with mockups of breeding blankets called Test Blanket Modules (TBMs). The blanket will help to slow down the neutrons (shielding of other components) and to collect the released heat (the neutrons' lost kinetic energy) with coolants. The TBMs will contain lithium and, in reaction with neutrons, tritium will be bred and inserted in the plasma as fuel [1].

Eurofer97 steel will be used as a structural material in the TBMs [1]. Neutron irradiation of Eurofer will lead to microstructural damage and to the transmutation of He in the matrix (discussed in section 2.2). Both situations are extremely detrimental and will affect the mechanical properties of this steel: irradiation induced swelling, increased yield strength accompanied by embrittlement, and irradiation induced stress relaxation are some examples of the alterations.

While ITER aims to prove the fusion principle as a viable source of energy, DEMO, the DEMOnstration fusion power reactor to be built on the success of ITER, aims to the step towards a commercial power plant [2].

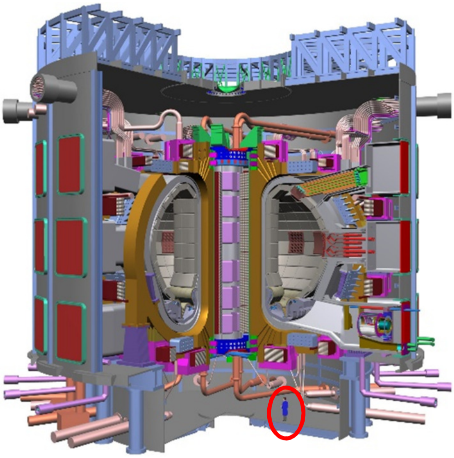

Figure 2.2 *ITER, the first fusion reactor to be built [1]. A man on the bottom right (within the red oval) is present for scale. Eurofer97 steel components will be located behind the green and dark blue panels facing the central area.*

2.2 Effects of neutron irradiation in steels

When a material is neutron irradiated, two damage mechanisms take place: displacements of lattice atoms and transmutation of helium and hydrogen.

Displacement of a lattice atom is generated by the elastic collision between a neutron and the nucleus of an atom. The first displaced atom is designated primary knock-on atom (PKA) and it dissipates its energy by colliding with other atoms in the surroundings. For PKA formation the energy of the hitting neutron must exceed a threshold energy value known as displacement energy, E^{disp}, the energy that is transferred to the recoil atom so that it is displaced and kicked off its site. If the energy transferred in the collision is lower than E^{disp}, the atom will vibrate at its equilibrium position but will not be displaced [3]. When the atom being hit is displaced it will leave a vacancy behind. If the PKA has absorbed enough energy to displace other atoms, the sequence of events is repeated and a collision cascade takes place. Eventually, all the displaced atoms thermalize either at the position of a pre-existing vacancy (a vacancy existing in the material before irradiation), at the position of a vacancy formed during the cascade displacements or as a self-interstitial atom (SIA). The number of interstitials is equal to the number of vacancies formed. The pair of an interstitial and a vacancy is called a Frenkel pair (figure 2.3). The damage created is quantified by the number of displacements per atom (dpa), the number of times an atom is, on average, displaced. Irradiation cascades can lead to severe microstructural alterations and to the alteration of the mechanical properties of the materials [3–5].

Figure 2.3 shows possible irradiation damage features. As SIAs are formed, they may aggregate and contribute to the creation of precipitates, i.e. second-phase particles in the nanometer size range, or form dislocation loops. The vacancies created in the damage cascades can also aggregate and form voids (empty clusters) or bubbles (clusters of vacancies that contain helium). Likewise, the same happens with helium – these atoms can exist as a single interstitial atom or cluster in the lattice, or on vacancies and voids.

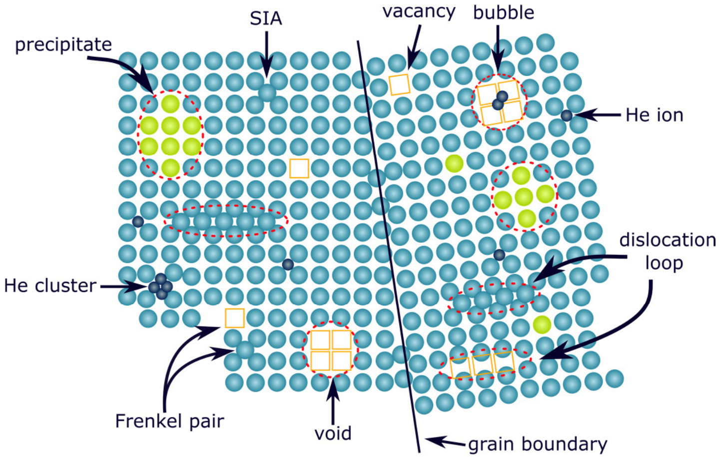

Figure 2.3 *Irradiation induced damage features.*

The transmutation of He is a point of concern as helium has a low solubility in ferrite, and tends to form clusters that can persist in the matrix over long periods of time [6]. Transmutation of He can take place due to nuclear reactions. When nickel is neutron irradiated, it can generate helium via the reactions

$$^{58}\mathrm{Ni}(n, \gamma)^{59}\mathrm{Ni} \tag{2.1}$$

$$^{59}\mathrm{Ni}(n, \alpha)^{56}\mathrm{Fe} \tag{2.2}$$

Another possible reaction is

$$^{10}B(n, \alpha)\,^{7}Li \qquad (2.3)$$

where boron produces helium and lithium.

The total amount of helium in the lattice should also include the helium produced in the breeding blanket reaction, mentioned in section 2.1. As the amount of helium present in the irradiated material increases, He atoms aggregate and form He clusters in the matrix. The accumulation of helium leads to measurable changes in the mechanical properties such as high temperature embrittlement [7]. In this case, the helium bubbles create pressure and can reduce the material's ductility and tensile strength, or even act as initiation points for cracks.

Neutron irradiation also leads to the activation of steels. Besides the transmutation of helium, reactions that yield radioactive isotopes may take place. Although the composition of Eurofer97 was carefully thought of (details described in chapter 3), the incorporation of alloying elements such as Mn, responsible for high dose rates for a period of 100 years, is still an issue for the materials reduced activation properties and its application [8].

2.3 He implantation vs. neutron irradiation

Ion implantations are widely used to simulate neutron irradiation effects. When compared to neutron irradiation, ion implantation has great practical advantages such as being straightforward to perform under well-defined implantation conditions (dose, temperature), the possibility to implant with different ions simultaneously and the absence of residual activity in the material after implantation. Neutron irradiation must be performed in a reactor and therefore these conditions differ: the irradiation temperature and the achieved dose can vary, depending on the position within the reactor core and the samples become activated, which limits the tests that can be performed afterwards.

The time span of the experiment is also an important factor: while for ion implantation the experiment time span is mainly dependent on the required dose, neutron irradiation of the material can take years to be performed as it involves capsule design, in-core irradiation of the material, cooling and disassembly of the set-up [9]. Furthermore, the expertise needed for the use of special facilities and sample handling, always keeping in mind the user's safety, can also be costly (both currency and time wise). For these reasons, ion implantations are a much cheaper option than neutron irradiations.

The main issue with ion implantations is the equivalence of the results when compared to a neutron environment. How to translate the ion implantation results to neutron irradiation data?

The first step to is to quantify the damage produced by both techniques. The damage unit for neutron irradiations is the fluence, given in n/cm^2. For ions, the damage is quantified by the integrated current in units of ion/cm^2. Both units can be converted to displacements per atom, dpa, or to dose rate as dpa/s. Another difference between neutrons and ions is the energy spectrum. While ions are produced in monoenergetic beams, the neutron energy in a reactor extends over several orders of magnitude.

The depth of penetration of ions and neutrons is another important aspect. Ion implantations have a narrow deposition profile at a well determined depth (e.g.: He ions implanted with 500 keV energy in Fe will be located at ~ 1 µm depth). The maximum depth at which ions can be implanted is of the order of hundreds of µm [9], and is determined by the implantation energy and the density of the material. Neutrons can penetrate deeper into the material and lead to a uniform damage profile.

The cross section for an ion-atom reaction is larger than for the neutron-nucleus reactions and therefore a higher damage per particle fluence will be created for ions.

While neutron irradiation is mandatory for the qualification of materials for use in fusion reactors, ion implantation provides a rapid and economical overview of radiation effects on the microstructure [9].

2.4 Irradiation hardening

The elastic and plastic behavior of materials can be studied with tensile tests, where a specimen is subject to a continuously increasing uniaxial strain. Tensile tests provide information on the yield strength (σ_y), ultimate tensile strength (σ_t), and the uniform and total elongation. Figure 2.4 shows a schematic stress-strain plot obtained from tensile tests done on neutron irradiated bcc steels, such as Eurofer97. Once a material has been plastically deformed it may not function as intended. The yield strength is related to the starting point of the plastic region and is therefore extremely important when determining the application of the material. Typically, an increase in σ_y is observed with increasing dose, mostly at irradiation temperatures below 0.3 T_m (melting temperature). The increase in σ_y due to neutron irradiation is described as irradiation hardening. A decrease in ductility (uniform and total elongation) is also noticed with increasing dose. A high elongation value is associated with ductile materials, whereas a low elongation is related to a brittle structure. The tensile strength σ_t is the maximum stress that a material can withstand before failure. After irradiation, the yield ratio $\frac{\sigma_y}{\sigma_t}$ tends to increase to values close to 1.

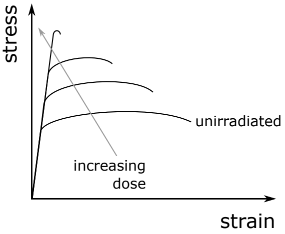

Figure 2.4 *Effect of irradiation on the stress-strain behaviour of a ferritic bcc steel. Adapted from [9].*

The yield strength is related to the behaviour of dislocations when the material is put under stress. If the applied stress is sufficient to promote dislocation movement, the material is in the plastic region and will be deformed. If that is not the case and the stress is not enough for yielding, the material is in the elastic region.

As the material is put under stress, dislocation lines present in the matrix glide and are eventually pinned at defects such as precipitates and grain boundaries. As more dislocations reach pinning points (acting as obstacles for dislocation glidding), a ‘pile up’ of dislocations occurs. The pile up causes a high stress concentration point that will eventually lead to fracture. During neutron irradiation of the material, multiple defects form in the matrix: defect clusters, dislocation loops, voids, bubbles, precipitates (see section 2.2 for irradiation induced defects). The presence of these defects represents extra obstacles for dislocations, leading to a more brittle behavior of the material. The interaction between dislocations and obstacles can be classified into athermal or thermally activated interactions. Athermal interactions are independent of temperature. In this case, dislocations bow around the obstacle. In thermally activated interactions the dislocation overcomes the obstacle by cutting through it or by means of dislocation climbing.

The presence of irradiation induced defects increases the resistance to the gliding of dislocations and is known as hardening. The irradiation hardening ($\Delta\sigma_y$) can be calculated with

$$\Delta\sigma_y = \sigma_y - \sigma_y^0 = \frac{\alpha M \mu b}{l} \tag{2.4}$$

where σ_y is the yield strength after irradiation, σ_y^0 is the yield strength before irradiation, *α* represents the obstacle strength [3,9], *M* is the Taylor factor, *μ* is the shear modulus, *b* is the Burgers vector and l is the inter-obstacle spacing after the irradiation [3,9]. According to the dispersed barrier hardening (DBH) model [3,9,10] the inter-obstacle spacing can be calculated with

$$l = {}^{1}\!/_{\sqrt{Nd}} \tag{2.5}$$

where *N* is the defect density and *d* is the obstacle diameter. To obtain this relation we should consider a volume *V* containing *n* spherical obstacles (figure 2.5).

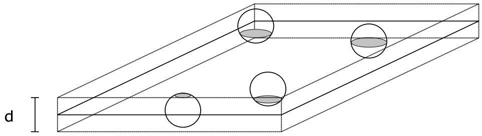

Figure 2.5 *Schematic showing the intersection of spherical obstacles of diameter d with an area A. Adapted from [9].*

All defects within this volume intersect the area *A* represented in figure 2.5. The volume *V* is therefore defined as

$$V = d \cdot A \tag{2.6}$$

with *d* being the defect diameter. The defect density *N* is given by

$$N = {}^{n}\!/_{V} \tag{2.7}$$

The area ***a*** per defect in the intersection plane is given by

$$a = {}^{A}\!/_{n} \tag{2.8}$$

Considering the case of defects being uniformly distributed in the area *A*, the distance between two sequential defects is given by l (figure 2.6).

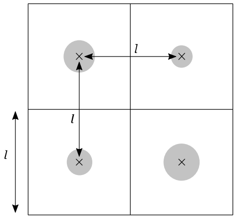

Figure 2.6 *Scheme showing an even distribution of defects on the area A. The distance between two neighboring defects is given by* l*.*

The relation between the area ***a*** the distance l is

$$a = l^2 \tag{2.9}$$

Substituting l, *n* and *V*, given by equations 2.9, 2.7 and 2.6, respectively, the relation to obtain the inter-obstacle spacing is

$$l^2 = {}^{1}\!/_{Nd} \tag{2.10}$$

which is equivalent to equation 2.5.

Alternatively, the value l can be given by the effective inter-obstacle spacing, considering that the defects opposing the dislocation movement are point defects. This equation can be obtained as follows: consider a matrix of total volume *V* and containing *n* point defects, uniformly distributed. The volume occupied per defect *v* is given by

$$v = {}^{V}\!/_{n} \tag{2.12}$$

and the concentration of defects *N* in this volume is given by

$$N = {}^{n}\!/_{V} \tag{2.13}$$

Considering two neighboring defects located at a distance *l*, the average volume *v* per defect is given by

$$v = l^3 \tag{2.14}$$

Substituting equations 2.12 and 2.13 in equation 2.14, it comes that

$$l = {}^{1}\!/_{\sqrt[3]{N}} \tag{2.15}$$

The obstacle strength, *α* (see equation 2.4), has been a point of discussion in the scientific community and little work has been done in relation to mechanical tests in Eurofer97. Although *α* is usually designated as obstacle strength, no clear definition on its significance has been agreed on – while some authors define *α* as a fitting factor, others associate it with how strong an obstacle is in stopping of dislocations. Chapter 6 of this thesis will shed light on the differences of using equations 2.5 and 2.15 to calculate the hardening of neutron irradiated Eurofer, and into the possible values of *α* for the irradiation induced defects observed in this steel.

2.5 State of the art

Eurofer97 is the pre-selected structural material for test blanket modules at ITER and later will be used for the breeding blanket of DEMO [11]. Once installed in a fusion reactor, Eurofer97 will be neutron irradiated. Neutron irradiation will severely damage the material's matrix, leading to the formation of defects and to the transmutation of helium and hydrogen. The production of transmuted He in Eurofer97 is a big concern as helium has a low solubility and tends to form clusters, which persist in the matrix over long periods of time. Helium atoms may aggregate and form clusters, leading to irradiation swelling and embrittlement [6,12,13]. The alteration of the mechanical properties after neutron irradiation is non-desirable and it should be considered for the design and application of the components. In addition to matrix damage and He transmutation, neutrons are responsible for the activation of materials. Once in the matrix, the impact of the neutrons will generate radioactive isotopes. One of the outlined goals for the materials of the structural components is that they must be recycled within a reasonable period after dismantling. Considering that, the chemical composition of Eurofer97 was carefully designed to minimize the amount of radiologically undesired elements responsible for long term activations and transmuted He [8,14,15]. A table with Eurofer97 steel chemical composition is given in chapter 3.

2.5.1 Helium implantations: reproducing the transmutation of He

Helium implantation of Eurofer97 is a widely used technique to emulate the transmutation of He (see section 2.3. for the comparison between He implantations and neutron irradiations), as after helium implantation materials can be studied with a wide range of complementary techniques.

During implantation He clusters are formed in the material. These clusters will eventually lead to the degradation of the mechanical properties. The location of the clusters is speculated to be at preferential locations such as grain boundaries and point defects. The size of the helium clusters is not well defined and depends on factors such as the implantation dose and the implantation temperature. Interstitial helium is highly mobile and has a migration energy of ~ 0.07 eV [16,17]. Considering that, an ideal implantation should be done at cryogenic temperatures (and the samples kept at the same temperature afterwards), so that the interstitial helium is trapped in the material and can later be measured. Since this is often not practical, most of the implantations are done at room temperature and it is accepted that the helium is present in the sample as He clusters (He_n) and He/vacancy clusters (He_nV_m). Furthermore, the presence of vacancy clusters (V_m, also designated as cavities) that are created during the implantation is also expected.

Sabelova [18] has studied He implanted Fe-12wt.%Cr with positron annihilation (PA) lifetime spectroscopy. It is observed that in an area containing a high He/V ratio, helium filling the implantation induced defects is observed. However, in an area with a low He/V ratio, empty vacancy clusters are noticed. This work is consistent with the observations of He implanted Eurofer97 shown in this thesis (chapter 5).

The release temperatures of helium from bubbles formed during implantation were studied by Morishita, Ono and Sugano [19–21] with the thermal desorption spectroscopy (TDS) technique at multiple implantations energies and doses. These authors have attempted to describe the mechanisms of He desorption in the temperature range of 300 – 2000 K. Morishita [19] observes the same TDS peak positions at implantation energies of 8 keV and 150 eV (figure 2.7). Peak I is ascribed to the desorption of helium from a trapping site associated with a vacancy in the neighborhood of the surface. Peak II is correlated with the desorption of helium from He_nV clusters, with $2 \leq n \leq 6$. Peak III is coincident with the phase transition of the steel and related to the dissociation of HeV pairs. This is also observed in the TDS measurements presented in this thesis (chapter 5) and related to changes in the grain boundaries during phase transition that lead to the dissociation of a high number of He_nV_m clusters. The coincidence of the phase transition with the dissociation of HeV pairs was further pursued by Xu [22,23], who assigns a high intensity peak measured with TDS around 1100 K to the phase transition of iron (1185 K), and uses a linear correlation to the other temperature values. Peak IV is linked to Ostwald ripening effects and peak V is related to the dissociation of helium from bubbles. Figure 2.8 shows the TDS spectra obtained by Ono [20] after implanting pure Fe and Fe-9Cr with 5 keV He with a dose of 2.0×10^{20} He/m^2 at a temperature of 85 K. The peaks identified as I, II and III are speculated to be related to the dissociation of helium-vacancy-self-interstitial atom complexes, to the annihilation of small dislocation loops containing helium, or to the coalescence of dislocation loops. The mechanisms behind each individual peak are not distinguished. The peaks IV and V are attributed to the migration of helium bubbles to the surface and subsequent release and to the phase transformation of the steel, respectively.

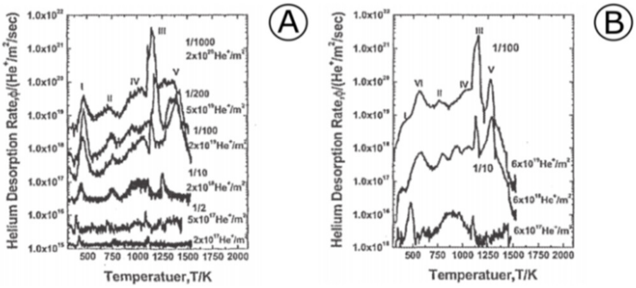

Figure 2.7 *TDS spectra of He implanted iron [19]. The implantations were conducted at room temperature. A: implantation energy of 8 keV. B: implantation energy of 150 eV. For both cases the heating rate was of 1 K/s.*

Regarding the release of He from bubbles at high temperatures with TDS spectra, Vassen [24] has suggested the presence of thermal vacancies as the cause for the continuous growth of He_nV_m clusters and the later formation of bubbles. Sugano [25] has demonstrated that with increasing temperature, the density of bubbles present in the material decreases while their average size increases. An increasing amount of desorbed helium is observed in the TDS measurements presented in this thesis (chapter 5) and associated with the He release from bubbles. This idea is confirmed by parallel positron annihilation measurements done at several annealing temperatures.

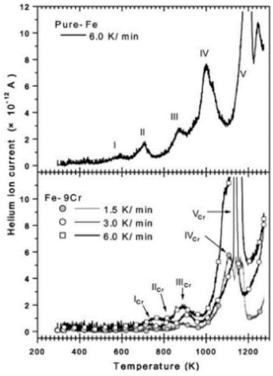

Figure 2.8 *TDS spectra of He implanted pure Fe (top) and Fe-9Cr (bottom) [20]. The implantations were performed at 473 K and a dose of 2.0 x* 10^{20} *ions/*m^2.

2.5.2 Modelling the helium behavior

The interaction of helium with vacancies has been extensively studied [17,26–31]. It has been shown that the presence of helium helps to stabilize vacancy clusters and to reduce the emission of vacancies. This is the principle of the formation of helium bubbles. The ideal ratio between He and V to obtain a stable He_nV_m cluster is a topic under discussion, with ab initio calculations suggesting the value of $\frac{n}{m}$ ~ 1.3 [27], and empirical potential calculations the value of ~ 1.8 [17,28]. An extensive list of defect-defect binding energies obtained with multiple modeling methods can be found in [26]. An example of the modeling on the formation and diffusion of bubbles in the matrix is done by Dethloff [29]. This author shows that higher irradiation temperatures and lower helium generation rates promote helium capture by sinks such as grain boundaries and line dislocations. An overview of the modeling aspects of the He diffusion and accumulation is presented in reference [26].

2.5.3 Neutron irradiation – the importance of the mechanical properties of Eurofer97

Structural steels are neutron irradiated in fission reactors as a preliminary way to study the neutron damage in fusion reactors. The irradiation of Eurofer discussed in this thesis was done at the High Flux Reactor (HFR). Vladmirov [32] has compared the neutron flux (figure 2.9A) and the ranges of helium transmutation and damage production at HFR and the predicted values for DEMO (figure 2.9B). As it is seen, the neutron flux and the damage production is lower at HFR than at DEMO. Although these are not ideal conditions, the specimens irradiated at HFR should provide insight on the interactions between neutrons and Eurofer97. The neutron flux and damage production levels for ITER are expected to be in between HFR and DEMO. This is an important aspect to keep in mind when analyzing the results of this thesis. Even so, the irradiations at HFR should be interpreted as a first step in collecting knowledge of how the neutron irradiation of Eurofer97 affects the microstructure and mechanical properties. Further investigation should be done after irradiation at ITER.

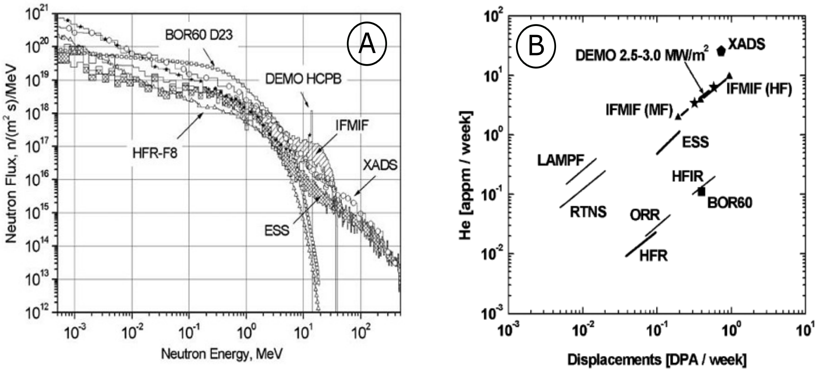

Figure 2.9 *Comparison of the neutron spectra and damage production of the blanket of the fusion reactor DEMO (DEMO HCPB (Helium cooled Pebble Bed), DEMO) and of the core position F8 of HFR (HFR-F8, HFR). A: neutron spectra; B – transmutation of helium vs. damage production. Other reactors also plotted: International Fusion Materials Irradiation Facility (IFMIF), European Spallation Source (ESS), Experimental Accelerator Driven System (XADS), Research Institute of Atomic Reactors (BOR-60), Los Alamos Meson Physics Facility (LAMPF), Rotating target Neutron Source (RTNS), Oak Ridge Research Reactor (ORR), High Flux Isotope Reactor (HFIR).*

Neutron irradiated Eurofer97 has been studied with transmission electron microscopy (TEM) by Klimenkov [33], who has observed black dots (identified as an agglomeration of point defects or fine precipitates [4]) and dislocation loops as irradiation induced defects (figure 2.10). The same type of defects are observed and discussed in chapter 5.

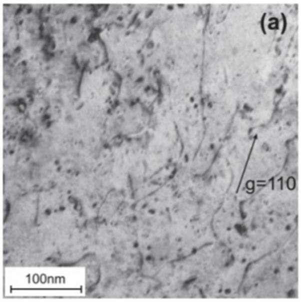

Figure 2.10 *TEM image of Eurofer97 irradiated with 16.3 dpa and 523 K [33]. Black dots and dislocation loops are observed as irradiation induced defects.*

The presence of irradiation defects is a point of concern as they affect the mechanical properties of the material. Irradiation swelling, for example, is caused by the generation and clustering of vacancies formed during the damage cascades caused by the neutrons that hit the matrix. As the irradiation temperature increases, the diffusivity of interstitial atoms is higher than the diffusivity of vacancies and interstitials can be trapped at microstructural sinks such as precipitates, grain boundaries or dislocations. As a parallel event, vacancies may aggregate and growth into voids (empty cavities) and bubbles (He filled), causing an enlargement of the material's volume. An example of the presence of bubbles in neutron irradiated Eurofer97 is shown in figure 2.11. The presence of voids and bubbles degrades the mechanical properties. Eurofer97 is a ferritic-martensitic steel and this class of steels shows swelling under 1 % up to doses of 155 dpa and irradiation temperatures above 620 K [34]. The swelling resistance is one of the reasons (perhaps the most important) why Eurofer97 is pre-selected for test blanket modules at ITER.

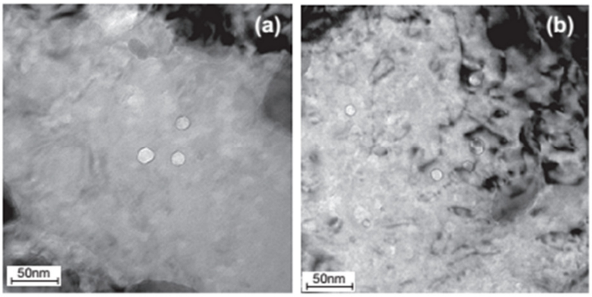

Figure 2.11 *TEM images of Eurofer97 irradiated with 16.3 dpa and 623 K [33].Bubbles containing transmuted helium are observed.*

The irradiation hardening of Eurofer after neutron irradiation is caused by the irradiation induced defects, i.e. black dots and dislocation loops. Irradiation hardening and embrittlement will greatly affect the lifetime of the components. The increase of yield strength is known to be dependent on the irradiation temperature and dose [15,35–40]. It has been observed that in tensile specimens irradiated at 333 K the hardening is ~ 1.5 times faster (as a function of damage) than in specimens irradiated at 573 K and saturates at ~ 0.4 dpa [35,36,39]. The hardening of reduced activation ferritic-martenistic steels measured for specimens irradiated at temperatures in the range 573 – 600 K and tested at the irradiation temperature shows a tendency to saturation with increasing doses up to 42 dpa [41]. If that happens, the qualification for DEMO will be achieved (expected damage in the range of 50 – 80 dpa [32,42,43]). A decrease of uniform elongation and loss of work hardening with increasing dose has been measured [35,36,44]. When specimens are irradiated at temperatures in the range 573 – 600 K and tested at 300 K, the decrease of the uniform elongation is from 6 - 8 % in unirradiated conditions to 0.5 % at a dose of 8 dpa. When specimens are irradiated and tested at the same temperature, the decrease of the uniform elongation is from 15 – 20 % to 8 % up a dose of 8 dpa.

Nomenclature

A	Area intersected by spherical defects	nm^2
a	Area occupied by each defect in the intersection plane	nm^2
b	Burgers vector	m

d	Obstacle diameter	nm
E^{diss}	Dissociation energy	eV
$^{2}\mathrm{H}$	Deuterium	
$^{3}\mathrm{H}$	Tritrium	
$^{4}\mathrm{He}$	Helium	
He_{n}	Helium clusters	
$\mathrm{He}_{n}\mathrm{V}_{m}$	Helium-vacancy clusters	
l	Inter-obstacle spacing	nm
M	Taylor factor	
N	Defect density	m^{-3}
n	Number of defects	
T_m	Melting temperature	K
V	Volume containing defects	nm^{3}
v	Average volume per defect	nm^{3}
V_{m}	Vacancy clusters	

α	Obstacle strength	
μ	Shear modulus	GPa
σ_y	Yield strength	MPa
σ_t	Ultimate tensile strength	MPa
$\Delta\sigma_y$	Irradiation hardening	MPa
σ_y^0	Yield strength before irradiation	MPa

DBH	Dispersed barrier hardening model
DEMO	Demonstration power plant
dpa	Displacements per atom
HFR	High flux reactor
PA(S)	Positron annihilation (spectroscopy)
PKA	Primary knock-on atom
SIA	Self interstitial atom
TBMs	Test blanket modules
TDS	Thermal desorption spectroscopy
TEM	Transmission electron microscopy

References

[1] ITER, https://www.iter.org (2014).

[2] L.M. Giancarli, M. Abdou, D.J. Campbell, V.A. Chuyanov, M.Y. Ahn, M. Enoeda, C. Pan, Y. Poitevin, E. Rajendra Kumar, I. Ricapito, Y. Strebkov, S. Suzuki, P.C. Wong, M. Zmitko, Fusion Eng. Des. 87 (2012) 395.

[3] J. Gittus, Irradiation Effects in Crystalline Solids, Applied Science Publishers LTD, 1978.

[4] R. Konings, ed., Comprehensive Nuclear Materials, 1st ed., Elsevier Ltd, 2012.

[5] R. Klueh, D. Harries, High-Chromium Ferritic and Martensitic Steels for Nuclear Applications, ASTM: MONO3, 2001.

[6] M.R. Gilbert, S.L. Dudarev, D. Nguyen-Manh, S. Zheng, L.W. Packer, J.C. Sublet, J. Nucl. Mater. 442 (2013) 1.

[7] H. Trinkaus, H. Ullmaier, 215 (1994) 303.

[8] R. Lindau, A. Möslang, M. Rieth, M. Klimiankou, E. Materna-Morris, A. Alamo, A. F. Tavassoli, C. Cayron, A. M. Lancha, P. Fernandez, N. Baluc, R. Schäublin, E. Diegele, G. Filacchioni, J.W. Rensman, B.V.D. Schaaf, E. Lucon, W. Dietz, Fusion Eng. Des. 75-79 (2005) 989.

[9] G. Was, Fundamentals of Radiation Materials Science, Springer Berlin Heidelberg, 2007.

[10] A.K. Seeger, in: U. Nations (Ed.), 2nd UN Conf. Peac. Uses At. Energy, Geneva, 1958, p. 250.

[11] European Fusion Development Agreement - EFDA, EFDA, Fusion Electricity: A Roadmap to the Realisation of Fusion Energy, 2012.

[12] R.E. Stoller, J. Nucl. Mater. 174 (1990) 289.

[13] M.R. Gilbert, S.L. Dudarev, S. Zheng, L.W. Packer, J.-C. Sublet, Nucl. Fusion 52 (2012) 083019.

[14] B. van der Schaaf, F. Tavassoli, C. Fazio, E. Rigal, E. Diegele, R. Lindau, Fusion Eng. Des. 69 (2003) 197.

[15] E. Lucon, P. Benoit, P. Jacquet, E. Diegele, R. Lässer, A. Alamo, R. Coppola, F. Gillemot, P. Jung, A. Lind, S. Messoloras, P. Novosad, R. Lindau, D. Preininger, M. Klimiankou, C. Petersen, M. Rieth, E. Materna-Morris, H.C. Schneider, J.W. Rensman, B. Van Der Schaaf, B.K. Singh, P. Spaetig, Fusion Eng. Des. 81 (2006) 917.

[16] K. Morishita, R. Sugano, B.D. Wirth, J. Nucl. Mater. 323 (2003) 243.

[17] K. Morishita, R. Sugano, B.D. Wirth, T. Diaz de la Rubia, Nucl. Instruments Methods Phys. Res. Sect. B Beam Interact. with Mater. Atoms 202 (2003) 76.

[18] V. Sabelová, V. Kršjak, J. Kuriplach, M. Petriska, V. Slugeň, J. Šimeg Veterníková, J. Nucl. Mater. 450 (2014) 54.

[19] K. Morishita, R. Sugano, H. Iwakiri, N. Yoshida, A. Kimura, in: Fourth Pacific Rim Int. Conf. Adv. Mater. Process., 2001.

[20] K. Ono, K. Arakawa, H. Shibasaki, H. Kurata, I. Nakamichi, N. Yoshida, J. Nucl. Mater. 329-333 (2004) 933.

[21] R. Sugano, K. Morishita, H. Iwakiri, N. Yoshida, J. Nucl. Mater. 307-311 (2002) 941.

[22] D. Xu, T. Bus, S.C. Glade, B.D. Wirth, J. Nucl. Mater. 367-370 (2007) 483.

[23] D. Xu, B.D. Wirth, J. Nucl. Mater. 386-388 (2009) 395.

[24] R. Vassen, H. Trinkaus, P. Jung, Phys. Rev. B 44 (1991) 4206.

[25] R. Sugano, K. Morishita, a Kimura, H. Iwakiri, N. Yoshida, J. Nucl. Mater. 329-333 (2004) 942.

[26] M.J. Caturla, C.J. Ortiz, C.C. Fu, Comptes Rendus Phys. 9 (2008) 401.

[27] C.-C. Fu, F. Willaime, Phys. Rev. B 72 (2005) 064117.

[28] K. Morishita, B.D. Wirth, T.D. De Rubia, A. Kimura, (2001).

[29] C. Dethloff, E. Gaganidze, V. V. Svetukhin, J. Aktaa, J. Nucl. Mater. 426 (2012) 287.

[30] C.-C. Fu, F. Willaime, J. Nucl. Mater. 367-370 (2007) 244.

[31] D. Terentyev, N. Juslin, K. Nordlund, N. Sandberg, J. Appl. Phys. 105 (2009) 103509.

[32] P. Vladimirov, A. Möslang, J. Nucl. Mater. 329-333 (2004) 233.

[33] M. Klimenkov, E. Materna-Morris, a. Möslang, J. Nucl. Mater. 417 (2011) 124.

[34] P. Dubuisson, D. Gilbon, J.L. Séran, J. Nucl. Mater. 205 (1993) 178.

[35] J.W. Rensman, NRG Irradiation Testing: Report on 300 oC and 60 oC Irradiated RAFM Steels, 2005.

[36] N. Luzginova, J.W. Rensman, M. Jong, P. ten Pierick, T. Bakker, H. Nolles, J. Nucl. Mater. 455 (2014) 24.

[37] B.V.D. Schaaf, C. Petersen, Y. De Carlan, J.W. Rensman, E. Gaganidze, X. Averty, J. Nucl. Mater. 386-388 (2009) 236.

[38] J. Rensman, E. Lucon, J. Boskeljon, J. Van Hoepen, R. Den Boef, P. Ten Pierick, J. Nucl. Mater. 329-333 (2004) 1113.

[39] J. Rensman, H.E. Hofmans, E.W. Schuring, J. Van Hoepen, J.B.M. Bakker, R. Den Boef, F.P. Van den Broek, E.D.L. Van Essen, J. Nucl. Mater. 307-311 (2002) 250.

[40] E. Gaganidze, C. Petersen, E. Materna-Morris, C. Dethloff, O.J. Weiß, J. Aktaa, a. Povstyanko, a. Fedoseev, O. Makarov, V. Prokhorov, J. Nucl. Mater. 417 (2011) 93.

[41] A. Alamo, J.L. Bertin, V.K. Shamardin, P. Wident, J. Nucl. Mater. 367-370 A (2007) 54.

[42] R. Lässer, N. Baluc, J.L. Boutard, E. Diegele, S. Dudarev, M. Gasparotto, a. Möslang, R. Pippan, B. Riccardi, B. van der Schaaf, Fusion Eng. Des. 82 (2007) 511.

[43] S.J. Zinkle, A. Möslang, Fusion Eng. Des. 88 (2013) 472.

[44] E. Lucon, W. Vandermeulen, J. Nucl. Mater. 386-388 (2009) 254.

Chapter 3

Experimental

3.1 Introduction

The goal of this research is to better understand the consequences of neutron irradiation on Eurofer97 in terms of the creation of displacement damage and the production of helium in the material. Furthermore, a correlation of these with the mechanical properties of Eurofer97 is of value when trying to foresee the materials behavior in a fusion reactor. A scheme of the experimental procedure is presented in figure 3.1. In parallel, this material has been neutron irradiated at HFR and ion implanted in multiple locations. While the neutron irradiated material was subject to mechanical tests that were followed by transmission electron microscopy (TEM) investigations, the ion implanted samples required a more detailed approach. First, the design of the samples was carefully thought of and then the conditions of tempering and annealing were selected. Finally, these samples were ion implanted and subject of positron annihilation and thermal annealing studies.

Section 3.2 mentions the material composition and the heat treatment at the manufacturer. Section 3.3 regards the sample preparation. Section 3.4 discusses He implantations and the selections of energies and doses. Section 3.5 refers to the neutron irradiations at the High Flux Reactor (HFR), in Petten. Finally, the analysis techniques are described in section 3.6.

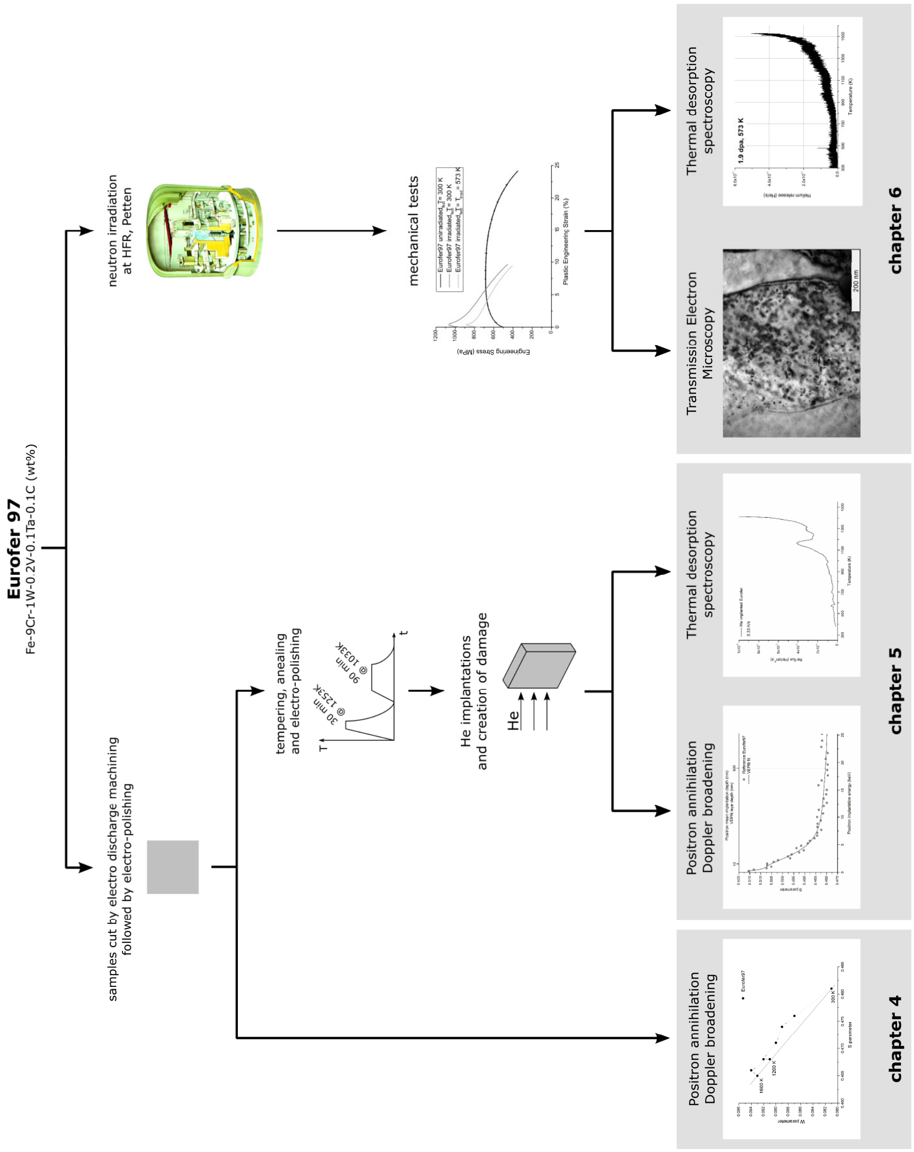

***Figure 3.1** Scheme of the experimental work.*

3.2 Material

The European Union reference batch of Eurofer97 steel was produced by Böhler (Austria), with a nominal composition of Fe-9Cr-1W-0.2V-0.1Ta-0.1C (wt.%). Table 3.1 shows a detailed description of the specifications for the chemical composition of Eurofer97.

Eurofer97 was produced by hot rolling at the manufacturer. The material has been prepared in steps. The first step consisted of an austenitization anneal of the microstructure (face centered-cubic structure, iron gamma phase) at 1253 K for 30 min. During air cooling, martensite is formed. This step is followed by tempering of the formed martensite at 1033 K for 90 min. The tempering aims to relieve mechanical stresses and to enhance toughness, and is also followed by air cooling. The final structure has tempered martensitic laths in a ferrite matrix (body centered-cubic structure, iron alpha phase) [1].

The need for a fast radioactive decay of the material after irradiation is a primary concern for environmental and security criteria when considering a future with fusion energy reactors. Figure 3.2 shows the effect of the undesired impurities in Eurofer97. This figure shows the surface gamma rate of Eurofer after irradiation as a function of time. In the legend, Eurofer ref. represents the ideal composition for Eurofer-type steel. In reality, Eurofer97 does include the radiologically undesired elements. Although these are present in small concentrations, it is clear that these trace-elements are responsible for long term activations that prevent this material of reaching a hands-on level within 100 years [3]. Improvements can be achieved by reducing the concentration in the alloy by, for example, reserve production processes for low activation steel only [4].

Eurofer97 exhibits sufficient strength for application at temperatures up to 820 K, which determines the maximum operational temperature of the fusion reactor components [5]. In order to increase the temperature limit alternative materials must be considered. It is known that oxide dispersion strengthening (ODS) is a good approach to improve the strength of ferritic-martensitic steel at temperatures above 820 K. ODS Eurofer, an Eurofer version containing yttria oxide, 0.3 wt. % Y_2O_3, was developed. ODS Eurofer was prepared by mechanical alloying at the producer Böhler (Austria).

Table 3.1 *Composition ranges of Eurofer97 [2]. Target values are given in square brackets. The total concentration of As+Sn+Sb+Zr is less than 500 ppm. Radiologically undesired elements are related to long decay times.*

	Chemical Element	**Radiologically desired**	**Specification Eurofer97 [wt %]**
Basic composition	Cr		8.5 – 9.5 [9.0]
	C		0.09 - 0.12 [0.11]
	Mn		0.20 – 0.60 [0.40]
	P		< 0.005
	S		< 0.005
	V		0.15 – 0.25
	B		< 0.001
	N		0.015 – 0.045 [0.030]
	O		< 0.01
Various Substitution elements	W		1.0 – 1.2 [1.1]
	Ta		0.06 – 0.09
	Ti	< 200 ppm	< 0.01 (100 ppm)
Radiologically undesired trace-elements	Nb	1 ppm	< 0.001 (10 ppm)
	Mo	30 ppm	< 0.005 (50 ppm)
	Ni	200 ppm	< 0.005 (50 ppm)
	Cu	100 ppm	< 0.005 (50 ppm)
	Al	30 ppm	< 0.01 (100 ppm)
	Si	1100 ppm	< 0.05 (500 ppm)
	Co	50 ppm	< 0.005 (50 ppm)
	Sn	< 20 ppm	
	As	< 50 ppm	

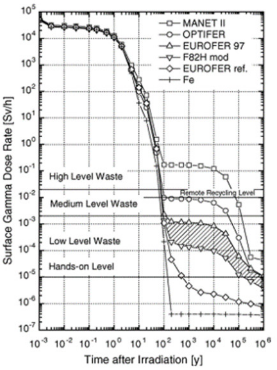

Figure 3.2 *Calculated decay of γ surface dose rate in iron and ferritic-martensitic steels after irradiation (12,5 MWa/m^2) in a first wall DEMO spectrum [5]. MANET and OPTIFER were the first reduced activation ferritic/martensitic (RAFM) steels to be developed. F82H mod is the Japanese version of a RAFM steel. EUROFER ref. represents an alloy composition containing the theoretical values of undesired elements [5].*

3.3 Sample preparation

At the start of the project a piece of Eurofer97 with dimensions 21 x 10 x 1.4 cm^3 was received. From this piece, samples were cut by wire-cut electrical discharge machining (EDM). The cutting wire of EDM has an associated dimensional error of 0.2 μm. Due to the use of a high temperature at the wire, the material properties near or at the cutting surface may be modified. In order to reduce the surface temperature effect, after EDM the samples were electro-polished with a solution of 135 ml of acetic acid and 15 ml of per-chloric acid to remove possible surface oxide layers. To ensure that the samples were still in the manufacturer conditions, including the surface region, the tempering and the annealing described at the beginning of section 3.1 were repeated, now under a low pressure of 10^{-4} Pa. In this case, both steps were followed by cooling in an argon environment at an average cooling rate of 15.6 K/min. After this, the samples were again electro-polished to remove any possible contaminations that took place in the oven.

The work presented in chapter 4 regards a study of the ‘as-received’ conditions of Eurofer97, where a piece of Eurofer is step annealed up to 1600 K. For this study, the repetition of the tempering and annealing done at the manufacturer was not considered (figure 3.1). These steps were also not included in the preparation of the plasma helium implanted samples discussed in chapter 5, section 5.2. Instead, those steps were an improvement of the experimental work used for the He implantations, shown in chapter 5.3.

3.3.1 Helium implantations

For the ion implantations samples with two different dimensions were cut by EDM: one with $14 \times 14 \times 0.5$ mm^3 and the other with $14 \times 14 \times 0.5$ mm^3. The latter were cut according to the scheme shown in figure 3.3, so after implantation nine small squares of $14 \times 14 \times 0.5$ mm^3 could be easily detached from the lager central piece with dimensions $14 \times 14 \times 0.5$ mm^3. The central piece was used for positron annihilation Doppler broadening (PADB) measurements and the smaller squares for thermal desorption spectroscopy (TDS). After being implanted, the samples were kept at room temperature.

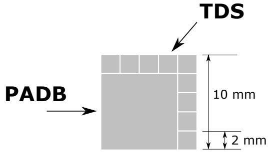

Figure 3.3 *Scheme of a Eurofer sample for He implantations.*

3.3.2 Thermal desorption spectroscopy

Both the He implanted and the neutron irradiated samples were measured with TDS. For all measurements the dimensions and volume of the TDS pieces were known. In the case of the ion implantations, samples were either cut by punch press from after plasma implantation piece (chapter 5, section 5.2) or easily detachable after ion beam implantation, as shown in figure 3.3 (chapter 5, section 5.3). For He implanted material, the dimensions of TDS samples were $2 \times 2 \times 0.5$ mm^3. The TDS measurements done with neutron irradiated Eurofer were performed using TEM discs with a diameter of 3 mm and a thickness of approximately 100 µm.

3.3.3 Transmission Electron Microscopy

Transmission electron microscopy was performed on samples subject to the conditions described in table 3.4. TEM discs were cut from tensile and impact toughness specimens that were mechanically tested at room temperature after neutron irradiation in the region furthest away from the damaged section of the fracture zone. Discs with a diameter of 3 mm and a thickness of approximately 100 μm were obtained by a sequence of grinding and polishing steps carried out in hot cells. The final thinning was done by electro-polishing. The TEM discs are estimated to have a thickness of 15 nm [6].

3.4 He implantations

Helium was introduced into Eurofer97 samples by two methods: plasma and ion beam implantation. The plasma implantations were performed in a plasma sputtering set-up as shown in figure 3.4. The conditions of the plasma implantations are shown in table 3.2. Two sets of samples (A and B) were implanted, with the latter being annealed between the last electro-polishing and He implantation in order to reduce the density of pre-existing traps in the sample. In this way, the damage observed with PADB is associated solely with the implantation itself. The low implantation energy of 3 keV was selected due to the electrical limitations of the system. The high doses were chosen to ensure that the amount of helium present in the samples was enough to be recorded by TDS. The temperatures are a direct consequence of the plasma implantation as the cooling had to be done from the back side of the samples.

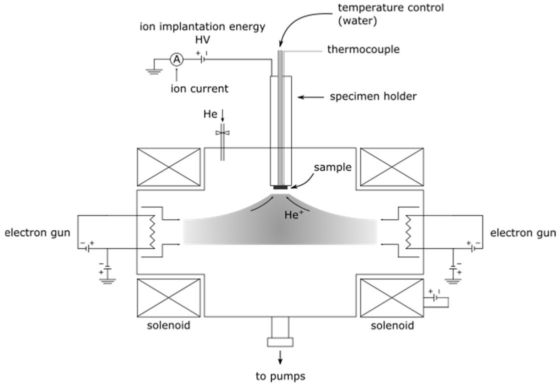

Figure 3.4 *Scheme of the plasma implantation.*

Table 3.2 *Plasma implantation conditions of Eurofer97 samples. For the set of samples* B *the pre-treatment consisted of electro-polishing followed by annealing at 1200 K for 1 hour, with oven cooling.*

Designation	Energy	Dose (He/cm^2)	Temperature (K)	Duration (s)	Current (A)
A1	3 keV	2.87 x 10^{19}	375	1800	5 x 10^{-3}
A2		1.91 x 10^{18}	450	60	10 x 10^{-3}
B1		2.87 x 10^{19}	375	3000	3 x 10^{-3}
B2		1.91 x 10^{18}	525	30	20 x 10^{-3}

The ion beam implantation conditions are shown in table 3.3. The 350 keV implantations were performed at the Helmholtz-Zentrum in Dresden, Germany. The 500 keV and 2 MeV implantations were performed at the CEMHTI-CNRS, Orléans, France. These energies were selected to widen the depth range of radiation damage in Eurofer and therefore to reduce possible surface effects. The dose range was also broadened to investigate the effect of dose in the material.

Table 3.3 *Experimental details of Eurofer97 room temperature implantations with energies of 350 keV, 500 keV and 2 MeV.*

Energy	Dose (He/cm^2)	Temperature	Duration (s)	Current (A)
350 keV	1x10^{15}	room temperature	625	2.5 x10^{-7}
	1x10^{16}		6.5 x 10^3	2.5 x10^{-7}
500 keV	1x10^{14}	room temperature	970	1.2 x10^{-7}
	1x10^{15}		4.0 x 10^3	2.8 x10^{-7}
	1x10^{16}		4.1 x 10^4	2.7 x10^{-7}
	1x10^{17}		6.9 x 10^4	16.3 x10^{-7}
2 MeV	1x10^{14}	room temperature	926	3.3 x10^{-7}
	1x10^{15}		9.4 x 10^3	1.2 x10^{-7}
	1x10^{16}		5.8 x 10^4	2.1 x10^{-7}
	1x10^{17}		1.7 x 10^5	25.6 x10^{-7}

3.5 Neutron irradiation

Eurofer97 steel has been neutron irradiated in multiple campaigns at the HFR. The HFR is a multi-purpose research and test reactor. It is a 45 MW thermal pool type reactor, with 20 in-core and 12 poolside irradiation positions [7]. A matrix of the irradiation core with thermal and fast neutron fluence rates is shown in figure 3.5A. The vertical neutron fluence rate distribution is given for location E5 (figure 3.5B) as an example. It is seen that, the damage of each specimen (given in displacements per atom (dpa)) depends on the vertical position for each reactor core location. The dose at which each specimen (singularly) is irradiated is designated as achieved dose. The average dose for each core location is designated as nominal dose. A matrix with the irradiations relevant for this work is presented in table 3.4.

The SUMO experiment stands for for *in-SodiUm steel Mixed specimens irradiatiOn*. In this experiment a set of different steel specimens for post irradiation mechanical examination (PIE) were mounted. Figure 3.6 shows the general arrangement of specimens in the SUMO irradiation capsule (rig). The specimens are placed in irradiation rigs which are filled with sodium to ensure good heat conductivity. The irradiation temperature, T_{irrad}, is calculated by the balance between the gamma heating and the heat dissipation via the gas gaps introduced in the sample holder [2]. The gas gaps are filled with a mixture of helium and neon. The temperature of the irradiation is monitored with 20 thermocouples mounted on the specimens.

Table 3.4 *NRG irradiation matrix for Eurofer97 [2].*

	Irradiation conditions					
Experiment	**Nominal Dose (dpa)**	**Achieved Dose (dpa)**	**Irradiation Temperature (K)**	**Irradiation time (full power days)**	**Irradiation position**	**Calculated helium content (appm)**
SIWAS-09	2.5	2.4	333	150	E7	13.3
SUMO-04	2.0	1.9	573	250	G7	10.5
SUMO-02	10.0	8.0	573	720	G5	12.8

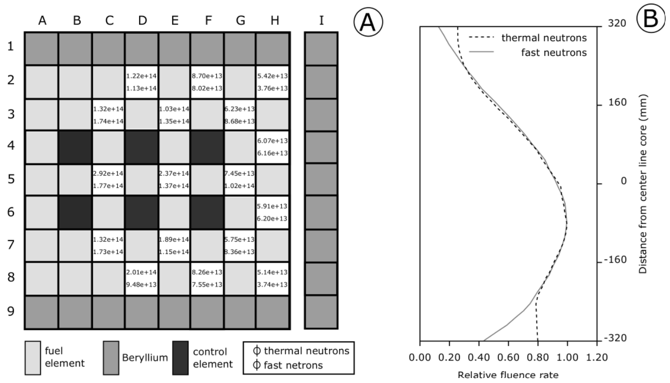

Figure 3.5 *Thermal and fast neutron fluences. Adapted from [7]. A: High flux reactor irradiation core. Thermal and fast neutron fluence rates (units in* 10^{18} $m^{-2}.s^{-1}$*) for the different in-core positions. B: Vertical fluence rate for position E5 of the reactor core.*

The other experiment is named SIWAS, which stands for *SImplified WAter-Steel irradiation*. In this experiment the specimens are inside a perforated tube and therefore in contact with the reactor cooling water [7]. As in the case of SUMO, a set of different steel specimens to perform PIE are mounted. The operating temperature control is made by moving the specimen rig vertically, changing the position regarding the neutron flux profile. Thermocouples are spread in the sample holder to monitor the actual irradiation temperature [2].

For both experiments, the neutron monitoring is typically done through 13 detectors placed in key positions within the irradiation rig. The uncertainty of the irradiation received dose in terms of dpa is 14 % [2].

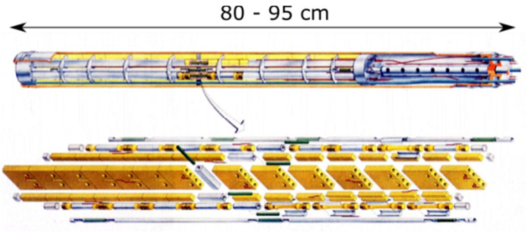

Figure 3.6 *Drawing of the general arrangement of the SUMO irradiation capsule [7]. Specimens prepared for post-irradiation mechanical testing with different shapes are included.*

3.6 Experimental techniques

3.6.1 Positron annihilation Doppler broadening

Positron annihilation Doppler broadening spectroscopy has been performed at the Reactor Institute Delft (RID), at the Variable Energy Positron beam (VEP). The goal of PADB is to study the generation and evolution of defects in materials.

3.6.1.1 PADB set-up

A scheme of the PADB set-up is shown in figure 3.7 and a detailed description of the experimental setup can be found in reference [8]. The area designated A is used for transfer of the ^{22}Na positron source to the source holder. Area B contains the source. Here, positrons are emitted from a ^{22}Na source and immediately moderated by a 8 μm thick polycrystalline tungsten foil. This moderator foil has been annealed to reduce the number of positron trapping defects. After moderation, the emitted positrons pass through a pre-accelerator, thereby raising their kinetic energy to 115 eV. The guiding of the positron beam is done through-out the set-up via 14 solenoids, with a magnetic field of 10 mT. Area C has 1 meter curvature and acts as an energy filter, removing the fast positrons from the beam. Furthermore, the curvature ensures that the source area is not in line-of-sight with the detector, which could cause false annihilation counts. The area D consists of a high electrostatic accelerator that accelerates the positrons to the user-defined energy. The acceleration is achieved by applying a high voltage to the source, the moderator, the inner tube in the curved area and the first accelerator plate of the accelerator. After passing the accelerator, the positrons are guided to the sample chamber, area E, where they hit the material being probed and annihilate in the sample. At the entrance of the sample chamber a grid is located. When a positive voltage is applied at the grid, positrons that are re-emitted from the sample are forced back and re-implanted. Areas D and E are separated by a valve that safeguards the vacuum of the system while the sample is being introduced. The pressure of the system is of the order of 10^{-5} Pa. The positron beam can be accelerated to energies in the range of 0.1 to 25 keV, creating a beam with an intensity of 10^4 positrons/s and a diameter of 3 mm.

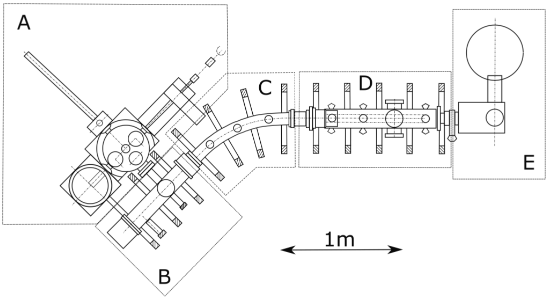

Figure 3.7 *Scheme of the PADB set-up. Adapted from [8].*

3.6.1.2 Interaction of positrons with solids

Figure 3.8 shows a scheme of the possible interactions of positrons with the solid being probed. When positrons arrive at the material's surface they can be elastically scattered and form diffracted beams. However, once in the material positrons can either diffuse back to the surface and leave the material or annihilate with an electron.

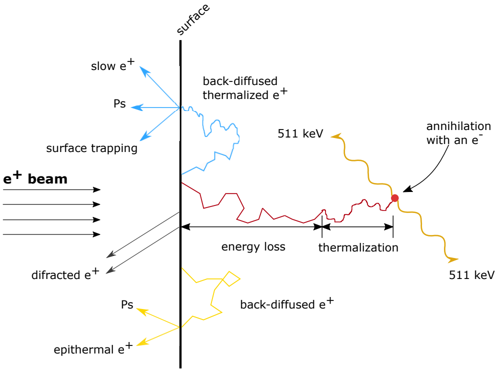

Figure 3.8 *Possible interactions of positrons with the material being probed.*

Back-diffusion can happen both prior or after thermalization of the positron. Diffusion to the surface before thermalization can lead to the emission of a high energy positron. It is also possible that, once at the surface, positronium (Ps) is formed by the aggregation of the positron with an electron [8]. The positronium eventually annihilates and, depending of the orientation of the spins of the positron and the electron, emits two gamma photons (p_Ps) of 511 keV each or three gamma photons (o_Ps) with energies in the range of 0 to 511 keV.

In the case of thermalization before back-diffusion it is possible that the positron is released at the surface [8]. In this event, the positron is re-implanted into the sample due to the positive voltage applied to the grid at the entrance of the sample chamber [8]. Other possibilities are the trapping of the positron at a defect in the solid’s surface, followed by annihilation with an electron.

3.6.1.3 Positron annihilation

After implantation, positrons may slow down to thermal energy and annihilate with electrons of the material, emitting two gamma photons of an average energy of 511 keV in almost opposite directions. This is expressed by

$$e^+ + e^- \rightarrow 2\gamma \tag{3.1}$$

where e^+ represents a positron, e^- represents an electron and γ represents a gamma

photon emitted after the annihilation. The momentum of the positron-electron pair is conserved. The γ-energy is Doppler shifted from 511 keV by an amount ΔE given by

$$\Delta E = \frac{cp_{//}}{2} \tag{3.2}$$

where c is the speed of light and $p_{//}$ is the momentum component of the electrons in the direction of the γ-emission. The photo peak is therefore broadened and the broadening can be quantified by the *S* (sharpness) parameter and the *W* (wing) parameter [8]. Figure 3.9 shows a representation of the photo peak with the two areas of interest marked. The *S* parameter reflects the ratio between the counts in the central energy window (where $|\Delta E| < 0.89$ keV) and the total counts in the photo peak. The energy choice makes the *S* parameter sensitive to positron annihilations with electrons with low momentums, as in the case of valence electrons. As the positrons diffuse in the material they might get trapped in dislocations, vacancies, voids, bubbles, increasing the probability of annihilation with low momentum electrons. For that reason, the *S* parameter reflects the degree of imperfection of the material. On the other hand, the *W* parameter relates to annihilations with high momentum electrons (2.56 keV $< |\Delta E| <$ 6.64 keV), which are basically core electrons. A high *W* parameter is associated with defect free materials.

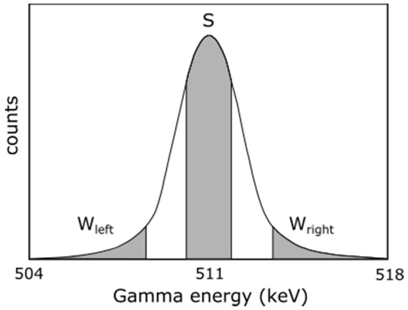

***Figure 3.9** Doppler broadening of the gamma photo peak. Representation of the S and W parameters.*

For a uniform defect distribution the *S* parameter is given by

$$S = S_d\left(\frac{C\nu}{C\nu + \lambda_b}\right) + S_b\left(\frac{\lambda_b}{C\nu + \lambda_b}\right) \tag{3.3}$$

where S_d is the *S* parameter of the defects, S_b is the *S* parameter of the bulk, *C* is the concentration of defects, ν is the specific positron trapping rate for defects (10^{14} s^{-1} [9]) and λ_b is the annihilation rate at the bulk (8.6×10^9 s^{-1} [9]). The *S* parameter is therefore a weighted average of a defect filled region (S_d) and the bulk (S_b). The *W* parameter can be interpreted in a similar manner.

The kinetics of positrons and their trapping at defects is governed by the diffusion equation

$$D_+\frac{d^2c(z)}{dz^2} - \frac{d\big(v_d(z)c(z)\big)}{dz} - (v_t n_t(z) + \lambda_b)c(z) + I(z) = 0 \tag{3.4}$$

where D_+ is the positron diffusion coefficient, ***z*** is the positron implantation depth, $c(z)$ is the steady state positron distribution, $v_d(z)$ is the positron drift velocity, v_t is the specific positron trapping rate for defects, $n_t(z)$ is the defect concentration, and $I(z)$ is the energy dependent positron implantation rate. The effective positron diffusion length, L_+, in material containing defects is given by

$$L_+ = \sqrt{\frac{D_+}{\lambda_b + k_t}} \tag{3.5}$$

where $k_t = v_t n_t$ is the positron trapping rate into defects. Further details on the origin of this equation can be found in reference [8].

Each uniform distribution region of defects is designated as a layer. Each implantation layer is modeled using a Makhovian implantation profile [10,11] described by

$$P(z,E) = \frac{2z}{z_0^2}\mathrm{e}^{\left(-\left(\frac{z}{z_0}\right)^2\right)} \quad \text{with} \quad z_0 = \frac{\langle z\rangle}{\Gamma(3/2)} \tag{3.6}$$

where *P* is the probability of a positron with an initial energy *E* being implanted a layer, z_0 an energy dependent length parameter and *Γ(3/2)* is the gamma function that will take the value of $\sqrt{\pi}/2$.

The mean positron implantation depth, $\langle z\rangle$, is calculated by

$$\langle z\rangle = \frac{A}{\rho} \times E^{1.62} \tag{3.7}$$

where *A* is a material independent constant and *ρ* is the material's density. The positron depth scales indicated throughout the thesis are calculated with a value *A* of 40 nm.(g.cm^{-3}).keV$^{-1.62}$ and a value *ρ* of 7.874 g.cm^{-3} (value of Fe density). At 25 keV, Eurofer97 has a positron implantation depth of approximately 1 µm.

3.6.1.4 Determination of *S* and *W* values

The VEPFIT program [8,12] fits the experimental data obtained during a PADB measurement. VEPFIT can fit the *S* and *W* measured data and find their best value as a function of the positrons implantation energy. In this program the user can define the number of layers (regions probed by positrons, not necessarily of the same material composition) that the probed sample has. A layer is defined as a region that contains the same type of positron traps. Figure 3.10 shows the measured *S* values for a reference Eurofer97 sample, the VEPFIT fitted curve and the user defined positron trapping layers.

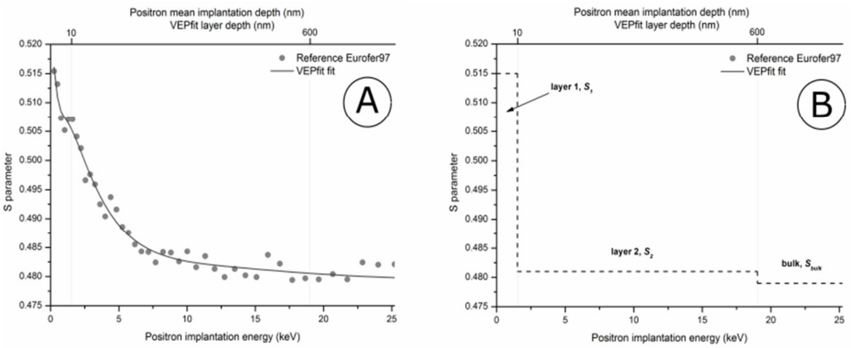

Figure 3.10 *A: measured S values of the reference Eurofer97 and the curve obtained with VEPFIT. B: defined trapping layers used in VEPFIT for the reference Eurofer97 curve. The third layer is considered as bulk. The S values obtained for each layer are marked in the S parameter scale.*

The experimental data is shown in figure 3.10A. The fit is based on the layers that are schematically shown in figure 3.10B, considering the following fitting parameter: layer 1, with 10 nm depth, layer 2, with 590 nm depth and a third layer, with an infinite depth, that is considered bulk. VEPFIT calculates the optimal *S* values of these layers taking positron diffusion into account. Similar results can be obtained for the *W* parameter. Each layer is ascribed an S_l value which, for a given implantation energy *E*, is calculated with

$$S(E) = F_s \cdot S_s + \sum_{l=1}^{N_l} \left(S_l \cdot \sum_{i=i_1}^{i_2} T_i\right) \tag{3.8}$$

where F_s is the fraction of positrons back-diffusing to the surface, S_s is the *S* value at the surface, N_l is the number of layers with the l^{th} layer covering the intervals i_1 to i_2, S_l is the *S* value for each layer and T_i is the fraction of positrons that will annihilate at layer *i*. Similarly, the equation for the *W* parameter is given by

$$W(E) = F_s \cdot SW_s + \sum_{l=1}^{N_l} \left(W_l \cdot \sum_{i=i_1}^{i_2} T_i\right) \tag{3.9}$$

By fitting the two sets of experimental data, information about the layer specific *S* and *W* values in each layer can be obtained. Throughout the thesis more details used on VEPFIT will be given, as necessary.

3.6.2 Thermal desorption spectroscopy

Thermal desorption spectroscopy is a technique based on the detection of atoms released from a sample during ramp anneal under high-vacuum conditions. The sample is placed in a vacuum chamber and the temperature is increased linearly in time. As the temperature of the material increases, the gas atoms that are present in the material can overcome their binding energy (E^b, atom-defect binding energy), migrate to the material surface and desorb into the vacuum holder.

The release rate is measured by a mass spectrometer and a thermal desorption spectrum is obtained [13]. An example of a TDS spectrum is shown in figure 3.11. The energies involved in the release of gas atoms from the lattice are schematically shown in figure 3.12. This scheme shows the energy barriers that an atom needs to overcome during implantation, desorption and migration. From the temperature at which specific desorption peaks appear, information is obtained about the defect dissociation energy and thus about the type of trap and its thermal stability. The number of gas atoms detected in a desorption peak is associated with defect concentration, number of gas atoms per defect and the dissociation energy in the case no re-trapping at another defect takes place.

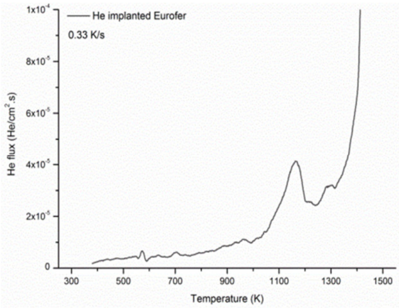

Figure 3.11 *Example of a TDS spectrum for a He implanted Eurofer97 sample. The ramp annealing rate is 0.33 K/s.*

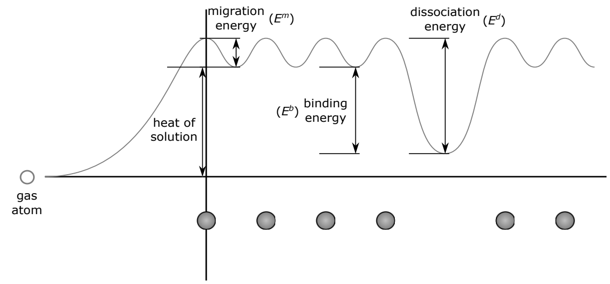

Figure 3.12 *Scheme of energies regarding a gas atom in an atomic lattice, example given for a vacancy.*

3.6.2.1 TDS set-up

The TDS system is composed of an ultra-high vacuum chamber, where the sample holder is placed, a quadruple and a calibration system. The ultra-high vacuum is achieved by a rough pump and a turbo pump in series. The quadrupole used for measuring the release of gas from the sample is a Leybold-Heraeus, Quadruvac Q100, detecting up to 10^{-8} mbar. The calibration system consists of 2 vessels of 500 cm^3, each filled with the calibration gas (in this case Helium) of a known pressure, typically on the order of 10^{-5} mbar. To calibrate the system a 1 cm^3 volume is filled with gas from one of the 500 cm^3 vessels. This volume is expanded into the vacuum chamber and detected with the quadrupole. The number of helium atoms in 1 cm^3 is calculated and compared to the known number of atoms in 500 cm^3, before each measurement. At room temperature, this 1 cm^3 volume is expected to have ~10^{12} gas atoms. The sensitivity of the system is given by the ratio between the number of gas atoms expanded and the total number of recorded pulses by the quadrupole.

3.6.2.2 Desorption rate

The desorption rate, R_d, of gas from its traps is given by [14]

$$R_d = N^x \cdot \nu_f \cdot \exp\left(-\frac{E^d}{kT}\right) \tag{3.10}$$

where *x* is the order of desorption [14], *N* is the density of traps filled with gas, ν_f is the attempt frequency, E^d is the dissociation energy and *k* is the Boltzmann constant and *T* is the temperature.

The first order desorption (x = 1) is valid when:

1. The diffusion of the gas from the sample is fast ($E^m \ll E^d$)
2. Each dissociation provides only one gas atom
3. Gas atoms do not recombine while leaving the sample

In the case gas atoms recombine or become trapped at deeper traps on their way to the sample surface, the second order desorption should be used (equation 3.10 with x = 2).

The temperature at the maximum release rate, T_p, for first order desorption is related to the dissociation energy with

$$\frac{E^d}{kT_p^2} = \frac{\nu_f}{\beta} \cdot \exp\left(-\frac{E^d}{kT}\right) \tag{3.11}$$

where *β* is the heating rate, $\mathrm{d}T/\mathrm{d}t$.

3.6.3 Mechanical testing

Mechanical tests have been done at the Nuclear Research and Consultancy Group [2,15], in Petten. The work was carried out in the lead shielded hot-cells of the NRG Hot Cell Lab (HCL).

3.6.3.1 Tensile Tests

During tensile tests the material is subjected to a stress under a constant actuator velocity, resulting in a strain rate of 5×10^{-4} s^{-1}. From the obtained stress-strain curve information is provided regarding the Yield Stress (YS) (YS offset value for 0.2 % elongation), the Ultimate Tensile Strength (UTS), the plastic Uniform Elongation (UE), the Total Elongation (TE) and the Reduction of Area (RA). The TE and the RA are measured on the specimen after testing. The geometry of the cylindrical specimens is shown in figure 3.13.

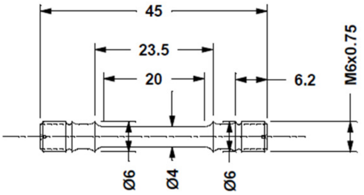

Figure 3.13 *Geometry of the cylindrical specimens used for tensile tests [2]. Dimensions in mm.*

The tensile tests were performed on Instron electro-mechanical machines in accordance with the standard ASTM E8M. The equipment has a 10 kN dynamic load cell and a furnace. The furnace temperature controllers are calibrated before each test campaign by comparing the temperature at each of the pullers and at the center of a dummy specimen. The temperature controllers have an error margin within ± 2 ºC.

Nomenclature

A	Material independent constant	nm.g.cm^{-3}.keV$^{-1.62}$
c	Speed of light	m.s^{-1}
$c(z)$	Steady state positron distribution	at. fr.
C	Concentration of defects	m^{-3}
D^+	Positron diffusion coefficient	m^2.s^{-1}
e^+	Positron	
e^-	Electron	
E	Positron implantation energy	keV
E	Energy for which VEPFIT calculates the *S* and *W* parameters	keV
E^d	Dissociation energy	eV
E^m	Migration energy	eV
F_s	Fraction of positrons back-diffusing to the surface	
He	Helium	
k	Boltzmann constant	m^2.kg.s^{-2}.K^{-1}
k_t	Positron trapping rate at defects	at. fr. s^{-1}

$I(z)$	Energy dependent positron implantation rate	at. fr. s^{-1}
L_+	Positron diffusion length	nm
$n_t(z)$	Defect concentration	at. fr.
N	Density of traps filled with gas	m^{-3}
N_l	Number of fitted layers with VEPFIT	
$p_{//}$	Momentum component of the electrons in the direction of the γ-emission	eV.m^{-1}.s
P	Probability of a positron being implanted in a layer	%
Ps	Positronium	
R_d	Desorption rate	s^{-1}
S	Sharpness parameter	
S_b	*S* parameter of the bulk	
S_d	*S* parameter of defects	
S_l	*S* parameter obtained for each layer with VEPFIT	
S_s	*S* parameter at the surface	
T	Gas release temperature	K
T_i	Fraction of positrons that will annihilate at the layer *i*	
T_p	Temperature at the maximum gas release rate	K
W	Wing parameter	
x	Order of desorption	
z_0	Positron implantation depth parameter	nm
z	Positron implantation depth	nm
$\langle z \rangle$	Mean positron implantation depth	nm
β	Heating rate	K.s^{-1}
γ	Gamma photon	keV
λ_b	Annihilation rate at the bulk	s^{-1}
$v_d(z)$	Positron drift velocity	m.s^{-1}
ν_f	Attempt frequency	s^{-1}
v_t	Specific positron trapping rate for defects	s^{-1}
ρ	Material density	g.cm^{-3}
dpa	Displacements per atom	
EDM	Electro-discharge machining	
HCL	Hot cell laboratory	

HFR	High flux reactor	
ODS	Oxide dispersion strengthened	
PADB	Positron annhilation Doppler broadening	
PIE	Post-irradiation examination	
RA	Reduction of area	%
RAFM	Reduced activation ferritic/martensitic steel	
RID	Reactor Institute Delft	
SIWAS	Simplified water-steel irradiation	
SUMO	In-sodium steel mixed specimens irradiation	
TDS	Thermal desorption spectroscopy	
TE	Total elongation	%
TEM	Transmission electron microscopy	
UE	Uniform elongation	%
UTS	Ultimate tensile strength	MPa
VEP	Variable energy positron beam	
YS	Yield strength	MPa

References

[1] G. Was, Fundamentals of Radiation Materials Science, Springer Berlin Heidelberg, 2007.

[2] J.W. Rensman, NRG Irradiation Testing: Report on 300 °C and 60 °C Irradiated RAFM Steels, 2005. doi:20023/05.68497/P.

[3] K. Ehrlich, S.W. Cierjacks, S. Kelzenberg, A. Möslang, ASTM Spec. Tech. Publ. STP 1270 (1996) 1109–1122.

[4] B. van der Schaaf, F. Tavassoli, C. Fazio, E. Rigal, E. Diegele, R. Lindau, Fusion Eng. Des. 69 (2003) 197–203.

[5] R. Lindau, A. Möslang, M. Rieth, M. Klimiankou, E. Materna-Morris, A. Alamo, et al., Fusion Eng. Des. 75-79 (2005) 989–996. doi:10.1016/j.fusengdes.2005.06.186.

[6] D. Williams, C. Carter, Transmission Electron Microscopy: A Textbook for Materials Science, Springer New York, 2009.

[7] European Comission, High Flux Reactor (HFR) Petten, Characteristics of the installation and the irradiation facilities, EUR 15151E, Comission of the European Communities, 1993.

[8] H. Schut, A variable energy positron beam facility with application in materials science, PhD thesis, Delft University of Technology, 1990.

[9] M. Eldrup, B.N. Singh, S.I. Golubov, Final Report on Investigations of the Influence of Helium Concentration and Implantation rate on Cavity Nucleation and Growth during Neutron Irradiation of Fe and EUROFER 97, 2010.

[10] A. Makhov, Sov. Phys. Solid State. 2 (1960) 1934–1951.

[11] A.P. Mills, R.J. Wilson, Phys. Rev. A. 26 (1982) 490–500.

[12] A. van Veen, H. Schut, J. de Vries, R.A. Hakvoort, M.R. IJpma, Positron Beams for Solids and Surfaces, 1991: pp. 171–198.

[13] P.A. Redhead, Vacuum. 12 (1962) 203–211.

[14] A. Fedorov, Evolution of point defect clusters during ion irradiation and thermal annealing, PhD thesis, Delft University of Technology, 2000. doi:90-407-2050-9.

[15] N. Luzginova, J.W. Rensman, M. Jong, P. ten Pierick, T. Bakker, H. Nolles, J. Nucl. Mater. 455 (2014) 24–25.

Chapter 4

Characterization of Eurofer97 in reference state by positron annihilation

Based on:

- I. Carvalho, H. Schut, A. Fedorov, N. Luzginova, J. Sietsma, J. Nucl. Mater. 442 (2013) S48-S51

Eurofer97 was step-annealed up to 1600 K, in 200 K steps. After annealing, the material was studied with positron annihilation Doppler broadening spectroscopy (PADB). The evolution of the *S,W* parameters is interpreted in relation to the phase transitions of this steel. At 300 K Eurofer97 has a tempered martensitic structure. In the range 1200 K - 1400 K the material is the austenitic region. During annealing in this temperature range the carbides present in the matrix dissolve and grain growth is expected. During cooling, a fresh (non-tempered) martensitic microstructure is formed. After annealing at 1600 K the material will present a ferritic-martensitic microstructure. By comparing the *S,W* values of Eurofer to those of pure Fe (measured at 300 K and after annealing at 1200 K for 1 h, oven cooling), it is concluded that the concentration of defects present in Eurofer97 tends to become similar to that of pure Fe with increasing annealing temperature.

4.1 Introduction

In order to understand the implantation- and irradiation-induced defects, it is important to have a clear picture of the reference material, both in terms of reference values and microscopic evolution. In this chapter a study of the reference Eurofer97 steel is presented. A reference sample of Eurofer97 was step-annealed up to 1600 K, in 200 K steps. Section 4.1 refers to a study in which Eurofer97 was annealed at temperatures up to 1600 K to better understand the defects behavior with increasing temperature. Section 4.2 resumes the findings of this annealing study, serving as a starting point for the interpretation of behavior of helium implanted samples in chapter 5.4.2.

4.2 Annealing study

With the goal of understanding the effect of increasing temperature on the material, Eurofer97 was annealed up to 1600 K, in 200 K steps. The annealings were performed in sequence, always using the same Eurofer sample. The sample was annealed under a low pressure of 10^{-4} Pa and kept at the annealing temperature for 1 h before furnace cooling at a rate of ~ 8 K/min. For this study, Eurofer97 was not annealed and tempered after being cut with electric discharge machining (see chapter 3, section 3.2., for sample preparation details).

A section of the quasi-binary iron-chromium phase diagram obtained for a constant value of 0.1 wt%C [1] is shown in figure 4.1. A vertical line corresponding to 9% Cr is traced. This composition, Fe-9%Cr, is equal to that of Eurofer97 steel. For 9% Cr steel the first phase transition of the material takes place between 1133 K and 1163 K, where the microstructure changes from ferrite (*α*, bcc) to austenite (*γ*, fcc). The second phase transition of the material takes place at 1570 K, where both austenite and ferrite phases coexist.

Figure 4.2 shows the continuous cooling transformation (CCT) diagram of Eurofer97 [2] starting at 1253 K, where the microstructure is fully austenitic before cooling. In this diagram lines representing different cooling rates are plotted. It is observed that when the material is annealed above 1163 K and cooled at rates above 7 K/min [2], such as in the case of this work and the air cooling performed at the manufacturer, a fully martensitic transformation will take place starting at 658 K.

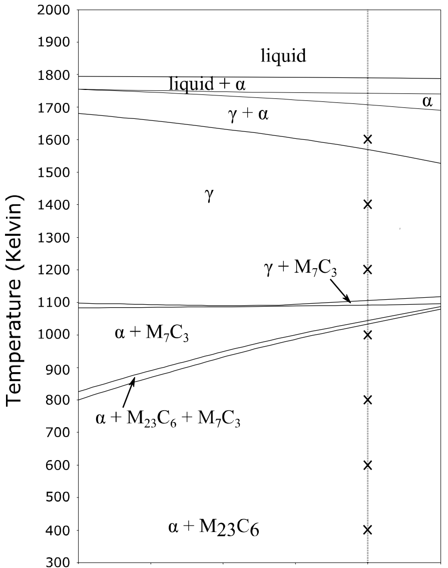

Figure 4.1 *Quasi-binary iron-chromium phase diagram with a constant value of 0.1 wt%C. Phase diagram obtained with Thermo-Calc software [1]. The phase transitions of a 9Cr-0.1C-Fe wt% steel are similar to those of Eurofer97. The annealing temperatures are marked with a cross in the line corresponding to 9% Cr steel.*

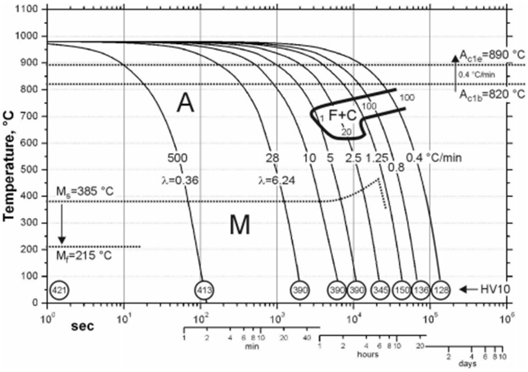

Figure 4.2 *Continuous cooling transformation diagram of Eurofer97 [2]. At annealing temperatures above 1163 K and cooling rates higher than 7 K/min martensitic microstructure will be formed. Legend: A - austenite, M - martensite, F - ferrite, C - cementite.*

After each annealing step the sample was studied with PADB. The measurements were performed at room temperature. Figure 4.3 shows the *S* and *W* parameters values as a function of the positron implantation energy and the positron implantation depth. The data points of the measurements at 300 K and after annealing 1600 K are plotted. The fitting quality noticed for these temperatures is representative for the fits for all annealing temperatures. For the fitting, a VEP model with one uniform layer was used (see section 3.5.1. for more information on the VEPFIT program). The fitted *S* and *W* values at positron implantation energies above 10 keV are shown in table 4.1 and designated as S_b and W_b. The S_b and W_b parameters have an associated error of 2 x 10^{-4}. For positron implantation depths larger than typically 250 nm the *S* parameter shows no variation with depth. For these depths, a decrease of the *S* value with increasing temperature is evident and ascribed to a decrease in the fraction of annihilations at vacancy type defects. A similar reasoning can be established for the *W* parameter.

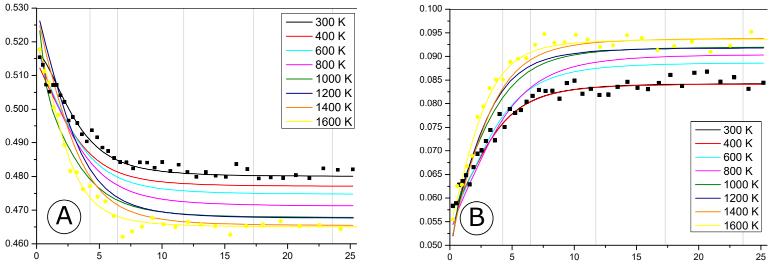

Figure 4.3 *PADB measurements of the annealing study of Eurofer97. VEPFIT curves are plotted as solid lines. Data are presented for 300 K and 1600 K curves.*

Table 4.1 *Fitted S and W parameters of the annealing study with Eurofer97 steel.*

Annealing temperature (K)	S_b parameter (± 0.0002)	W_b parameter (± 0.0002)
300	0.4812	0.0845
400	0.4770	0.0868
600	0.4747	0.0887
800	0.4712	0.0905
1000	0.4678	0.0920
1200	0.4676	0.0918
1400	0.4654	0.0938
1600	0.4650	0.0936

Figure 4.4 shows a graph of the S_b-W_b parameters determined for the different annealing temperatures of the Eurofer97 measurements. In this plot the S_b,W_b points that correspond to a tempered martensitic microstructure (after cooling, bcc) are connected with a dashed black line (300 K - 1000 K). The S_b,W_b points that correspond to a fresh martensitic microstructure (newly formed, after cooling, bct) are connected with a full grey line (1200 K - 1400 K). The S_b,W_b point obtained after the annealing at 1600 K reflects the presence of two phases after cooling: ferrite and martensite (bcc and bct, respectively).

At 300 K Eurofer97 is in the as-received condition and has a tempered martensitic microstructure that contains carbides [3,4] and defects such as vacancies. As the annealing temperature increases up to 1000 K, carbides are expected to coarsen and the density of vacancies present in the tempered martensitic microstructure is reduced, accompanied by a decrease of the S_b value and, inversely, an increase of the W_b value.

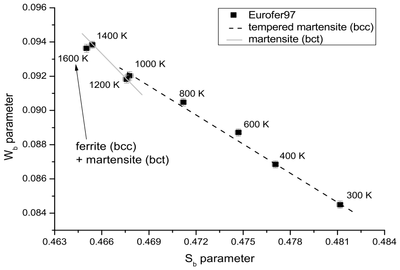

Figure 4.4 *S_b vs. W_b plot for annealed Eurofer97. The annealings were performed in sequence and had the duration of 1 h. The dashed black line reflects the trend of the S,W parameters associated with a tempered martensitic microstructure. The full grey line reflects the trend of the S,W parameters associated with a (not tempered) martensitic microstructure.*

As the material reaches 1200 K, it enters the austenitic region (*γ* phase, fcc) and the carbides present in the matrix dissolve (see the phase diagram in figure 4.1). During cooling, the cooling rate of the oven of 8 K/min, promotes the formation of a martensitic microstructure (bct, see CCT diagram in figure 4.2), which is noticed by only a slight decrease of the S_b value and a decrease of the W_b parameter with respect to the annealing done at 1000 K. The formation of the fresh martensitic microstructure is accompanied by multiple phenomena: the dissolution of carbides [5] and formation of dislocations in the material's lattice distortion due to the martensitic microstructure (bct). While the first phenomenon should reflect a decrease of the *S* value and an increase of the *W* value, the formation of dislocations will balance this effect and increase the *S* parameter and decrease *W*. A continuous grain growth of austenite [6] is noticed up to the annealing temperature of 1400 K.

During the annealing at 1600 K the material enters the ferritic and austenitic phase of the diagram. Upon cooling, the austenitic microstructure will not survive and the material will have a ferritic and a fresh martensitic microstructure (fcc and bct crystal structures, respectively). In relation to the S_b,W_b point of the annealing at 1400 K, the S_b and W_b values corresponding to 1600 K show a decrease of the S_b and W_b values. This is explained by a balance between the defects formed in the martensitic microstructure and the ferritic microstructure, containing lower defect concentrations and no carbides.

4.2.1 Comparison with pure iron

Figure 4.5 shows a graph of the fitted S_b-W_b values of Eurofer97. Added to this figure are the *S,W* values of a pure iron (Fe) sample, measured at 300 K and after annealing at 1200 K for 1 hour. Both *S,W* points associated with pure Fe reflect a ferritic microstructure. The measurement reflecting the annealing at 1200 K of the Fe sample was done after cooling, with the sample at room temperature. The *S* and *W* values were obtained with the same fitting procedure that was used for Eurofer. In figure 4.5 the traced lines connect the characteristic type of defects of pure Fe (dashed grey line) and the same two lines as in figure 4.4 (dashed black line for temperatures in the range 300 K - 1000 K, full grey line for temperatures of 1200 K and 1400 K).

For pure Fe, a decrease of the *S* and increase of the *W* values is noticed after annealing at 1200 K. The differences in the *S,W* values are associated with the annealing of dislocations present in the as-received condition (300 K), and to grain growth [6].

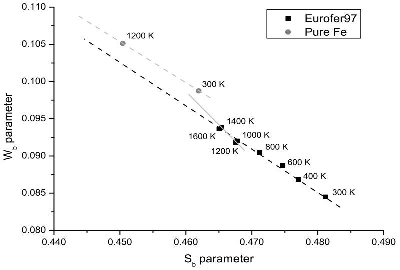

Figure 4.5 *S_b vs. W_b plot for annealed Eurofer97 and pure Fe. The annealings were performed in sequence and had the duration of 1 h. The dashed black line traced for Eurofer97 reflects the trend of the S,W parameters associated with a tempered martensitic microstructure. The full grey line traced for Eurofer97 reflects the trend of the S,W parameters associated with a (not tempered) martensitic microstructure. The dashed grey line traced for pure Fe reflects the trend of the S,W parameters associated with a ferritic microstructure.*

Looking at the *S,W* pairs of the Eurofer97 sample, the direction of the fitted lines connecting the annealings in the range 300 K - 1000 K and the annealings at 1200 K and 1400 K point in the direction of the line traced for the two *S,W* values associated with pure Fe. As Eurofer is annealed in the range 300 – 1000 K, the carbides in the matrix coarsen leading to a lower concentration of positron trapping sites, and the environment sensed by positrons in Eurofer becomes similar to that of Fe (which has no carbides, low concentration of positron trapping sites). The trend observed for the *S,W* points referring to the annealings of Eurofer in the range 1200 K – 1400 K reflect a matrix without carbides, such as the one from pure Fe. The common orientation of the fitted lines leads to the idea that, if annealed at higher temperatures, the concentration of defects in Eurofer97 would become increasingly similar to those of pure Fe.

4.3 Conclusions

At 300 K Eurofer97 has a tempered martensitic structure and contains dislocations and carbides [5]. Together with grain boundaries, these defects act as positron annihilation sinks. As the annealing temperature increases to 1000 K, the density of positron trapping sites present in the material is reduced and a decrease of the *S* parameter and increase of the *W* value is observed. When the sample is annealed at 1200 K it enters the γ phase region. While cooling, a fresh (non-tempered) martensitic microstructure will be formed. The PADB measurements at room temperature after annealing at 1200 K and 1400 K reflect the grain growth of austenite affecting the martensitic structure, the dissolution of carbides and formation of dislocations in the material. As the temperature increases to 1600 K, Eurofer97 will present a ferritic-martensitic microstructure after cooling.

A comparison of the *S-W* values of Eurofer97 to those of pure Fe (the latter measured at 300 K and after annealing at 1200 K for 1 h), shows a trend of the concentration of defects present in Eurofer97 to become similar to that of pure Fe.

Nomenclature

S_b	*S* parameter obtained for positron implantation energies above 10 keV
W_b	*W* parameter obtained for positron implantation energies above 10 keV

PADB	Positron annihilation Doppler broadening
CCT	Continuous cooling transformation diagram

References

[1] J.O. Andersson, T. Helander, L. Hoglund, P.F. Shi, B. Sundman, Calphad 26 (2002) 273.

[2] M. Rieth, The Chemical Composition of the EUROFER Steel, 2007.

[3] Z. Lu, R.G. Faulkner, N. Riddle, F.D. Martino, K. Yang, J. Nucl. Mater. 386-388 (2009) 445.

[4] P. Fernández, A. M. Lancha, J. Lapeña, M. Serrano, M. Hernández-Mayoral, J. Nucl. Mater. 307-311 (2002) 495.

[5] V.B. Oliveira, M.J.R. Sandim, D. Stamopoulos, R. A. Renzetti, A. D. Santos, H.R.Z. Sandim, J. Nucl. Mater. 435 (2013) 189.

[6] W. Callister, D. Rethwisch, Materials Science and Engineering: An Introduction, 7th ed., John Wiley & Sons, 2007.

Chapter 5

He implantations: the first step to understand defect creation in Eurofer97

Based on:

- I. Carvalho, H. Schut, A. Fedorov, N. Luzginova, J. Sietsma, J. Nucl. Mater. 442 (2013) S48-S51
- I. Carvalho, H. Schut, A. Fedorov, N. Luzginova, P. Desgardin, J. Sietsma, J. Phys.: Conf. Ser. 443 (2013) 012034
- I. Carvalho, H. Schut, A. Fedorov, N. Luzginova, P. Desgardin, J. Sietsma, J. Nucl. Mater. 442:1-3 (2013) 377-381
- I. Carvalho, H. Schut, A. Fedorov, N. Luzginova, P. Desgardin, J. Sietsma, J. Phys.: Conf. Ser. 505 (2014) 012019

With the aim to characterize the type of defect structures formed during implantation and to investigate their thermal stability, helium (He) implanted samples were studied using positron annihilation Doppler broadening (PADB) and thermal desorption spectroscopy (TDS). The results obtained with the two techniques are correlated. Eurofer97 was plasma and ion beam implanted. The plasma implantations were carried out with 3 keV energy and with doses in the range 10^{18-19} He/cm^2. Two sets of samples were implanted: set A, in the as-received condition, and set B, after annealing at 1200 K for 1 h. Within each set, one sample was implanted at a low temperature (375 K) and the other at a high temperature (450 K or 525K). After implantation, set A shows a decrease of the *S* value and increase of the *W* value when compared to those obtained pre-implantation. Set B yields *S* and *W* parameters with similar values, before and after the helium implantation. Furthermore, for the samples implanted at a higher temperature the diffusion towards the bulk of the He ions is deduced. The ion-beam implantations were done at room temperature with energies of 350 keV, 500 keV and 2 MeV, and doses in the range 10^{14-17} He/cm^2. The correlation of the results obtained with PADB and TDS allows the understanding of the evolution of implantation induced defects with increasing temperature. Below 1200 K the helium-vacancy (He_nV_m) clusters dissociate. The temperature of the helium release is dependent on the dissociation energy of the helium-per-vacancy (He/V) ratio of the cluster. Above 1200 K, the formation of bubbles (large He_nV_m clusters) takes place.

5.1 Introduction

Typical neutron irradiation experiments in research reactors require years of in-core exposure to reach an appreciable fluence, and typically another year of disassembly and cooling in order to safely handle the irradiated samples. These factors, together with the need of specialized knowledge and handling facilities, make neutron irradiations costly. To optimize the irradiation settings, pre-irradiation ion implantation studies are often done. Ion implantations are an economic and flexible way to emulate the damage created by neutrons. The material to be analyzed can be implanted with ions of various energies, ion fluxes and at selected temperatures. However, it is important to keep in mind that ion implantation conditions and induced defects do not correlate directly with those of neutron irradiations. When the implantations are done with He ions, the main differences between to neutron irradiations are the location of the damage created, the local density of the damage, and the temperature at which the defects are created.

In the case of helium implantations, the created damage is located at a sub-surface region whose depth depends on the implantation energy. For neutron irradiation, the damage is distributed over the thickness of the material. That said, it is important to keep in mind that the He implantations presented in this chapter were done considering that the damaged region is representative of the full volume of an irradiated sample and that the primary knock-on atom (PKA) energy distribution is also similar to that of neutron irradiations. The temperature at which implantations and irradiations are done has a great impact on the evolution of the created defects. Under typical reactor operating conditions neutron irradiations take place at elevated temperatures. Focusing on the application of Eurofer97 in a Tokamak-type fusion reactor, operational temperatures in the range of 620 to 820 K are expected. The He ion implantations presented in this chapter were performed at room temperature. Implantation at this relatively low temperature allows the study of the interaction between the helium and the native defects, i.e. defects existing in the material before implantation. An important parameter of the ion implantations is the depth-dependent He-to-defect ratio, which can be controlled by choosing the implantation dose and energy by comparing results obtained with samples with different native defect densities. Following the implantation, subsequent annealing experiments give insight into the evolution of the initial irradiated situation with temperature. Knowledge regarding the helium formed during neutron transmutation reactions and its evolution is therefore contained in this type of experiments.

Section 5.2 refers to plasma implantations at low (3 keV) energies. The effect of the implantation temperature is presented in this section. Section 5.3 refers to ion beam implantations. In this section a correlation between PADB and TDS measurements is established and the evolution of helium-vacancy clusters in the temperature range of 300 K - 1500 K is discussed.

5.2 Plasma implantations

The first step to understand the implantation induced defects and clustering of He ions in Eurofer97 was to perform plasma implantations. The implantations were done in two sets of samples that differ in the density of defect structures prior to implantation. The different defect densities are intended to better distinguish between the defects introduced during manufacturing and the defects due to ion implantation. After implantation, the samples were measured with PADB and TDS and the results of the two techniques were correlated.

5.2.1 Implantation conditions

To differentiate between defects created by the implantation and those pre-existing in the sample due to the cold-rolling manufacturing process, one set of samples was annealed prior to the plasma implantation. Samples in set A were not pre-treated and therefore are expected to contain pre-existing defects (defects prior to the implantations). Samples in set B were vacuum annealed at 1200 K for 1 h before implantation and furnace cooled at a rate of ~ 8 K/min. At the start of the implantations, the material in set A is expected to have a tempered martensitic microstructure (information provided by the manufacturer). The material in set B is expected to have a fresh (not tempered) martensitic microstructure (see chapter 4 for a study of an annealed reference sample). From each set, one sample was implanted at a low temperature of 375 K to a dose of the order 10^{19} He/cm^2 (samples A1 and B1). Samples A2 and B2 were implanted to a dose of the order 10^{18} He/cm^2 and at temperatures of 450 K and 525 K respectively. Table 5.1 presents the implantation conditions of sets A and B. A scheme of the sample preparation and measurements related to the plasma implantation is shown in figure 5.1. Further details of the implantation and the sample preparation can be found in chapter 3.

Table 5.1 *Plasma implantation conditions of samples in set A and set B.*

Sample code	**Implantation temperature (K)**	**Implantation dose (He/cm^2)**
A1	375	3×10^{19}
A2	450	2×10^{18}
B1	375	3×10^{19}
B2	525	2×10^{18}

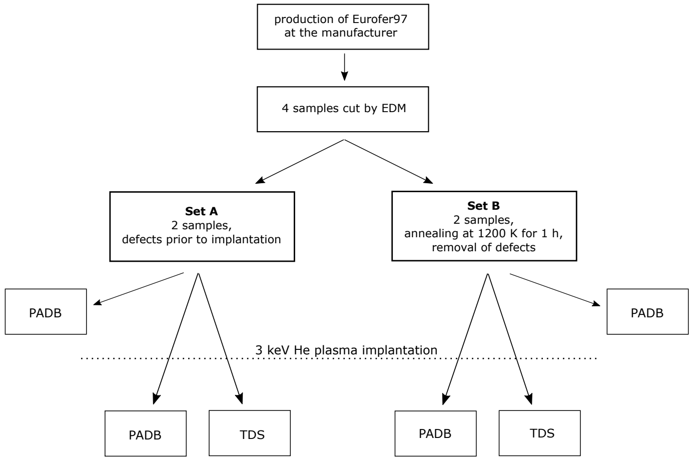

Figure 5.1 *Scheme of the sample preparation and measurements regarding the 3 keV plasma implantations. The samples were cut from the original manufacturer piece by electro-discharge machining (EDM).*

As the maximum attainable potential difference between sample and the electrodes was 3 keV, the implantation energy was limited to this value. TRIM [1] simulations of the defect and He distributions for an Fe-9%Cr alloy and a dose of 10^{18} He/cm^2 are shown in figure 5.2. The defect distribution is related to the formation of Frenkel pairs (information about the effects of ion implantations and neutron irradiation in steels can be found in chapter 2). It is noticed that both the He and defect distributions, with their maxima at approximately 15 nm and 8 nm, respectively, are well within the positron probing range of about 1 μm in Eurofer97.

The method used to plasma He implant the Eurofer97 samples has some controversial points. In chapter 3, section 3.4 a scheme of the implanter is shown. The samples implanted had a size of 14 x 14 x 0.5 mm^3. The samples were attached to the sample holder by one of the corners, with a small screw. Due to the design of the experiment, doubts can be raised regarding the uniform distribution of helium ions in the sample. Since the sample was mounted above the plasma at a distance of approximately 4 cm and the plasma hit the sample mostly in its center, it is possible that the central area of the sample had a higher implantation dose, as shown in figure 5.3. This would influence the TDS measurements of samples A1 and B1, in which a corner piece was cut from the implanted sample.

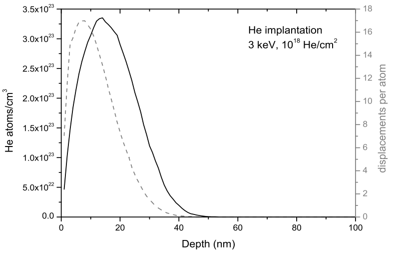

Figure 5.2 *TRIM simulation of He implantation and damage creation depth range for 3 keV, 10^{18} He ions/cm^2 in Fe-9Cr. TRIM simulations assume a 0 K environment. The solid black line corresponds to the implanted He concentration (He atoms/cm^3) and the dashed grey line corresponds to the displacements per atom.*

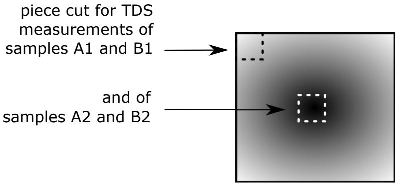

Figure 5.3 *Scheme representing the plasma implanted region of the Eurofer97 sample. A corner piece was used for the TDS measurements of the samples A1 and B1.*

5.2.2 Positron annihilation measurements

Before implantation, a sample from each set was measured with PADB. Figure 5.4 shows the reference *S* and *W* curves of sets A and B (samples after being cut by electro-discharge machining, as seen in figure 5.1); the reference of set B reflects the annealing at 1200 K for 1 h. Since the curves show a gradual decrease from the surface towards the interior of the sample, the data was fitted with VEPFIT considering a single layer. For both sets, the fitted plateau values of *S* and *W* parameters for positron implantation energies above 10 keV are defined as S_{b1} and W_{b1}. The values of S_{b1} and W_{b1} are characteristic of the bulk of Eurofer97 steel and are presented in table 5.2. The *S* and *W* values in the surface region will not be discussed, since they strongly depend on the surface conditions. It is possible that during thermalization positrons back-diffuse towards the surface and annihilate there.

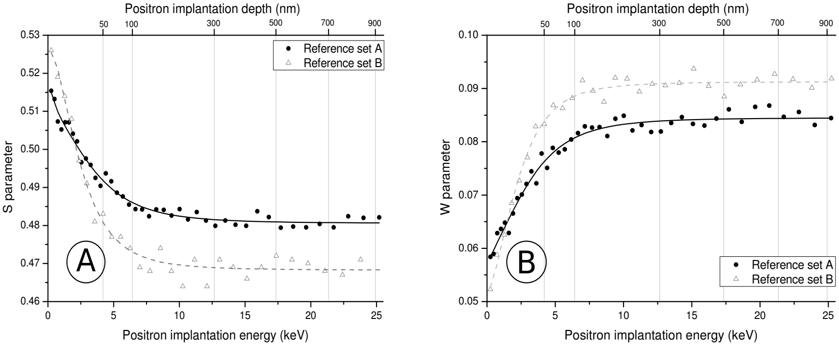

Figure 5.4 *S (A) and W (B) curves of the reference non-implanted samples of sets A and B. Reference B has been annealed at 1200 K for 1 h. The lines show the fits obtained with VEPFIT.*

Table 5.2 *S and W values fitted with VEPFIT of the reference and the 3 keV He implanted samples. Set B was annealed at 1200 K for 1 h before implantation. The indexes 1 and 2 in the S and W parameters referrer to the L_1 and L_2 fitting layers, respectively.*

Designation	***S* parameter (± 0.0005)**		***W* parameter (± 0.0005)**	
	S_{b1}		W_{b1}	
Reference set A	0.4812		0.0845	
Reference set B	0.4682		0.0913	
Implanted samples	**S_1, layer L_1, depths < 30 nm**	**S_2, layer L_2, depths > 30 nm**	**W_1, layer L_1, depths < 30 nm**	**W_2, layer L_2, depths > 30 nm**
A1	0.5338	0.4638	0.0541	0.0934
A2	0.5209	0.4621	0.0457	0.0955
B1	0.5366	0.4634	0.0943	0.0947
B2	0.5212	0.4700	0.0479	0.0923

As the surface might have a different chemical composition than the bulk of the sample (e.g. oxide formation), the annihilations at shallow positron implantation depths should not be considered for the analysis of the material. The formation of positronium is also possible. More details on surface effects can be found in chapter 3, section 3.6. As a consequence of disregarding the measurement data for positron energies below 10 keV, no significant outcome of the positron diffusion length was achieved with VEPFIT. Without the information obtained at depths below ~ 200 nm, the profile of the *S* and *W* curves is entirely flat and the positron diffusion length related to the high energy positron implantations cannot be obtained with VEPFIT (the positron diffusion length is obtained by comparing different sections of the positron implantation profile).

As mentioned in chapter 3, the *S* parameter is given by

$$S = S_d\left(\frac{C\nu}{C\nu + \lambda_b}\right) + S_b\left(\frac{\lambda_b}{C\nu + \lambda_b}\right) \tag{5.1}$$

where S_d is the *S* parameter of a region containing defects, S_b is the *S* parameter of the bulk, *C* is the concentration of defects, ν is the specific positron trapping rate for defects (10^{14} s^{-1} [2]) and λ_b is the annihilation rate at the bulk (8.6×10^9 s^{-1} [2]). The *S* parameter is therefore a weighted average of the *S* values of a defect filled region (S_d) and the bulk (S_b) (for the purpose of this thesis, considered a defect free region). Looking at figure 5.4A and considering both *S* curves, it is possible to assume that S_b can take a value of 0.4600 and S_d of 0.4900 (S_b should have a lower *S* value than the reference of set B as even after annealing at 1200 K for 1 h some defect structures will remain in the sample; S_d should have a *S* value higher than the reference of set A as during the annealing at the manufacturer some of the defects present in the microstructure are removed). The defect concentration can be derived from equation 5.1, as

$$C = \frac{\lambda_b}{\nu}\left(\frac{S - S_b}{S_d - S}\right) \tag{5.2}$$

Substituting the estimated S_d and S_b parameters in equation 5.2 and considering that the S_{b1} value of the reference of set A is 0.4812 (full black line), the defect concentration takes the value of 2 x 10^{-4} m^{-3}. In the case of the reference of set B (dashed grey line), the S_{b1} value is 0.4682 and the defect concentration is 3 x 10^{-5} m^{-3}. The comparison of both defect concentration values clearly shows that a significant part of the pre-existing defects of set B have been annealed after 1 h at 1200 K. Although the calculation of the relative defect concentrations depends on the choice of the S_d and S_b parameters, their exact value does not affect the interpretation of the outcome as long as S_d is higher than the S value of the set A and S_b is lower than the S value of the set B.

After implantation, sets A and B were measured with PADB. The results are shown in figure 5.5. The obtained results were fitted with VEPFIT. The fits were done using two layers that represent the ratio between the He content and damage created by the plasma implantations, which is described in terms of vacancies (V). The first layer, designated L_1, is defined for depths less than 30 nm (~ 3 keV). The second layer, designated L_2, describes depths larger than 30 nm. The thicknesses of these layers are based on the TRIM simulations (figure 5.2), where two regions can be defined based on their He/V ratio. While L_1 represents a region with a high He/V ratio (this region contains the maximum of the implanted He ions), L_2 represents a region with low He/V ratio. The S and W fitted values for each layer are designated S_1,W_1 and S_2,W_2 and their values are shown in table 5.2.

The S curves of samples A1 and A2 (figure 5.5A) show fitted S_2 plateau values well below the value S_{b1} found for the reference sample and are comparable to the measured S values of high-temperature annealed samples (1600 K) presented in chapter 4. Since the temperature of the samples during the implantation is low (375 K, 450 K) and even though the duration of the implantations can reach 30 min, the decrease in S_2 cannot be solely explained by thermal annealing. Another possible reason for the decrease of the S_2 value is that during implantation He migration occurs, which is followed by He trapping at the pre-existing defects, such as vacancies and dislocations, abundant in the samples of set A. Helium-vacancy defects have less open volume in comparison to an empty vacancy. This implies a lower S parameter and a higher W parameter (figures 5.5A and B). For set B (figures 5.5C and D) the bulk values of the implanted samples are similar to that of the corresponding reference sample in accordance with the lower concentration of pre-existing defects.

In the damaged region (depths less than ~ 30 nm), all implanted samples show an increase of the S_1 value in comparison to the reference value, which is representative for the creation of vacancy-type defects during the 3 keV implantation (figures 5.5A and C). For the B2 sample (and to some extent also for the A2 sample) the increase of the S value in the first 30 nm is less pronounced than that of samples B1 and A1, possibly due to recombination effects caused by the higher implantation temperature, in combination with the lower fluence.

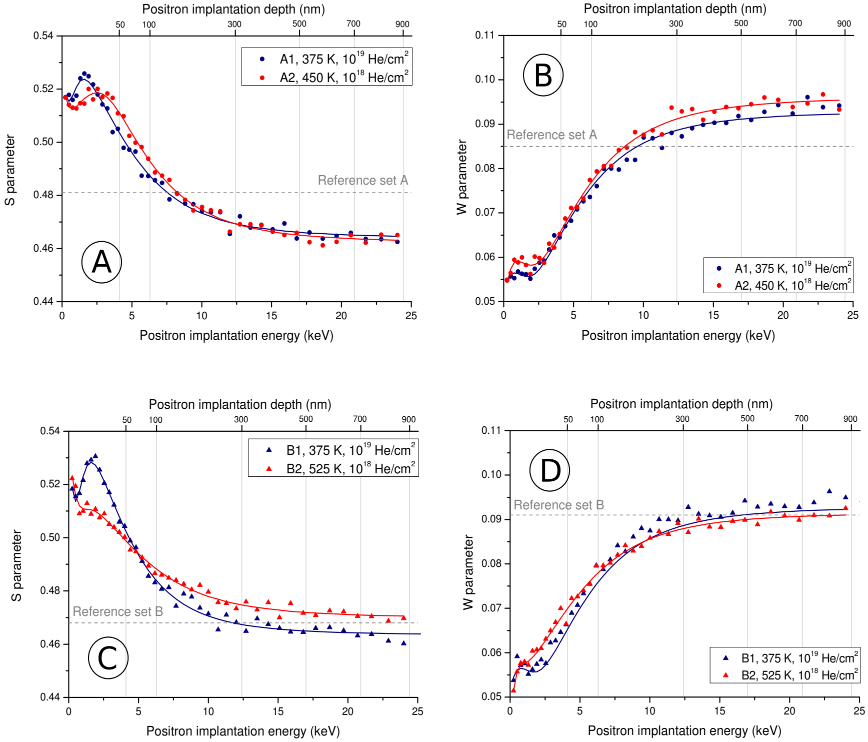

***Figure 5.5** S (A and C) and W (B and D) curves of the He implanted samples. Set B has been annealed at 1200 K for 1 h before ion implantation. A dotted line representing the S_{b1} and W_{b1} parameters of the references of each set are plotted for comparison. VEPFIT curves are plotted as solid lines.*

5.2.3 Thermal desorption spectroscopy analysis

Parallel to the PADB studies, the thermal stability of the implantation induced defects was studied with TDS. Figure 5.6 shows the TDS spectra of both sets of 3 keV He implanted samples. The TDS measurements of samples A1 and B1 were performed using the middle TDS sample piece, whereas for samples A2 and B2 an off-centre piece was chosen (see figure 5.3).

The horizontal axis at the top of the graphs represents the dissociation energy corresponding to the annealing temperature, located at the bottom axis and obtained for a fixed heating rate. The dissociation energy (E^d) is the energy necessary for He desorption from defect structures. This concept is schematically shown in chapter 3, figure 3.12 .The dissociation energy is related to the temperature according to

$$\ln\left(\frac{\beta}{T^2}\right) = -\frac{E^d}{k_B T} + \ln\left(\frac{\nu_f k_B}{E^d}\right) \tag{5.3}$$

where *β* is the heating rate, k_B is the Boltzmann constant, *T* is the peak temperature and ν_f is the jump or attempt frequency, assumed to be 10^{13} s^{-1} [3]. As mentioned in reference [3], equation 5.3 assumes that there are no mutual transformations between traps with different E^d values (that the type of traps does not change, e.g. that two clusters of two vacancies each do not aggregate and form a four-vacancy cluster). This, of course, is not the real situation since when the temperature increases an evolution between different types of traps is expected to take place, as well as re-trapping of He after release from a trap. Even so, this equation provides an estimation of the dissociation temperature of a defect cluster with a given dissociation energy.

In the TDS setup used the samples were linearly heated to 1500 K at a rate of 0.33 K/s. Before each measurement the system was baked out overnight at 470 K to reduce the background signal (i.e. humidity in the system that could lead to He counts in the quadrupole). The sharpest peak observed in TDS spectra is believed to relate to the phase transition of martensite into austenite and is therefore corrected to the temperature of 1163 K (peak marked IV in figure 5.6; a phase diagram of Eurofer97 is presented in chapter 4, figure 4.1). Knowing that the high He release peak should appear at 1163 K, the temperature position of the other peaks is adjusted linearly. Due to the lack of a background spectrum, no background subtraction is performed to the measurement spectra. This means that during the measurements the quadrupole sensed peak from helium will partially overlap with the peak from hydrogen (related to the humidity present in the system). The background signal is also present in the spectra shown in figure 5.6. It was noticed that the peak at 1163 K was clipped by the quadrupole for the set A samples. This peak has been reconstructed and its height increased by approximately 10 %.

As mentioned at the end of section 5.2.1., questions can be raised regarding the uniform implantation of ions with the plasma system used and the location from where the TDS pieces were cut. However, the fact that a high intensity peak (peak

IV, corrected for the 1163 K temperature) was observed for all measurements is an indicator of a successful implantation. The dissociation energy of this peak, 3.45 eV, is associated with the desorption of He from clusters with a He/V ratio of ~ 1.8 [4], likely He_2V [5]. The differences between the spectra can be associated with the differences in the sample preparation of the two sets (set B was annealed at 1200 K for 1 h prior to implantation) and the implantation conditions.

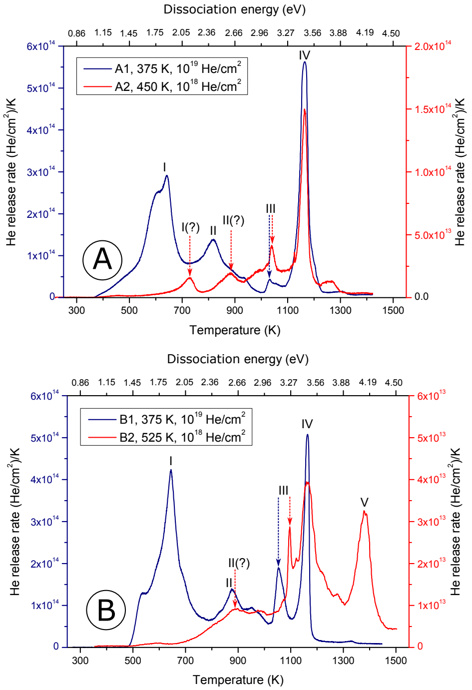

Figure 5.6 *TDS spectra of the 3 keV He implanted samples. A: set A. B: set B, annealed at 1200 K for 1 h before implantation. For samples A2 and B2 the central piece of the implanted sample was used for measurement. The background has not been subtracted.*

For all spectra (figure 5.6) four He release peaks can be distinguished and are marked as I, II, III and IV. For the B2 sample (red line in figure 5.6B), one extra peak is observed at 1400 K and is identified as peak V. From these spectra it is clear that for samples A1, A2 and B1 the majority of helium is released below 1163 K. For sample B2 most of the helium is released above this temperature.

5.2.4 Discussion

The desorption of He from the implanted samples is achieved when the He_nV_m clusters reach their dissociation energy due to an increase of the material's temperature. Clusters may delay the release of He by the aggregating free vacancies present in the matrix. The existence of vacancies in the matrix is explained by the dissociation of vacancy clusters (V_m) formed during the implantation. The binding energy of such clusters is slightly higher than 1 eV and takes place up to 700 K [4].

The differences in the sample preparation are noticed both with TDS and PADB measurements. Before implantation, the 1200 K annealing for 1 h of the samples in set B is sensed by the lower S parameter (and higher W parameter), in comparison to the samples in set A (reference measurements are shown in figure 5.4). After implantation (figure 5.5) two regions of interest arise from the PADB measurements: a region below 30 nm depth, with a high He/V content, and another beyond 30 nm depth, with a lower He/V content. The damaged region, denominated L_1, is similar for all implanted samples. The ion implantation has a stronger impact in the L_2 region of set A than that of set B. For set A the S parameter decreases (and the W parameter increases) pronouncedly beyond the implantation range. This can be understood due to the higher defect concentration of set A before implantation. When implanted, the He ions diffuse through the sample and are trapped at the pre-existing defects, such as vacancies and dislocations, abundant in the set A samples. The Helium-vacancy defects have smaller open volume for positron to annihilate at and yield a lower S parameter and a higher W parameter, in comparison to an empty vacancy. For set B, the lower density of pre-irradiation defects (He traps) together with the high implantation temperature of the B2 sample probably promote the diffusion of He into the bulk of the sample and away from the region probed by positrons.

In the TDS spectra (figure 5.6), not only the effect of the sample preparation is noticed but also the implantation conditions are reflected in the measurements. As stated, for samples A1, A2 and B1 the majority of helium is released below 1163 K (peak IV), while for sample and B2 most of the helium is released above this temperature. The relevance of the identified peaks is always interpreted in comparison to peak IV.

Peak I and II are observed for all spectra. Peak I is likely associated with desorption of He from He_nV_m clusters with a dissociation energy of ~ 2 eV and a He/V ratio of ~ 0.5 [4]. As the helium is released from the clusters, it can either reach the materials surface and be detected by the quadrupole, or be retrapped by He_nV_m clusters with a higher dissociation energy. In parallel, the dissociation of vacancy clusters that are formed during the implantation is expected to take place up to 800 K [4]. As the V_m clusters dissociate it is possible that the vacancies in the matrix aggregate with He_nV_m clusters, increasing the dissociation energy of that cluster. The presence of peak II is explained by the release of He_nV_m clusters with a dissociation energy of ~ 2 eV and a He/V ratio of ~ 0.5 [4]. Peaks I and II are distinguishable in samples A1, A2 and B1 and, for sample B2, an increase of He desorption is observed only at the temperatures corresponding to peak II. These peaks have stronger relative intensity (in comparison to peak IV) for the samples A1 and B1. That intensity can be explained by the higher (10^{19} He/cm^2) implantation dose of these samples, which increases the He/V ratio in the defect clusters. As for the samples A2 and B2, the implantation temperature is a key factor. It is likely that, during the implantation, part of the formed He_nV_m clusters are being annealed (desorption of He from the clusters is promoted during the implantation itself). This effect is enhanced for the B2 sample, where the implantation temperature is the highest (525 K).

The differences in the sample preparation are also observed in the location of peak III, which is located between 1000 K and 1100 K. Peak III is of higher relative intensity for samples set B than for set A (in relation to the other peaks present on each spectrum). The dissociation energies associated with this temperature range are 2.96 eV to 3.27 eV, characteristic of the dissociation of He_2V [5]. At the moment it is unclear why the density of such defect clusters is higher in set B than in set A.

The effect of the implantation temperature and, to some extent, of the sample preparation, is noticed on peak V, located at ~ 1400 K and only observed for the sample B2. At this point, it is interesting to recall that the B2 sample had the highest implantation temperature: 525 K. Other authors [6–9] mention that above ~ 1200 K the formation of bubbles with low He content takes place. It is likely that the formation of bubbles delays the release of the remaining He of the sample to higher temperature in the B2 sample. The higher implantation temperature of this sample plays an important role as it promotes the diffusion of He towards the interior of the sample, increasing the trapping rate of He ions. The annealing at 1200 K for 1 h of the set B sample, prior to the implantation, also reduces the helium traps in the sample and promotes inward diffusion.

The percentage of helium retention after implantation, calculated as the area below the TDS spectra (including system background), is presented in table 5.3, from which two observations can be made:

- For all samples the fraction of retained helium is very low. This might be a consequence of the low 3 keV implantation energy and consequently shallow implantation region of less than 30 nm as predicted by TRIM. This enables a large fraction of He-ions to back-diffuse to the surface, thereby decreasing significantly the amount of He trapped.

- The samples A2 and B2, implanted at the higher temperatures, retain the highest fraction of helium. This can be partly due to the choice of the central TDS piece to be analyzed and by the diffusion of helium into the material being promoted by the implantation temperature.

Table 5.3 *Helium retention for 3 keV plasma implanted samples. Set B was annealed at 1200 K for 1 h before He implantation. For samples A2 and B2 the central piece of the implanted sample was used for measurement. The retention is calculated as the area under the TDS spectra, which includes the background of the system.*

Sample code	Implantation temperature (K)	Implantation dose (He/cm^2)	He desorbed (He/cm^2)	He retention (%)
A1	375	3 x 10^{19}	8.5 x 10^{16}	0.28
A2	450	2 x 10^{18}	3.5 x 10^{16}	1.75
B1	375	3 x 10^{19}	9.3 x 10^{16}	0.31
B2	525	2 x 10^{18}	1.6 x 10^{16}	0.79

5.3 Ion-beam implantations

This section aims to understand the consequences of different He implantation energies and doses in Eurofer97 steel. The thermal stability of the implantation defects is also studied by annealing the samples in the PADB beam and with the help of TDS measurements. The annealing of the samples was done in steps, up to 1500 K.

5.3.1 Implantation conditions

Eurofer97 was ion-beam He implanted with energies of 350 keV, 500 keV and 2 MeV. The samples were implanted at room temperature and with doses in the range of 10^{14}-10^{17} He/cm^2. The sample preparation for the ion beam implantations differs from the one of the plasma implanted samples: the annealing and tempering steps done by the manufacturer were repeated after cutting the samples by EDM, as schematically shown in figure 5.7. The samples are expected to have a tempered martensitic microstructure at the moment of the ion implantation. The decision of repeating the annealing and tempering steps at the manufacturer rose based on the idea that the method used to cut the samples, EDM, might induce defects in the near surface region, which would affect the outcome of the implantations and the PADB measurements. Further details of the sample preparation and of the implantation conditions can be found in chapter 3.

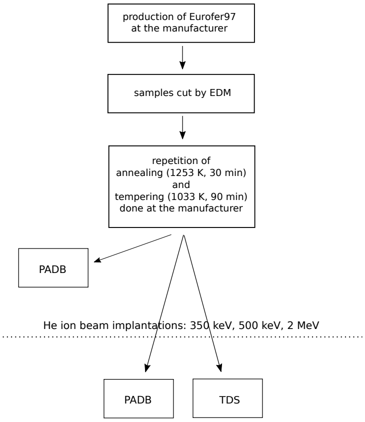

Figure 5.7 *Scheme of the sample preparation and measurements regarding the 350 keV, 500 keV and 2 MeV ion-beam implantations. The annealing and tempering of the samples, initially done at the manufacturer, was repeated in order to minimize possible surface effects originated by electro-discharge machining.*

TRIM [1] simulations were performed in order to know at which depth the ions are located in the sample. The defects and He distributions, given for a Fe-9%Cr alloy and a dose of 10^{15} He/cm^2, are presented in figure 5.8. The peaks of the ion ranges for 350 keV, 500 keV and 2 MeV are located at depths of 780 nm, 1.0 µm and

3.2 µm, respectively. The maximum values for the displacements per atom are at slightly different depths, with values of 720 nm, 955 nm and 3.15 µm. For all implantation energies, the density of implanted ions and of damage events rapidly drop to zero beyond their maximum value.

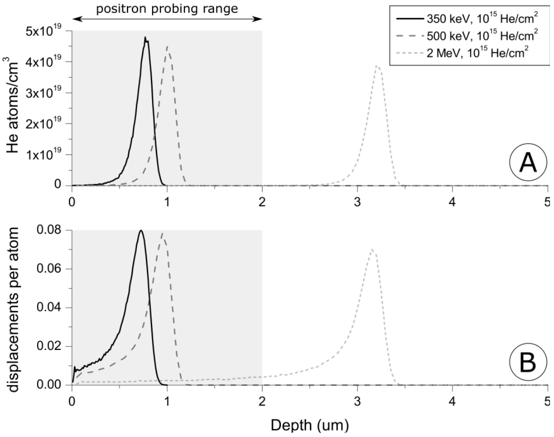

***Figure 5.8** TRIM simulation of He implantation and damage creation depth range for 350 keV, 500 keV and 2 MeV, for a dose of 10^{15} He ions/cm^2 in Fe-9%Cr. TRIM simulations assume a 0 K environment. A - implanted He concentration (He atoms/cm^3). B - displacements per atom.*

5.3.2 Positron annihilation measurements

The PADB measurements of the ion-beam implanted samples were performed with the samples in an *in-situ* oven mounted in the positron beam (figure 5.9). By measuring a non-implanted sample in the regular holder (used for the plasma implanted samples) and the oven-holder (used for the ion-beam implanted samples), it was noticed that the position of the *S* and *W* points were vertically shifted for *S* and *W*, respectively.

The reference curve of a sample representative for the condition of the material before implantation was measured only with the regular holder. Figure 5.9 shows the *S* and *W* curves of the reference sample. As in the case of reference sample for the plasma implantations, the data was fitted considering a single layer in VEPFIT. The fitted *S* and *W* values at positron implantation energies above 10 keV are designated S_{b2} and W_{b2} and take the values of 0.4532 and 0.1123, respectively.

The *S* and *W* values in the surface region will not be discussed as they strongly depend on the surface conditions.

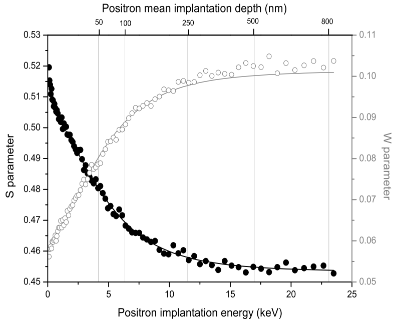

Figure 5.9 *PADB measurements of a reference sample, before ion implantation, in the regular sample holder. The data is presented as symbols and the VEPFIT fits are presented as solid lines.*

As it will be discussed later, it was noticed that annealing the 2 MeV, 10^{14} He/cm^2 sample at 800 K yielded the lowest *S* and highest *W* values measured (table 5.4). This *S,W* point, added on PADB plots of this section as a blue asterisk, will serve as a reference point representing a well annealed and defect free sample. More details about this *S,W* point will follow in the discussion of the annealing study of the 2 MeV samples (section 5.3.2.1.1.).

The fits of the data obtained for samples implanted at 350 keV and 500 keV were done with a total of three layers: two layers associated with the damage created by the ion-beam implantations plus a deeper layer for the bulk. The thicknesses of the first two layers are based on the TRIM simulations (figure 5.8), where two regions can be defined based on their He/V ratio. The first fitted layer, L_1, has a thickness of 250 nm and 300 nm for 350 keV and 500 keV energies, respectively, and represents the region with a low He/V ratio. The second fitted layer, L_2, has a thickness of 750 nm and 700 nm, respectively for 350 keV and 500 keV, and represents the region of the damage peak where a high He/V ratio is expected. In the case of the 2 MeV implantations, one single layer (L_1) was used in the fit since the He and V concentrations are low over the entire positron probing range (figure 5.8). The L_1 layer used in the fits of the 2 MeV samples is equivalent to the L_1 layers of the 350 keV and 500 keV samples as all L_1 layers have a similar He/V ratio. The third layer (L_b) of the implantations at 350 keV and 500 keV is considered to be bulk and is equivalent to the non-implanted reference sample. In this study it was noticed that, in order to obtain a good fit, the thickness of L_2 had to be decreased as the annealing temperature of the samples was increased. Nonetheless, the sum of the thicknesses of L_1 and L_2 was kept constant. The fitted *S* and *W* values obtained for the L_1 and L_2 layers are shown in table 5.4.

Table 5.4 *S and W values fitted with VEPFIT of the reference and the ion-beam implanted samples. The reference mentioned in this table refers to the 2 MeV, 10^{14}He/cm^2 sample after annealing at 800 K. This point is represented by a blue asterisk on the PADB plots of section 5.3.2.*

Designation		**S parameter (± 0.0005)**		***W* parameter (± 0.0005)**	
Reference		0.4483		0.01014	
Implanted samples		***S₁*, layer *L₁***	***S₂*, layer *L₂***	***W₁*, layer *L₁***	***W₂*, layer *L₂***
2 MeV	10^{14} He/cm^2	0.4675	—	0.0887	—
	10^{15} He/cm^2	0.4893	—	0.0769	—
	10^{16} He/cm^2	0.5110	—	0.0681	—
	10^{17} He/cm^2	0.5317	—	0.0604	—
350 keV	10^{14} He/cm^2	0.4840	0.4888	0.0805	0.0775
	10^{15} He/cm^2	0.4917	0.4933	0.0779	0.0753
	10^{16} He/cm^2	0.5183	0.5022	0.0653	0.0653
	10^{17} He/cm^2	0.5343	0.5106	0.0608	0.0686
500 keV	10^{14} He/cm^2	0.4777	0.4845	0.0853	0.0784
	10^{15} He/cm^2	0.5052	0.5081	0.0696	0.0682
	10^{16} He/cm^2	0.5260	0.5169	0.0614	0.0651
	10^{17} He/cm^2	0.5196	0.4961	0.0624	0.0707

Let us start by looking at the *S,W* plot of the 2 MeV implanted samples (figure 5.10). The points refer to *S* and *W* values of the L_1 layer of the measurements done at room temperature. The region probed by positrons in these samples is far away from the location of the peak of He ions (~ 3 μm depth). This region is expected to contain mostly empty and small vacancy clusters, formed during implantation, and a low density of He ions. As the implantation dose increases, the concentration of the clusters will increase. Clusters of vacancies containing He ions, He_nV_m, might also be present, but considering the distance between the region probed by positrons (~ 1 μm depth) and the maxima of the He ions, the density of such clusters will be low. The *S,W* trend observed for the 2 MeV samples implanted at the various doses can be modeled using an equation reflecting the presence of different types of defects created during the implantation. The equation for the positron annihilations being accounted for in the *S* parameter is given by

$$S = (1 - f_t) \cdot S_{ref} + f_t \cdot S_d \tag{5.4}$$

where f_t is the fraction of annihilations in defects, S_{ref} is the reference *S* parameter and S_d is the *S* parameter of the defects (see eq. 5.1.). For these implantations, considering a simple model with only two types of defects, the *S* parameter can be described by

$$S_d = f_{d1} \cdot S_{d1} + f_{d2} \cdot S_{d2} \quad \text{with} \quad f_{d1} + f_{d2} = 1 \tag{5.5}$$

where f_{d1} and S_{d1} denote the fraction of annihilations in and the *S* parameter of small V_m clusters, respectively, and f_{d2} and S_{d2} denote the fraction of annihilations in and the *S* parameter of large V_m clusters, respectively. Substituting equation 5.5 in equation 5.4 yields

$$S = (1 - f_t) \cdot S_{ref} + f_t \cdot (f_{d1} \cdot S_{d1} + f_{d2} \cdot S_{d2}) \tag{5.6}$$

and, in a similar manner, the *W* parameter is given by

$$W = (1 - f_t) \cdot W_{ref} + f_t \cdot (f_{d1} \cdot W_{d1} + f_{d2} \cdot W_{d2}) \tag{5.7}$$

where W_{d1} denotes the *W* parameter of small V_m clusters, and W_{d2} denotes the *W* parameter of large V_m clusters.

To model the experimental data let us start by considering that the defects created during the 10^{14} He/cm^2 implantation are solely small V_m clusters ($f_{d2} = 0$). Looking at figure 5.10, a straight line can be drawn from the reference point passing through the *S,W* value of this low dose implantation. This line represents the *S,W* values associated with the presence of small V_m clusters. With increasing concentration of this type of defects the *S,W* points shift towards higher *S*, lower *W* values. A second line can be traced to represent the large V_m clusters. The position of the *S,W* line for large vacancy clusters is deduced from the work by Kruseman on aluminum alloys [10]. By annealing an aluminum alloy and measuring it with PADB at the annealing temperature, Kruseman has determined the relative position of the *S,W* point associated with divacancies with that of vacancies [10]. Two *S,W* points defined for Eurofer97, #1 and #2, were added to figure 5.10 for clarity. Based on these S,W points in relation to the measured *S,W* values of the various implantation doses, a fitting line was traced based on equation 5.6 (full line in figure 5.10). The position of this line was obtained with the help of the *S,W* values of points #1 (S^1, W^1) and #2 (S^2, W^2). The fitted line was calculated considering that, up to the dose of 10^{14} He/cm^2, all positrons annihilating in defects in would do so in small vacancy clusters ($f_t = f_{d1}$). For doses higher than 10^{14} He/cm^2, a fraction of the positrons annihilating in defects would progressively start to do so also in larger vacancy clusters, of which the density would increase for higher implantation doses. The modeled line represents the increase in density and size of the clusters of vacancies formed during implantation. This line is shown in all *S,W* plots referring to the annealing of ion-beam implanted samples for comparison.

On the basis of the implantations done at 2 MeV (figure 5.10 and 5.11A), the implantations done at 350 keV and 500 keV shown in figures 5.11B and 5.11C, respectively, can be understood. Looking at the *S,W* points of these lower energy implantations it becomes clear that, although these positron implantation curves require two layers to fit the damaged regions (as opposed to the 2 MeV samples where only L_1 is used), the *S,W* values for both L_1 and L_2 follow the line derived for the 2 MeV samples. For both implantation energies, 350 keV and 500 keV, the implantation doses of 10^{14} and 10^{15} He/cm^2 result in an L_1 point located to the left (lower *S*, higher *W*) of the point representing the L_2 layer. In the samples implanted with higher doses of 10^{16} and 10^{17} He/cm^2, the L_1 point is located to the right (higher *S* and lower *W*) of the point representing the L_2 layer.

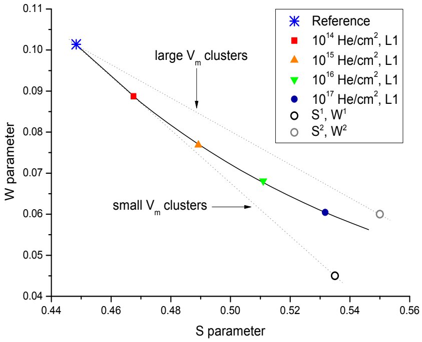

Figure 5.10 *Fitted line to equation (5.6) representing the increase of density and size of the clusters of vacancies formed during implantation. The plotted data refers to the PADB measurements of 2 MeV helium implanted Eurofer97 samples.* S^1,W^1 *and* S^2,W^2 *points help define the direction of the S,W lines associated with small and large vacancy clusters, respectively. The direction of the small-clusters was defined with the help of the* 10^{14} *He/cm*^{2} *S,W point.*

As expected from TRIM calculations the implantation at 350 keV and a dose of 10^{14} He/cm^2 (figure 5.11B) results in a higher density of defects in L_2 than in L_1. The implantation defects for the L_2 layer reflect the presence of helium in a very low density (consequence of a low implantation dose). For the doses of 10^{16} and 10^{17} He/cm^2, larger defects are formed. With the increasing density of implanted helium ions, it becomes probable that the defects formed in L_2 contain a higher He/V ratio than the L_1 layer. This is likely the cause for the change in *S,W* values of L_2 with respect to L_1, observed also for the 500 keV implantations. The He present in the clusters will lower the open volume available for positrons to annihilate and the clusters will be sensed by positrons as if they had a smaller size. At the intermediate dose of 10^{15} He/cm^2, the *S,W* points reflect a mixed character of low and high implantation doses defects.

The samples implanted with energy of 500 keV (figure 5.11C) show a similar trend to those implanted with 350 keV (figure 5.11B). Again, the L_1 and L_2 *S,W* points are on the curved line. The relative positions of L_1 to L_2 are the same as in the 350 keV samples. The *S,W* values of the sample implanted with 10^{17} He/cm^2 are surprising: a lower *S* value and a higher *W* parameter than that of the 10^{16} He/cm^2 sample is observed, whereas a higher *S* and lower *W* values were expected. Although the implantations were aimed to be done at room temperature, it is possible that, for this sample, the implantation temperature was higher than 300 K. If so, a partial annealing of the clusters that should have been formed during the implantation might take place, i.e. if the implantation temperature increases, the dissociation energy of some of the He_nV_m clusters is reached during the implantation itself and He is not trapped.

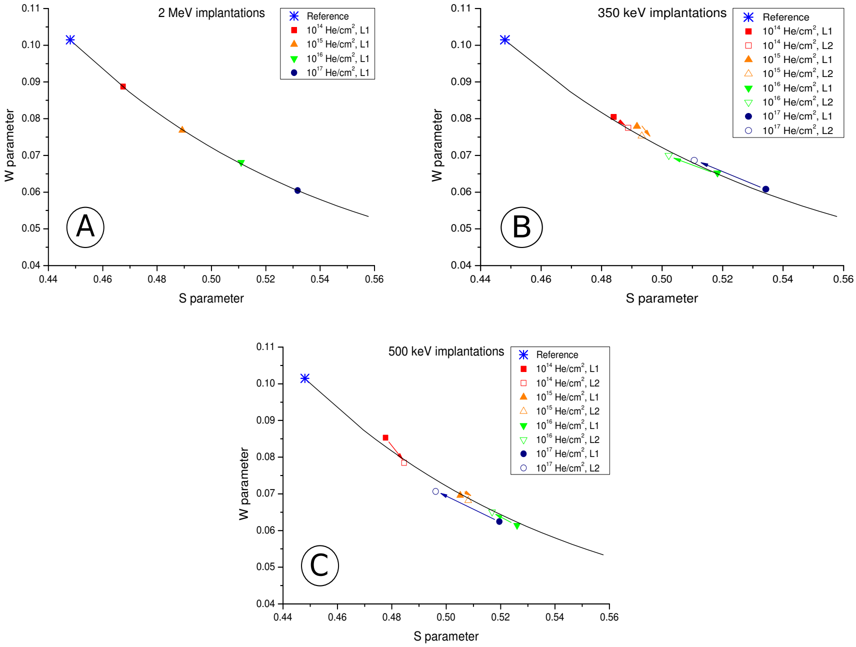

Figure 5.11 *PADB of helium implanted Eurofer97. A – Implantation energy 2 MeV. B - Implantation energy 350 keV. C - Implantation energy 500 keV. The reference S,W point is represented by a blue asterisk. The fitted line represents the increase of density and size of the clusters of vacancies formed during implantation. The layer 1 (L_1) is represented by full symbols and is related to a low He/V ratio. The layer 2 (L2) is represented by open symbols and is related to a high He/V ratio. The error of the fits is smaller than size of the symbols. The arrows indicate the differences between the S,W parameters for L_1 and L_2.*

A scheme representing the location of He_nV_m clusters in the modeled line is shown in figure 5.12. Considering two defect clusters with the same number of vacancies, the one that has a higher number of He ions will have a smaller open volume for positron to annihilate at. That said, He_nV_m clusters with a high He/V ratio will have *S,W* points with low *S* and high *W* values. On the contrary, defect clusters with a low He/V ratio will have *S,W* points with high *S* and low *W* values.

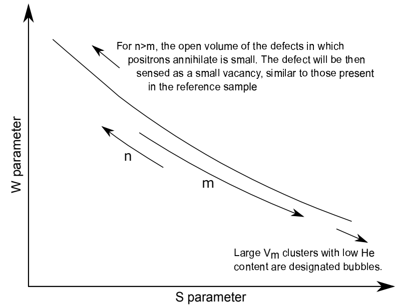

Figure 5.12 *Schematic interpretation of the line defined in figure 5.11.*

5.3.3 Annealing studies of ion-beam implanted samples

With the goal of observing the evolution of the implantation induced defects with increasing temperature, the samples were step-annealed up to 1500 K. The PADB measurements were done at room temperature, after oven cooling of the samples. All the *S*-*W* plots shown in this section include the curved line discussed in figure 5.10, describing the increase of density and the type of defect clusters.

5.3.3.1 Annealing study of 2 MeV implanted samples

As previously mentioned, the region probed by positrons in Eurofer97 steel after helium implantation with energy of 2 MeV has a low He/V ratio. As most of the implanted He is located at ~ 3 µm depth, the initial defects probed by positrons are mostly empty V_m clusters of which the concentration and size increase with dose. Figure 5.13 shows the *S,W* plots of the PADB measurements after each annealing step, where some *S,W* points are marked with their respective annealing temperature.

Figure 5.13A refers to the annealing of the sample implanted with 10^{14} He/cm^2. This sample was annealed up to 800 K. As the temperature increases, the *S,W* points move into the direction of the reference point, reflecting a gradual annealing of V_m clusters [4]. In fact, the *S,W* point reflecting the annealing at 600 K coincides with the *S,W* point of the reference (the reference point is based on the annealing of this sample at a temperature of 800 K). It can be concluded that at 600

K the defects created during implantation at depths probed by positrons are annealed.

Figure 5.13B shows the annealing of the sample implanted with 10^{15} He/cm^2. At room temperature this sample is expected to contain only V_m clusters in the region probed by positrons. The *S,W* point referring to the 800 K annealing is the closest to the reference Eurofer97 *S,W* point and associated with the annealing of V_m clusters [4]. For temperatures above 800 K, the trends observed in the *S* and *W* parameters are schematically shown in figure 5.14A. In the annealing step form 800 K to 900 K an increase of the *S* and decrease of the *W* values is noticed. After the annealing of vacancy clusters, the positrons will annihilate at He_nV_m clusters present in the matrix. The increase of *S* and decrease of *W* values is explained by the release of He from these clusters, which, according to the work by Morishita *et al.*, should have a dissociation energy in the range 2.5 – 3 eV [4]. In the range 900 – 1100 K the *S,W* points move in the direction of the reference. The *S,W* point referring to the annealing at 1200 K reflects the phase transition of the Eurofer97 at 1163 K (the phase diagram of Eurofer97 is shown in figure 4.1) and the reorganization of grain boundaries that it implies. During the phase transition a partial removal of defects takes place. The 1200 K *S,W* point also reflects the presence of stable He_nV_m clusters, with a He/V ratio of ~ 1.8 [4]. The presence of He ions at depths probed by positrons is explained by the dissociation of He_nV_m with a higher He/V ratio and subsequent diffusion of He towards to the probed region. At temperatures above ~ 1200 K the formation of bubbles takes place via Ostwald ripening and/or coalescence phenomena. At 1500 K the matrix should contain a small density of large He_nV_m clusters [6,7]. The *S* and *W* values of the annealings at 1400 K and 1500 K shift in the direction of the reference sample, indicating the dissociation and/or diffusion of bubbles [6,7].

Figure 5.13C shows the annealing of the sample implanted with 10^{16} He/cm^2. At this dose, the implantation defects probed by positrons are V_m clusters and He_nV_m defects, with low He content. For temperatures above 700 K, the trends observed in the *S* and *W* parameters are schematically shown in figure 5.14B. The annealing at

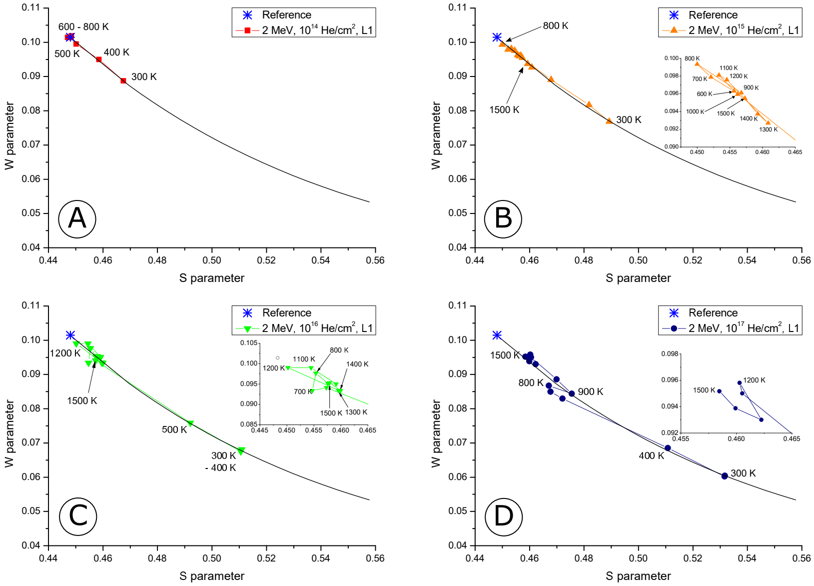

Figure 5.13 *PADB of helium implanted Eurofer97 with an energy of 2 MeV. The reference S,W point is represented by a blue asterisk. The line traced for all the plots refers to the increase of density and size of vacancy clusters during helium implantation. The samples were annealed up to 1500 K and the measurements are done after cooling, at room temperature. At room temperature, the defects probed by positrons in these samples are vacancy clusters. The data has been fitted with VEPFIT. The error of the fits is smaller than the size of the symbols.*

700 K/ 800 K yields an *S,W* point towards the reference values. This shift is explained by the annealing of the vacancies that takes place up to ~ 800 K [4]. Furthermore, the *S,W* point referring to the annealing at 700 K shows a shift towards a lower *W* value than that of the 600 K annealing. According to Eldrup [2] this shift is explained by the presence of He_nV_m clusters. Up to 1000 - 1100 K the dissociation of He_nV_m clusters with a dissociation energy lower than ~ 3 eV takes place. Although the defect clusters sensed by positrons contain helium ions, their *S,W* characteristic values are close to those of the reference and similar to the characteristic parameters of small vacancy clusters. A possible explanation is that the He content in the clusters reduces the open volume in which the positrons annihilate, and the defects are sensed as if they were constituted by a small number of vacancies. The *S,W* point of the annealing at 1200 K echoes the phase transition of the Eurofer97 (1163 K), and the presence of He_nV_m clusters with a He/V ratio of ~ 1.8 [3,4,11]. At temperatures above 1200 K, the formation of bubbles is expected to take place due

to Ostwald ripening and/or coarsening phenomena and the density of defects present in the matrix decreases. The S and W values of the annealings above 1200 K show a shift towards the reference. At 1500 K, it is expected that the matrix contain a small quantity of large bubbles [6,7].

The effect of annealing of the Eurofer97 sample implanted with 10^{17} He/cm^2 (figure 5.13D) is similar to that of the sample implanted with 10^{16} He/cm^2. A significant annealing of vacancy clusters occurs in the annealings up to ~ 800 K [4]. The S,W values after annealing at 800 K reflect the presence of He_nV_m clusters with $n \approx m$ [2]. The 900 K S,W point is associated with the dissociation of He_nV_m clusters with $n < m$. The S,W point of the annealing at 1200 K reflects the phase transition of Eurofer97 (1163 K) and the dissociation of He_2V [3,11]. As the temperature increases to 1500 K, Ostwald ripening and/or coarsening of defects takes place, and the helium contained in the defect clusters is released [5,12]. An increase of size and decrease of density of the positron traps is noticed. The S,W values at 1500 K are characteristic of a low density of large He_nV_m clusters (bubbles) [6,7].

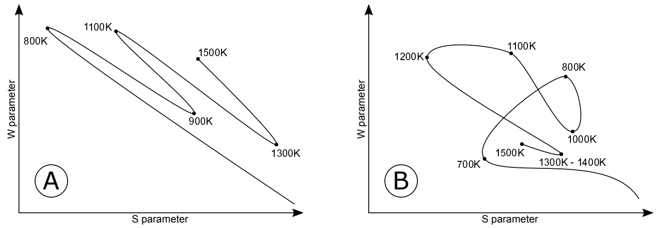

Figure 5.14 Scheme of the trends observed in the S and W parameters for 2 MeV samples implanted with: A – 10^{15} He/cm^2, B - 10^{16} He/cm^2.

5.3.3.2 Annealing study of 350 keV samples

Figure 5.15 shows the annealing study of the samples implanted with helium ions with an energy of 350 keV. In these samples positrons probe a region of low He/V ratio, the L_1 layer, and one of a high He/V ratio, the L_2 layer. The S,W plots shown in figures 5.15A, C, E and G refer to the L_1 layer. The trend observed for the S,W points of the annealings is similar to that of the 2 MeV samples. The interpretation of these figures is comparable to that described in the previous section (annealing of the 2 MeV samples, figure 5.13) and will not be repeated here. The differences in the position of the *S,W* points can be attributed to the higher content of He in layer L_1 of the 350 keV samples than that of the 2 MeV implanted Eurofer. The higher density of helium ions in L_1 will delay the annealing of the defect clusters and the shift of the *S,W* pairs towards the unimplanted reference only at higher temperatures. Layer L_2, having a high He/V ratio, is expected to contain He_nV_m clusters. The size of these clusters is dependent on the implantation dose – the higher the implantation dose, the higher the number of Frenkel pairs formed during implantation and the higher the number of He ions present in the vacancy clusters.

Figure 5.15B shows the *S,W* plot of the L_2 layer of the sample implanted with a dose of 10^{14} He/cm^2. It is noticed that at 800 K, the highest annealing temperature of this sample, the *S,W* pair does not reach the reference values. The shift observed from 300 K to 800 K towards a lower *S* and higher *W* reflects the annealing of the empty vacancy clusters present in layer L_2 and the presence of He_nV_m clusters with a He/V ratio higher than 4 [4] in the matrix.

The *S,W* plot of the L_2 layer of the sample implanted with 10^{15} He/cm^2 (figure 5.15D) shows a shift towards lower *S* and *W* values in the annealing steps from 400 K to 500 K. This is associated with the dissociation of V_m clusters [4] present in L_2 and the presence of He_nV_m clusters [2]. At 800 K the *S* and *W* values shift in a direction away from the reference, similar to what was observed for the 2 MeV, 10^{15} He/cm^2 sample. The increase of the annealing temperature to 1250 K promotes dissociation of He_nV_m clusters with a He/V ratio higher than ~ 1.8 [3,4,11], shifting the *S,W* pairs in the direction of the reference. The *S,W* point of the annealing at 1250 K also reflects the phase transition of Eurofer97. The trend of the *S,W* values of this sample is similar to that of the 2 MeV sample implanted with 10^{16} He/cm^2 (schematically shown in figure 5.14B).

The *S,W* plot of the annealing of the L_2 layer of the 10^{16} He/cm^2 sample is presented in figure 5.15F. The *S,W* point regarding the annealing at 500 K reflects the presence of He_nV_m clusters with $n > m$ [2]. Up to ~ 800 K the annealing of vacancy clusters takes place [4]. It is noticed that above 500 K the *S,W* pairs

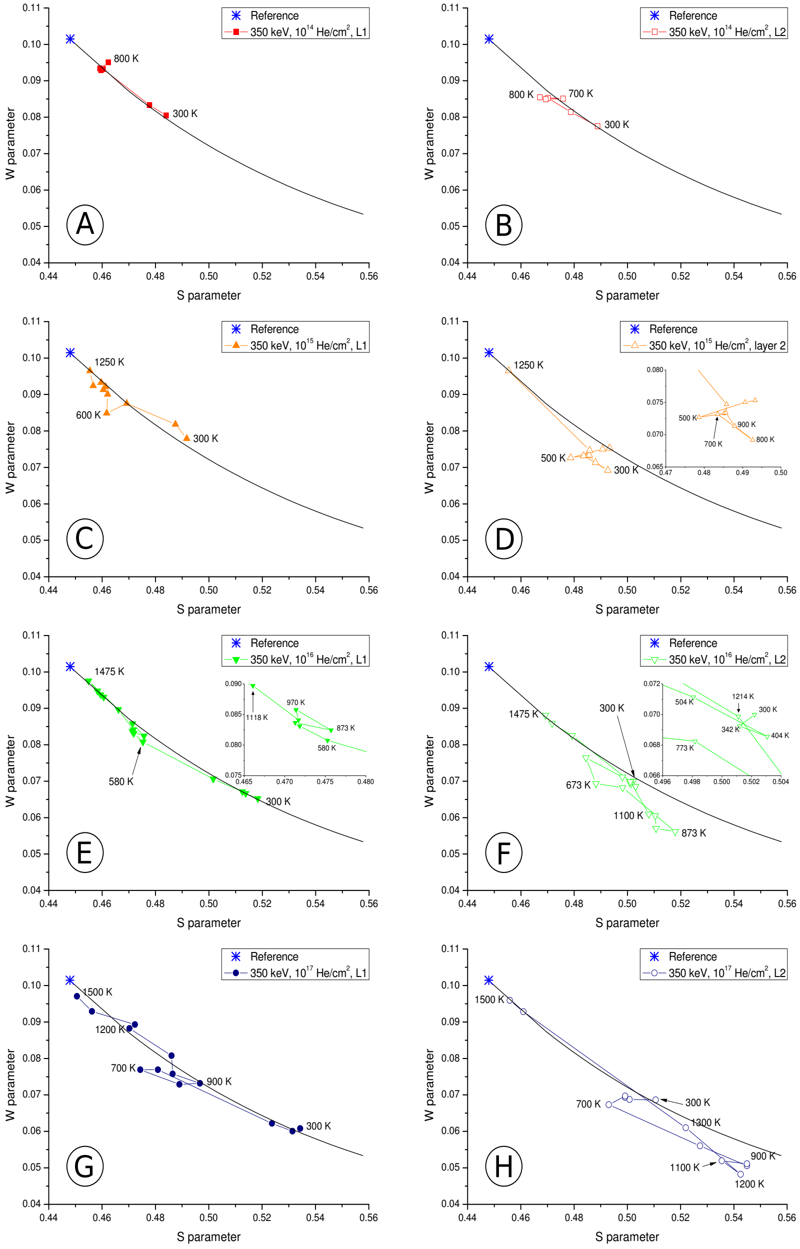

Figure 5.15 *PADB of helium implanted Eurofer97 with an energy of 350 keV. The reference S,W point is represented by a blue asterisk. The line traced for all the plots refers to the increase of density and size of vacancy clusters during helium implantation. The samples were annealed up to 1500 K and the measurements are done after cooling, at room temperature. At*

room temperature, the defects probed by positrons in these samples are vacancy clusters and He_nV_m *clusters. The data has been fitted with VEPFIT. The error of the fits is smaller than the size of the symbols. The reference S,W point is represented by a blue cross.*

decrease both their *S* and *W* values, up to 873 K. This decrease is explained similarly to the step between 800 K and 900 K observed for the 2 MeV, 10^{15} He/cm^2 sample. In the temperature range 500 K – 873 K, the dissociation of clusters with a dissociation energy in the range 2.5 – 3 eV [4] is expected. The increase of the annealing temperature to 1000 – 1200 K shifts the *S,W* pairs in the direction of the reference.

The *S,W* point of the annealing at 1200 K reflects the phase transition of Eurofer97 (1163 K) and the dissociation of He_nV_m clusters with a He/V ratio of ~ 1.8 [3,4,11]. The phase transition will generate a reorganization of grain boundaries and the annealing of some defect structures present in the matrix. At temperatures above 1300 K coalescence and/or Ostwald ripening of defects takes place. This will result in an increase of size and decrease of density of the positron traps. The *S,W* pair after annealing at 1475 K is related to the presence of bubbles (large defect clusters) in Eurofer97 [6,7]. The trend of the *S,W* values of this sample is similar to that of the 2 MeV sample implanted with 10^{15} He/cm^2 (schematically shown in figure 5.14A).

The *S,W* plot of the L_2 layer of the sample implanted with 10^{17} He/cm^2 is shown in figure 5.15H. The annealing behavior of the layer L_2 of this sample is qualitatively the same as that of the 10^{16} He/cm^2 sample. The higher implantation dose leads to a higher concentration of defects that leads to higher *S* and lower *W* values.

5.3.3.3 Annealing study of 500 keV samples

The annealing study of the 500 keV implanted Eurofer97 steel is shown in figure 5.16. As in the case of the samples implanted with 350 keV, positrons probe a region of low He/V ratio, designated layer L_1, and one of a high He/V ratio, designated layer L_2. The *S,W* plot of the layer L_1 is shown in figures 5.16A,C,E and G and is similar to those of the 350 keV samples (figures 5.15A,C,E and G) and to the 2 MeV samples (for the 2 Mev implantations positrons can only probe a region with low He/V ratio, figure 5.13). Layer L_2 has a higher He/V ratio than layer $L_{1.}$ L_2 contains He_nV_m clusters and their size increases with increasing implantation dose.

Figure 5.16B shows the S,W plot of the L_2 layer of the sample implanted with 10^{14} He/cm^2. The S,W points up to 500 K move in the direction of the reference and are associated with the annealing of V_m clusters [4]. The S,W value of the 600 K annealing shows a shift to lower W and higher S values, reflecting the presence of He_nV_m clusters with $n > m$ [2].

The S,W plot of the sample implanted with 10^{15} He/cm^2 at 500 keV (figure 5.16D) shows a distinct behavior of the L_2 layer in comparison to that of the 350 keV implanted samples. Up to 800 K the S,W pairs move in the direction of the reference, indicating the annealing of V_m clusters takes place [4]. The annealings at 900 K and 1000 K shift the S,W pairs in the direction of higher S and lower W values and are related to the dissociation of He_nV_m clusters. As the clusters dissociate and vacancies and He ions are released into the matrix, some of the defects will be retrapped at more stable clusters. As the temperature increases towards the phase transition temperature, 1163 K, the S,W points move towards the unimplanted reference. As in the other ion-beam implanted samples, the reorganization of grain boundaries taking place during the phase transition results in the annealing of some defect structures present in the matrix. The S,W point of the annealing at 1200 K reflects the phase transition of Eurofer97 (1163 K) and the dissociation of He_nV_m clusters with a He/V ratio of ~ 1.8 [3,4,11]. Above 1200 K the coalescence and/or Ostwald ripening of defects takes place and bubbles are formed. This will result in an increase of size and decrease of density of the positron traps. The S,W pairs move in the direction of the reference up to 1500 K, reflecting the dissociation and/or diffusion of bubbles [6,7]. The trend of the S,W values of this sample is similar to that of the 2 MeV sample implanted with 10^{15} He/cm^2 (schematically shown in figure 5.14A).

The S,W plot after annealing of the sample implanted with a dose of 10^{16} He/cm^2 is shown in figure 5.16F. The behavior of the S,W is qualitatively the same as in the sample implanted with 500 keV and 10^{15} He/cm^2 (figure 5.16D), discussed in the previous paragraph. Similarly, the annealing of the sample implanted with 500 keV and 10^{17} He/cm^2, shown in figure 5.16H, also resembles that of the implantation with 350 keV and a dose of 10^{17} He/cm^2 (figure 5.15H).

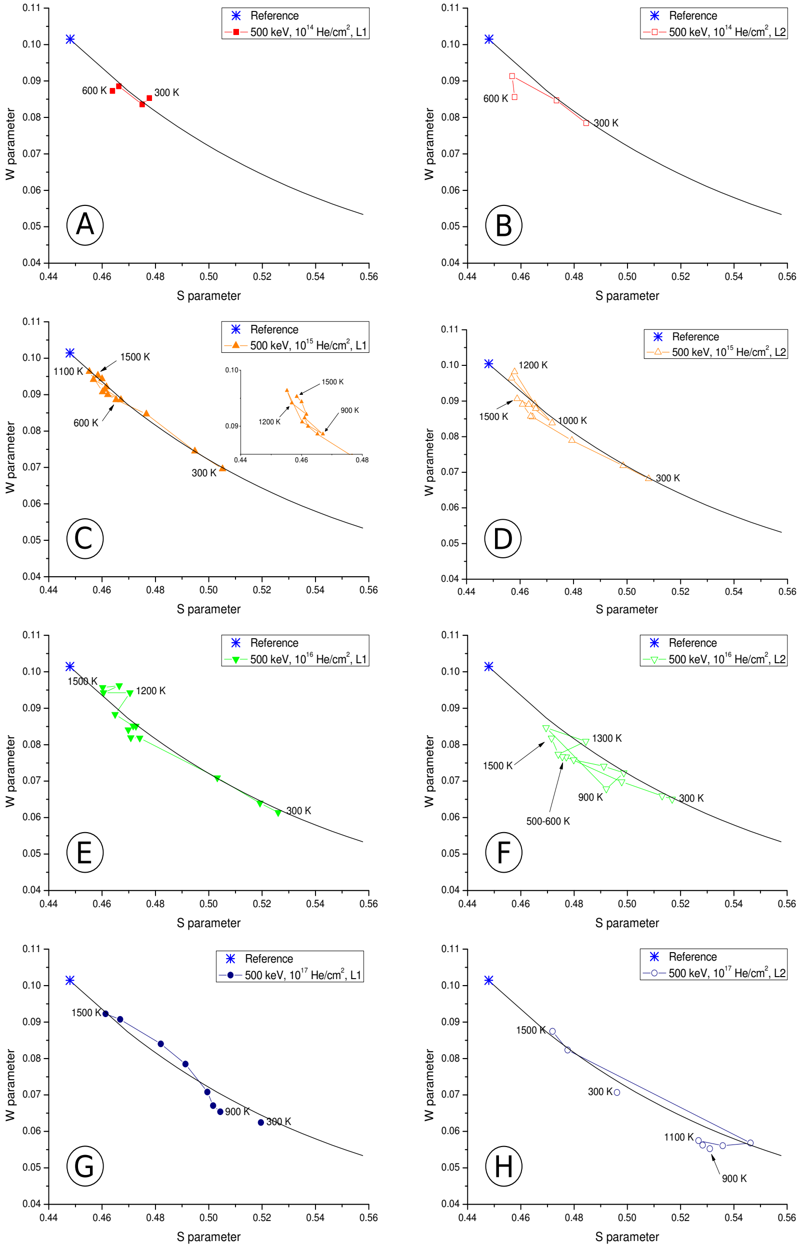

Figure 5.16 *PADB of helium implanted Eurofer97 with an energy of 500 keV. The reference S,W point is represented by a blue asterisk. The line traced for all the plots refers to the increase of density and size of vacancy clusters during helium implantation. The samples were annealed up to 1500 K and the measurements are done after cooling, at room temperature. At*

room temperature, the defects probed by positrons in these samples are vacancy clusters and He_nV_m *clusters. The data has been fitted with VEPFIT. The error of the fits is smaller than the size of the symbols. The reference S,W point is represented by a blue cross.*

5.4 Thermal desorption spectroscopy analysis

To study the thermal stability of the defects created during the helium implantation of Eurofer97, the samples implanted with 500 keV and 2 MeV were measured with thermal desorption spectroscopy. The spectra obtained are shown in figure 5.17. In the TDS set-up used the samples were linearly heated up to 1500 K at a rate of 0.33 K/s. The sharpest peak observed in TDS spectra is believed to be related to the phase transition of ferrite into austenite and therefore corrected to the temperature of 1163 K (peak marked IV in figure 5.17; a phase diagram of Eurofer97 is presented in chapter 4, figure 4.1). A linear correction is used for the other temperature values. As for plasma implantations, no background subtraction is performed for these spectra. Before each measurement the system was baked out overnight at a temperature of 470 K to reduce the background signal. The horizontal axis at the top of the graphs represents the dissociation energy corresponding to the annealing temperature at the bottom axis. The dissociation energy is the energy necessary for He desorption from defect structures. This concept is schematically shown in chapter 3, figure 3.12. Further details on how to calculate the dissociation energy are discussed on section 5.2.3. of this chapter. It was noticed that the peak at 1163 K was clipped by the quadrupole the samples implanted with a dose of 10^{17} He/cm^2. These peaks have been reconstructed and their height increased by approximately 10 %.

From the spectra in figure 5.17 three peaks are identified and are marked as I, II and III. Peak I is located at ~ 900 K and is probably related to the dissociation of He_nV_m clusters with a He/V ratio in the range 3 - 4. Peak II, located at 1163 K, is related to the phase transition of Eurofer97 steel and the dissociation of He_nV_m clusters with a He/V ratio of ~1.8 [5]. Peak III, actually defined as the region above 1300 K, is probably related to the dissociation of bubbles, taking place at high annealing temperatures [6,7].

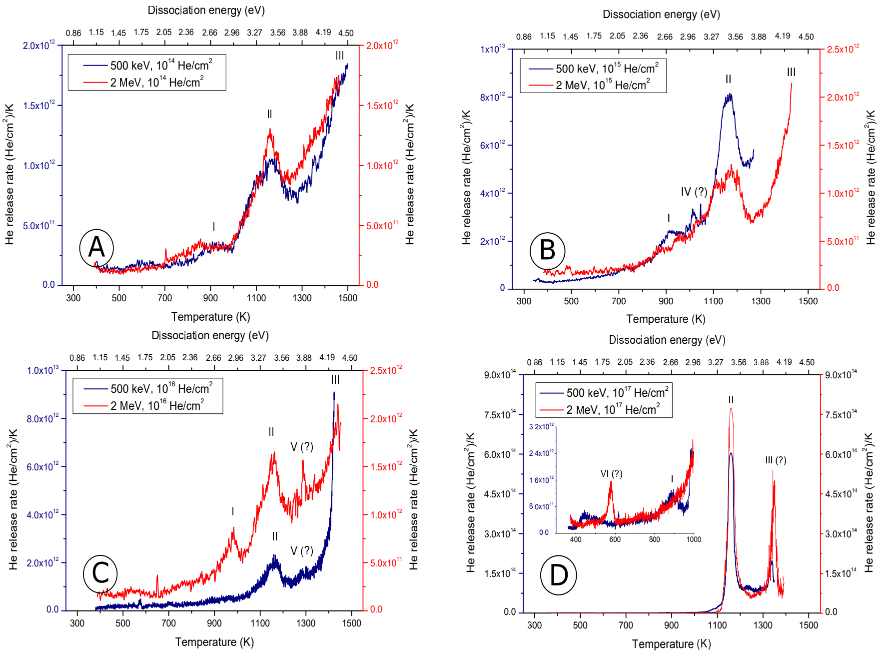

Figure 5.17 *TDS measurements of the Eurofer97 He implanted samples with an energy of 500 keV (blue lines) and 2 MeV (red lines). No background subtraction is performed on the spectra. The inset on figure 5.17D refers to the helium release of the 10^{17} He/cm^2 samples taking place at temperatures up to 1000 K.*

Other peaks can be identified in the spectra, although not clearly: peak IV (figure 5.17B, 500 keV sample), peak V (figure 5.17C), and peak VI (inset on figure 5.17D, 2 MeV sample). Peak IV is only observed in the 500 keV implanted sample. It is located in the interval 1000 K - 1100 K and has a dissociation energy of ~ 3 eV. This peak is possibly related to the onset of the phase transition and the beginning of the reorganization of grain boundaries and removal of defects. Peak V is located at 1300 K and it can be argued that it overlaps with the beginning of peak (region) III. As previously discussed, above 1200 K Ostwald ripening and/or coalescence of defects takes place. It is possible that peak V is related to these phenomena, but no clear association can be established. Finally, peak VI is observed solely for the 2 MeV implanted sample and is located in the range 500 K - 600 K. The location of this peak is the same as the peak I, identified for the plasma implanted samples (figure 5.6). Peak VI is likely associated with desorption from He_nV_m clusters with a dissociation energy of ~ 1.3 eV and a He/V ratio above 4. The reason why peaks IV, V and VI are not observed for all spectra is not clear, as all samples undergo the same sequence of helium release phenomena.

The calculated total amount of He desorbed is approximately 2 % of the implanted dose for all samples. This low value of He retention in Eurofer97 cannot be explained at the moment.

5.5 Discussion

In order to understand the evolution of defects with increasing temperature, it is important to know which defects are expected immediately after implantation. Figure 5.18 shows a scheme of the defects present in an implanted sample. At 300 K there should be vacancy clusters (V_m), helium-vacancy clusters (He_nV_m with $n > m$), and small He_nV clusters present. Due to the depth distribution of the helium ions during implantation, most He_nV_m clusters are expected to form in the region around the maxima of the He implantation (~ 1 μm for 350 keV and 500 keV samples and ~ 3 μm for 2 MeV samples, figure 5.8). The highest density of the V_m clusters is expected to be located at depths below the maxima of He implantation, in a region of low He/V ratio. Due to the very low migration energy of He, $E_{He}^{m} \sim 0.05 - 0.08$ eV [4,13], no helium ions are expected to be present in interstitial positions at room temperature, since they can migrate to vacancies or other traps, or leave the sample.

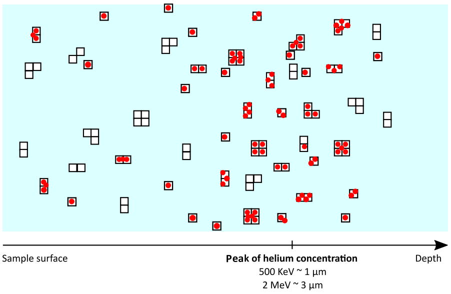

Figure 5.18 *Implantation induced defects in Eurofer97. Defects present in the sample at 300 K: vacancy clusters (V_m), helium-vacancy clusters (He_nV_m with n > m) and small He_nV clusters. The open squares represent vacancies and the red circles represent helium ions.*

As annealing of the implanted samples starts, the dissociation of He_nV_m clusters takes place and He is released. Alternatively, the dissociation of the clusters can be delayed by the attachment of vacancies present in the matrix. These vacancies can be present in the matrix as a consequence of the dissociation of V_m clusters (taking place up to ~ 800 K [4]). The delay of He release from the defect clusters due to the attachment of vacancies is valid for the whole TDS measurement. The retrapping of He or V by stable He_nV_m clusters can also take place.

The following descriptions for the defect behavior with increasing annealing temperature are based on the *S* parameters obtained for the ion implanted samples with a dose of 10^{15} and 10^{16} He/cm^2. The reason for this is that although the trends observed for the *S* parameter are the same for all implanted samples, these changes do not take place at the same temperatures. However, it should be kept in mind that the helium release mechanisms explained below are valid for all samples, even if taking place at slightly higher or lower temperatures. A scheme of the phenomena taking place in the matrix with increasing temperature is shown in figure 5.19 and can be followed during the discussion of results.

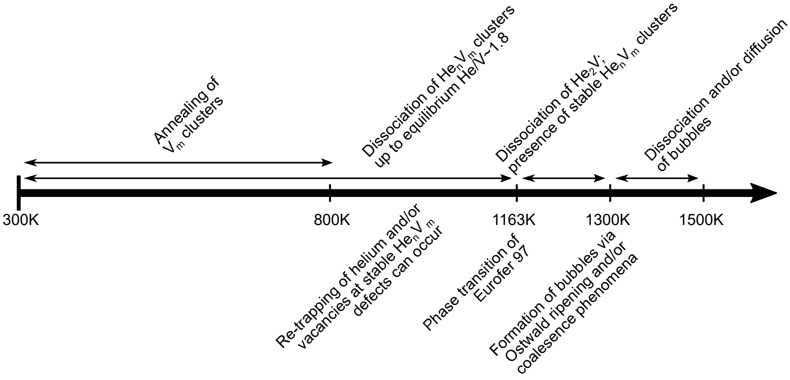

Figure 5.19 *Scheme of the phenomena taking place in the matrix with increasing temperature.*

Let us start by looking at the temperature range 300 K to 800 K. The annealing of the samples at up to 800 K promotes the dissociation of the V_m clusters [4]. This decrease of positron traps is observed in the annealing study of the 2 MeV samples (figure 5.13) as the PADB measurements of these samples reflect a region with low He/V ratio (layer L_1), far away from the He peak. The TDS spectra up to 800 K (ion implanted samples, shown in figure 5.17) show a small amount of helium release from the samples, indicating that the dissociation of vacancy clusters is the main phenomenon to consider in this temperature range. The low He release for the

300 K - 800 K temperature range can be explained by the dissociation of He_nV_m clusters with a He/V ratio higher than 4 [4]. However, as vacancies present in the matrix aggregate to these clusters, the He release is delayed. Another possibility is that the He is in fact released from the He_nV_m clusters but re-trapped in He_nV_m clusters with a lower He/V ratio. At 800 K the PADB measurements reflect a decrease in the density of positron traps accompanied by an increase in the trap size. Schematics of the phenomena taking place up to 800 K are shown in figure 5.20. The defect evolution up to 800 K is schematically shown in figure 5.21.

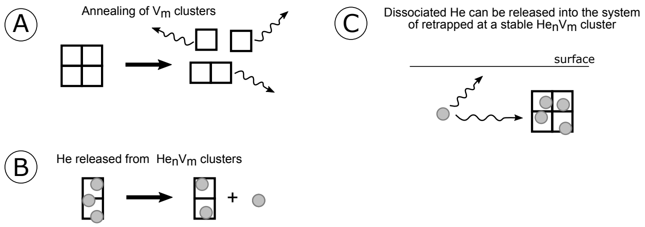

Figure 5.20 *Scheme representing A: the annealing of vacancy clusters, B: the He being released from He_nV_m clusters, C: the possible paths of desorbed He – to be released into the surface or to be retrapped at a stable He_nV_m cluster that can still accommodate more He ions.*

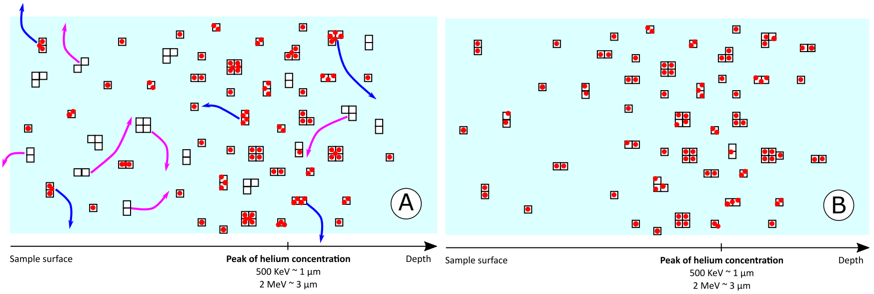

Figure 5.21 *A: scheme of the movement of defects below 800 K: the blue arrows represent the helium release and the purple arrows represent the vacancies movement. Annealing of vacancies and vacancy clusters takes place, as well as desorption of helium from He_nV_m ($n > m$) clusters. B: defects present in the sample at 800 K.*

The next temperature range to consider is between 800 K and 1000 K. This temperature range is marked by the dissociation of He_nV_m clusters with a He/V ratio in the range 3 - 4 [5] (figure 5.21B). The aggregation of vacancies to the clusters is possible and, if so, the release of He will be delayed. Retrapping of helium or vacancies at defect clusters is possible. The He released from the clusters can either contribute to the TDS spectra shown in figure 5.17, or become trapped in clusters with a higher dissociation energy before reaching the sample's surface (figure 5.21C). The stronger TDS signal of the 500 keV samples in comparison to that of the 2 MeV samples is explained by the location of the helium in the sample – approximately 1 μm and 3 μm depth, respectively. The defect evolution up to 1000 K is schematically shown in figure 5.22.

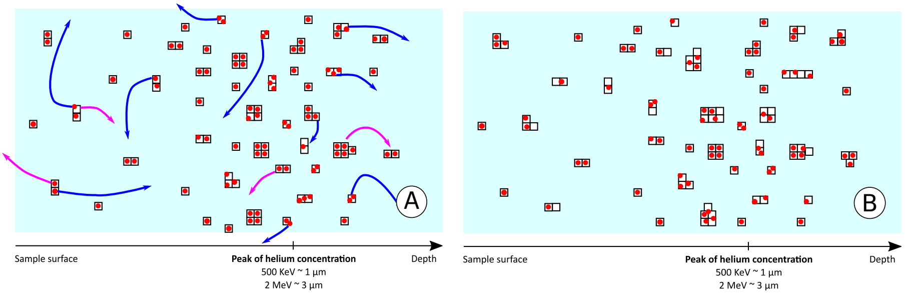

Figure 5.22 *A: schematics of the movement of defects in the range 800 – 1000 K: the blue arrows represent the helium release and the purple arrows represent the vacancies movement. Dissociation of* He_nV_m *clusters. The helium released might reach the surface of the sample and contribute to the TDS spectrum or be retrapped in a stable* He_nV_m *clusters that can still accommodate more ions. B: defects present in the sample at 1000 K.*

As the temperature increases to 1200 K the phase transition of Eurofer97 takes place (1163 K [14]) and leads to a reorganization of the grain boundaries that, consequently, leads to a removal of defects. Coincidently, the dissociation energies associated with this temperature range are of 2.96 eV to 3.27 eV, characteristic of the dissociation of He_nV_m clusters with a He/V ratio of ~ 1.8 [4], likely He_2V [5]. The dissociation of defect clusters is mostly present in the L_2 layer due to its high He/V ratio. As before, retrapping of helium and vacancies can occur.

For temperatures above 1200 K the TDS intensity increases significantly until the end of the measurement, Ostwald ripening and/or coalescence of defects can occur and the formation of bubbles takes place (figure 5.23). Above 1300 K the He release from the bubbles via dissociation and/or bubble diffusion mechanism [6,7,15] can occur, with both phenomena promoting increase of the dissociation energy of the cluster. The distinction between the two mechanisms cannot be clearly made by these measurements. The movement of the helium bubbles is schematically shown in figure 5.24.

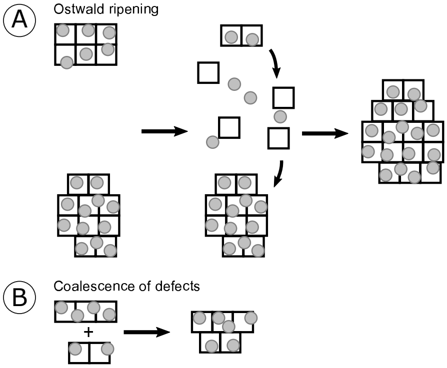

Figure 5.23 *Scheme representing A: Ostwald ripening phenomena, where smaller clusters dissociate and the He and the vacancies are absorbed by the larger clusters, B: coalescence of defects.*

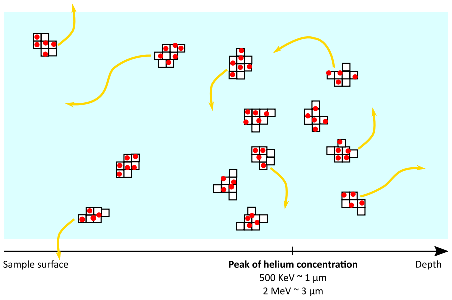

Figure 5.24 *Schematics of the movement of defects for temperatures above 1300 K. The yellow arrows represent the movement of the bubbles.*

5.6 Conclusions

With the goal of mimicking the transmutation of He in Eurofer97, this material was helium implanted using two different methods: plasma implantation and ion beam implantation. After the implantations, the material was analyzed with PADB and TDS.

Eurofer97 was He plasma implanted with different initial conditions: set A in the as-received conditions and set B after annealing at 1200 K for 1 h. An implantation energy of 3 keV was used for both sets. From each set, one of the samples was implanted at 10^{18} He/cm^2 and the other with 10^{19} He/cm^2. Within each set, one of the samples was implanted at a low temperature (375 K) and the other at a high temperature (450 K and 525 K, depending on the set). PADB measurements show that the implantations create damage up to a depth of 30 nm, a result that is consistent with TRIM calculations. Both samples of set A shows a decrease of the *S* parameter after implantation. This decrease is explained by a decrease of the fraction positron traps, as compared to the reference sample. It is foreseen that the positron traps are being filled with He during the implantations. PADB measurements of the samples in set B do not show a significant change in the *S* parameter for depths far beyond the He damage region. This is in agreement with the idea that set B has little pre-implantation defects and, once implanted, He will diffuse to depths beyond the positron diffusion length. The He release observed in the TDS spectra of the plasma implanted samples can be associated with the implantation temperature. While the samples implanted at 375 K release most of the retained helium below 1100 K, the samples implanted at 450 K and 525 K release the majority of its helium above that temperature.

The ion beam implantations were performed at 3 implantation energies: 350 keV, 500 keV and 2 MeV. The implantations were done with doses in the range 10^{14-17} He/cm^2. After implantation, the samples were step-annealed up to 1500 K. Each annealing step was followed by a PADB measurement. By plotting the *S,W* points after the different annealing treatments it is possible to understand the evolution of the defects created during the implantation with increasing temperature. The implanted samples were also measured with TDS. The results of the PADB and the TDS are consistent. Up to 800 K the dissociation of V_m clusters is concluded from the measurements. Above this temperature, the main phenomenon is the dissociation of He_nV_m clusters. As the temperature increases to 1100 K, He release from He_nV_m clusters with a He/V ratio lower than ~ 1.8 takes place. Since in parallel the formation of thermal vacancies takes place, some of these clusters will aggregate the newly formed vacancies and delay the release of helium. At 1200 K, two concurrent phenomena take place: the phase transition of Eurofer97 and the dissociation of He_nV_m clusters with a He/V ratio of ~ 1.8, likely He_2V. Above 1300 K, very large defect clusters (bubbles) will exist in the matrix. The release mechanism of He from bubbles is not clearly defined and can be attributed to the dissociation of bubbles and/or to bubble diffusion mechanism to the materials surface.

The TDS results with plasma implantations are in agreement with those of the ion implantations. Common He release temperatures are observed, independently of the implantation method: 900 K, 1200 K and release of He above 1300 K. The similarities found in the TDS spectra indicate that although the implantation temperature plays an important role in the He desorption from He_nV_m clusters, the phenomena behind the He release of the plasma implanted samples can be understood in the same way as that of the ion-beam implanted material.

Nomenclature

C	Concentration of defects	m^{-3}
E^d	Dissociation energy	eV
E^m_{He}	Migration energy of He	eV
f_{d1}	Fraction of positron annihilations in small vacancy clusters	
f_{d2}	Fraction of positron annihilations in large vacancy clusters	
f_t	Fraction of annihilations in defects	
He	Helium	
He/V	Helium-per-vacancy ratio	
He_nV_m	Helium-vacancy cluster	
k_B	Boltzmann constant	$m^2.kg.s^{-2}.K^{-1}$
L_1	First VEPFIT fitted layer	
L_2	Second VEPFIT fitted layer	
L_b	VEPFIT fitted layer representing the bulk	
S_1, W_1	*S* and *W* fitted values of layer L_1	
S^1, W^1	*S*,*W* values of point #1	
S_2, W_2	*S* and *W* fitted values of layer L_2	
S^2, W^2	*S*,*W* values of point #2	
S_b	*S* parameter of the bulk	
S_{b1}	Reference *S* value of the Eurofer97 plasma implanted samples	
S_d	*S* parameter of a region containing defects	
S_{d1}	*S* parameter of small vacancy clusters	
S_{d2}	*S* parameter of large vacancy clusters	

S_{ref}	Reference *S* parameter	
T	Annealing temperature	K
V	Vacancy	
$\mathrm{V_m}$	Vacancy cluster	
W_{b1}	Reference *W* value of the Eurofer97 plasma implanted samples	
W_{d1}	*W* parameter of small vacancy clusters	
W_{d2}	*W* parameter of large vacancy clusters	
β	Heating rate	$\mathrm{K.s^{-1}}$
λ_b	Positron annihilation rate at the bulk	$\mathrm{s^{-1}}$
ν	Positron trapping rate for defects	$\mathrm{s^{-1}}$
ν_f	Attempt frequency	$\mathrm{s^{-1}}$
EDM	Electro-discharge machining	
PADB	Positron annihilation Doppler broadening	
PKA	Primary knock-on atom	
TDS	Thermal desorption spectroscopy	

References

[1] J.F. Ziegler, TRIM - Transport of Ions in Matter, (2008). http://www.srim.org/.

[2] M. Eldrup, B.N. Singh, S.I. Golubov, Final Report on Investigations of the Influence of Helium Concentration and Implantation rate on Cavity Nucleation and Growth during Neutron Irradiation of Fe and EUROFER 97, 2010.

[3] D. Xu, B.D. Wirth, J. Nucl. Mater. 386-388 (2009) 395–399. doi:10.1016/j.jnucmat.2008.12.141.

[4] K. Morishita, R. Sugano, B.D. Wirth, T. Diaz de la Rubia, Nucl. Instruments Methods Phys. Res. Sect. B Beam Interact. with Mater. Atoms. 202 (2003) 76–81. doi:10.1016/S0168-583X(02)01832-3.

[5] K. Morishita, B.D. Wirth, T.D. De Rubia, A. Kimura, Effects of Helium on Radiation Damage Processes in Iron, (2001).

[6] K. Morishita, R. Sugano, H. Iwakiri, N. Yoshida, A. Kimura, Fourth Pacific Rim Int. Conf. Adv. Mater. Process., 2001.

[7] K.Z. Oo, I.I. Chernov, M.S. Staltsov, B.A. Kalin, A.N. Kalashnikov, S.Y. Binyukova, et al., 110 (2011) 130–137.

[8] D. Terentyev, N. Juslin, K. Nordlund, N. Sandberg, J. Appl. Phys. 105 (2009) 103509. doi:10.1063/1.3126709.

[9] M.J. Caturla, C.J. Ortiz, C.C. Fu, Comptes Rendus Phys. 9 (2008) 401–408. doi:10.1016/j.crhy.2007.09.004.

[10] A. Kruseman, Two-dimensional ACAR and low-background DBAR studies on materials with defects, PhD thesis, Delft University of Technology, 1999. doi:90-407-1880-6.

[11] D. Xu, T. Bus, S.C. Glade, B.D. Wirth, J. Nucl. Mater. 367-370 (2007) 483–488. doi:10.1016/j.jnucmat.2007.03.112.

[12] K. Morishita, R. Sugano, Modeling of He-bubble migration in bcc Fe, Nucl. Instruments Methods Phys. Res. Sect. B Beam Interact. with Mater. Atoms. 255 (2007) 52–56. doi:10.1016/j.nimb.2006.11.010.

[13] K. Morishita, R. Sugano, B.D. Wirth, MD and KMC modeling of the growth and shrinkage mechanisms of helium–vacancy clusters in Fe, J. Nucl. Mater. 323 (2003) 243–250. doi:10.1016/j.jnucmat.2003.08.019.

[14] M. Rieth, M. Schirra, A. Falkenstein, P. Graf, H. Heger, S., Kempe, R. Lindau, et al., Eurofer97 - Tensile, Charpy, Creep and Structural tests, 2003. doi:0947-8620.

[15] J. Gittus, Irradiation Effects in Crystalline Solids, Applied Science Publishers LTD, 1978.

Chapter 6

Neutron irradiation experiments

Based on:

- I. Carvalho, A. Fedorov, M. Kolluri, N. Luzginova, H. Schut, J. Sietsma proceedings of the 1st International conference on Ageing of Materials and Structures, Delft, 2014, ISBN: 974-94-6186-314-0

Eurofer97 was neutron irradiated under three different conditions: 2.4 displacements per atom (dpa) at 333 K, 1.9 dpa at 573 K and 8.0 dpa at 573 K. Transmission electron microscopy (TEM) samples were cut from the irradiated tensile specimens and the irradiation induced defects were identified. For the sample irradiated with 2.4 dpa and 333 K black dots with an average size of 7 nm were observed. For the other two conditions, black dots and dislocation loops were present. The average size of the defects for the sample irradiated with 1.9 dpa and 573 K shows a bi-modal distribution, with one peak at 9 nm and another at 17 nm. The defects present in the sample irradiated with 8.0 dpa and 573 K have an average size of 5 nm. Two conclusions can be drawn from the analysis of the TEM micrographs: the defect size increases with increasing irradiation temperature, and the defect size decreases with increasing irradiation dose. No He filled bubbles were observed in the TEM investigation. The irradiation hardening observed for the tensile specimens was investigated in terms of the obstacle strength (α), a parameter present in the hardening equation discussed in this chapter. The obstacle strength is believed to be related to the strength of the defects in stopping dislocation gliding. It is concluded that this parameter has a constant value of 0.22 for all irradiation conditions. This indicated that α is not dependent neither on the size of the obstacle nor on the dpa damage of the sample.

6.1 Introduction

Once in a fusion environment, materials must withstand high radiation levels and transmutation rates, high temperatures and high thermo-mechanical stresses. The fusion environment makes the development and characterization of structural materials very important topics of research.

Neutron irradiation of structural steels such as Eurofer97 will lead to severe damage of the material's matrix. The displacement of atoms from their lattice position will create Frenkel pairs (vacancies (V) and self-interstitial atoms (SIAs)) that may aggregate and form defect clusters such as dislocation loops and voids. In parallel, the transmutation of helium (He) gas from Nickel and Boron atoms takes place (further information on the transmutation reactions on chapter 2, section 2.2). The interaction of these gases with defect clusters will lead to the formation of helium bubbles. The presence of bubbles leads to irradiation swelling and embrittlement [1–3].

Several irradiation campaigns were conducted at the High-Flux Reactor (HFR), in Petten, to neutron irradiate Eurofer97 steel. The work in this chapter is focused on the irradiation conditions shown in table 6.1. A comparison of relevant operating conditions of the HFR, ITER and the Demonstration power plant (DEMO) is presented in table 6.2. Although the damage values are similar for all reactors, the transmutation of He is much lower at HFR than at ITER and DEMO. Section 6.2. addresses microscopy work done on the irradiated samples and identifies the irradiation induced defects. Material irradiated in the same conditions was mechanically tested and the results can be found in references [4–7]. Section 6.3. establishes the relation between the irradiation induced defects and the observed mechanical properties. Furthermore, also in this section a discussion is presented regarding the parameter α used in the irradiation hardening equation that reflects the strength of the induced defects in stopping the dislocation movement during a tensile test. Finally, section 6.4. discusses the expected transmutation of He in Eurofer and presents thermal desorption spectroscopy (TDS) results obtained with irradiated steel.

Table 6.1 *Irradiation conditions discussed in this chapter. Irradiation doses in dpa and irradiation temperature.*

Irradiation dose (dpa)	Irradiation temperature (K)	Duration (full power days)
2.4	333	150
1.9	573	250
8.0	573	720

Table 6.2 *Material relevant conditions at HFR [8], ITER and DEMO [9–11].*

	HFR	ITER	DEMO
Fusion Power (GW)	—	0.5	2 – 2.5
Heat Flux (MW/m^2)	1	0.1 – 0.3	0.5
Neutron Flux (m^{-2}s^{-1})	10^{18}	10^{18}	10^{19}
Damage, displacements per atom (dpa)	1.9 – 8.0 [1]	3 – 10	50 – 80
Transmutation product rates at first wall	~ 10 – 44 appm He [1]	~ 30 - 100 appm He ~ 135 - 450 appm H	~ 500 - 800 appm He ~ 2250 - 3600 appm H

[1] values for the work discussed in this thesis.

6.2 Transmission electron microscopy

To identify and understand the irradiation induced defects observed in Eurofer97, it is important to understand the unirradiated microstructure of this steel. The unirradiated Eurofer97 TEM images shown in this section were obtained by M. Kolluri and are published in reference [12]. The TEM work on neutron irradiated material refers to three irradiation conditions: 2.4 dpa and a temperature of 333 K, 1.9 dpa and a temperature of 573 K, and 8.0 dpa and a temperature of 573 K.

Two types of irradiation induced defects are identified in this section: black dots and dislocation loops. Black dots are identified as an agglomeration of point defects or fine precipitates [13]. With the goal of correlating the defect sizes and densities with the experimentally measured mechanical properties, the TEM micrographs were analyzed with the help of an imaging program. The distinction between black dots and dislocation loops was based on observation of a central whole for the latter. The presence of a central hole at the time of the TEM micrograph is dependent on the orientation of the loops in regard to the electron beam of the microscope (i.e. loops that are not perpendicular to the beam will show a smaller diameter or will not show a central hole). If the central hole is not observed for what in fact is are small dislocation loops, these will be identified as black dots. The calculated defect densities were obtained assuming a sample thickness of 15 nm (chapter 3). Further details regarding the irradiation experiments and thinning of the samples can be found in the experimental section of this thesis, in chapter 3.

6.2.1 Microstructure of unirradiated Eurofer97

Unirradiated Eurofer97 was investigated with TEM [12]. Figure 6.1A shows an overview of the unirradiated sample where laths of tempered martensite are identified [12,14]. Specifications of the manufacturer mention a lath size in the range 9 – 23 μm for Eurofer97 [12]. The martensite tempering done at the manufacturer (1033 K for 90 min) produces several carbides, seen in figures 6.1A and 6.1B along the grain boundaries and inside the martensite grains. Two types of precipitates are observed. The first type of precipitates is located at the lath boundaries (figure 6.1B) and has a coarse spheroidal shape, with sizes in the range 50 – 200 nm. The composition of these precipitates was not studied for this work but they can be recognized as $M_{23}C_6$ type precipitates [14–16]. The second type of precipitates, smaller in size, have a globular shape (figure 6.1B) and are located inside the grains. These precipates show a size in the range 10 – 100 nm and are identified according to the literature as MX type phases (where M is a Iron, Chromium or Tungsten and X is Tantalum or Vanadium) [14,15].

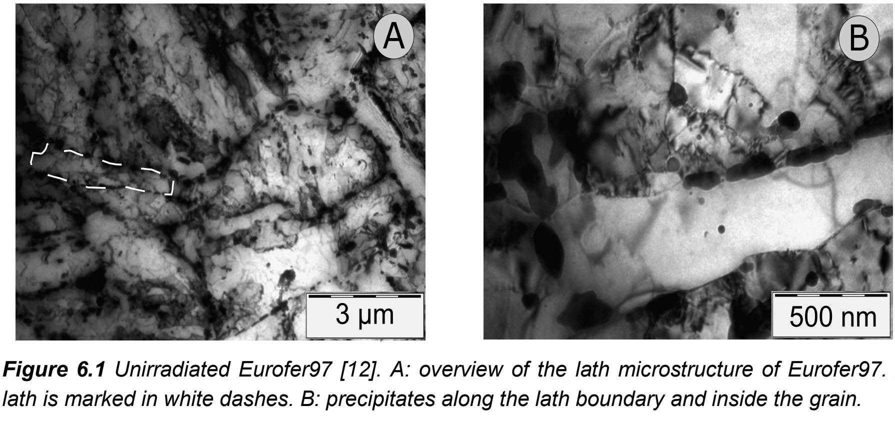

***Figure 6.1** Unirradiated Eurofer97 [12]. A: overview of the lath microstructure of Eurofer97. A lath is marked in white dashes. B: precipitates along the lath boundary and inside the grain.*

6.2.2 Microstructure of Eurofer97 neutron irradiated to 2.4 dpa and 333 K

Eurofer97 was neutron irradiated to 2.4 dpa at 333 K. The overview of the microstructure observed is shown in figures 6.2A and 6.2B. During the thinning of the TEM discs part of the TEM sample was damaged with corrosion. The damaged area is marked in figure 6.2A and does not affect the analysis of the irradiation induced defects. The observed microstructure is similar to that of unirradiated Eurofer, with precipitates expected to be of $M_{23}C_6$ and MX type [14,15] (figure 6.2B) and pre-existing martensitic laths are unchanged by neutron irradiation (figure 6.2A).

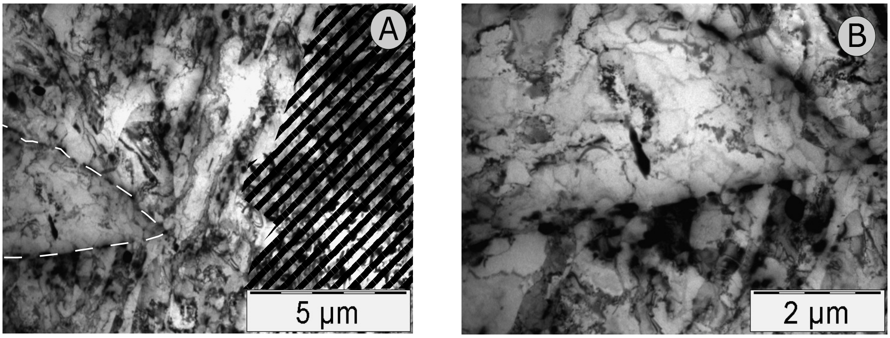

Figure 6.2 *Microstructure of 2.4 dpa and 333 K neutron irradiated Eurofer97. A: overview of the microstructure. The area damaged during thinning is marked with black stripes. A lath grain is traced with white dashes. B: detail of the lath marked in figure A. Larger precipitates are found in the grain boundaries while smaller ones are spread inside the grains. Irradiation induced damage is present as small black dots that are observed inside the grains.*

TEM micrographs showing the details of 2.4 dpa, 333 K irradiated laths are shown in figures 6.3A and 6.3B. These micrographs allow the identification of evenly spread irradiation damage, present as black dots (agglomeration of point defects or fine precipitates [13]). The black dots observed may act as pinning points for dislocation lines, as shown in figure 6.3B, and contribute for irradiation hardening. From the observation of an area of 1.12×10^{-12} m^2, a defect density of 1.9×10^{14} m^{-2} is calculated and an average defect size of 7 nm with a distribution width of 2 nm is measured. The size distribution of the black dots' diameters is shown in figure 6.4.

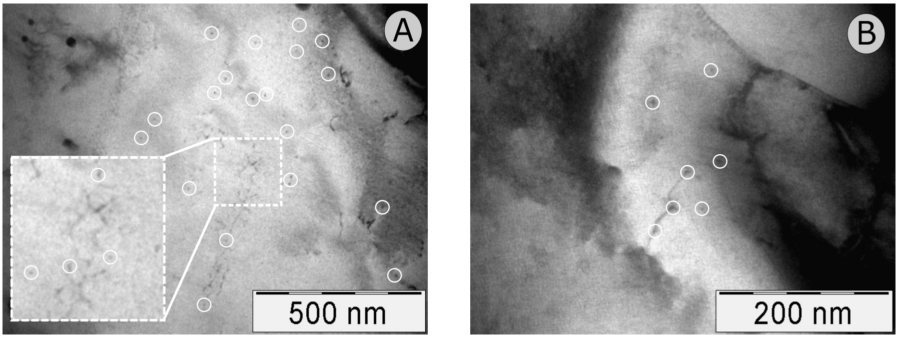

Figure 6.3 *Microstructure of 2.4 dpa and 333 K neutron irradiated Eurofer97. The images are taken inside a lath. The irradiation induced damage is observed as black dots, circled in white. A: an area consisting of several black dots is zoomed in. B: a dislocation line pinned on black dots is observed.*

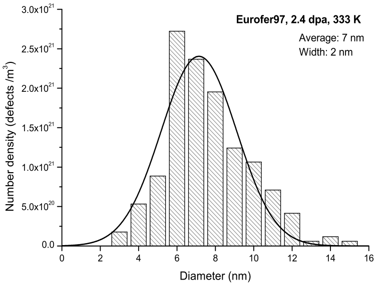

Figure 6.4 *Size distribution of irradiation induced black dots in Eurofer97, 2.4 dpa, 333 K. Results obtained after analysis of an area of 1.12 x 10^{-12} m^2. The average size of the black dots is 7 nm.*

6.2.3 Microstructure of Eurofer97 neutron irradiated to 1.9 dpa and 573 K

TEM observations were conducted on Eurofer97 steel that was neutron irradiated to 1.9 dpa at 573 K. The damage observed under these irradiation conditions represents the evolution of defects with increasing temperature (with respect to 2.4 dpa, 333 K). A low-magnification overview of the microstructure after irradiation is shown in figures 6.5A and 6.5B, where the pre-existing martensitic laths (not changed with irradiation) can still be observed. The precipitates, located inside and on the laths boundaries, are expected to be $M_{23}C_6$ and MX type phases [14,15].

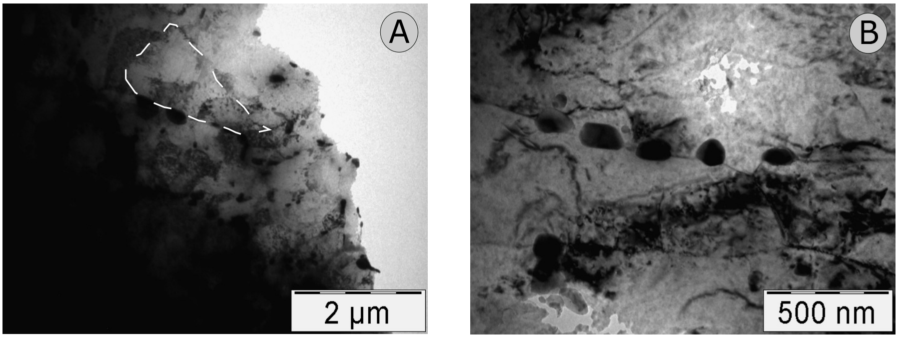

Figure 6.5 *Microstructure of 1.9 dpa and 573 K neutron irradiated Eurofer97. Irradiation induced damage present as small black dots and dislocation loops is observed inside the grains. A: overview of the microstructure. A lath is marked in white dashes. B: Larger precipitates are located on the grain boundaries, while smaller ones are spread inside the grains.*

The micrographs shown in figures 6.6A and 6.6B reveal the presence of irradiation induced defects. These irradiation conditions lead to the formation of black dots and dislocation loops. In comparison to the irradiation of 2.4 dpa and 333 K (section 6.2.2.), where only black dots were observed, the micrographs indicate that the increase in irradiation temperature to 573 K leads to the development of black dots into dislocation loops, as a consequence of the thermally activated diffusion and aggregation of point defects.

From the analysis of an area of 8.8 x 10^{-13} m^2 histograms of the defects size were plotted and are shown in figures 6.7A and 6.7B. The histograms show that the size distributions of black dots and dislocation loops have a bi-modal distribution each and their defects size overlaps. The black dots have average sizes of 9 nm and 17 nm, (figure 6.7A). The dislocation loops have average sizes of 10 nm and 18 nm (figure 6.7A). For both types of defects, the distribution width of the peaks is of 1 nm. As discussed at the beginning of section 6.2, the classification of black dots and dislocation loops is dependent on the observation of a central whole for the latter, taking place when the dislocation loops are perpendicular to the electron beam of the microscope. The overlapping of sizes can be interpreted as an indicator that part of what seems to be black dots, are in fact dislocation loops. If these dislocation loops would be observed in a direction perpendicular to the electron beam, the central hole of the loop would be noticed. Considering that a definite distinction between black dots and loops cannot clearly be made, the density of irradiation induced defects in this sample, independently of their character, was calculated to be 1.8 x 10^{14} m^{-2} (figure 6.7C). The histogram of the defects size is shown in figure 6.7C. The size distribution shows a bi-modal peak distribution for all observed defects, with one peak at around 9 nm and another peak around 17 nm, both with a distribution width of 1 nm. It is noticed that the defect density (independently of the defect character) is approximately the same for this sample in comparison to the one irradiated to 2.4 dpa, 333K, while the overall defect size increases for the irradiation condition of 1.9 dpa and 573 K.

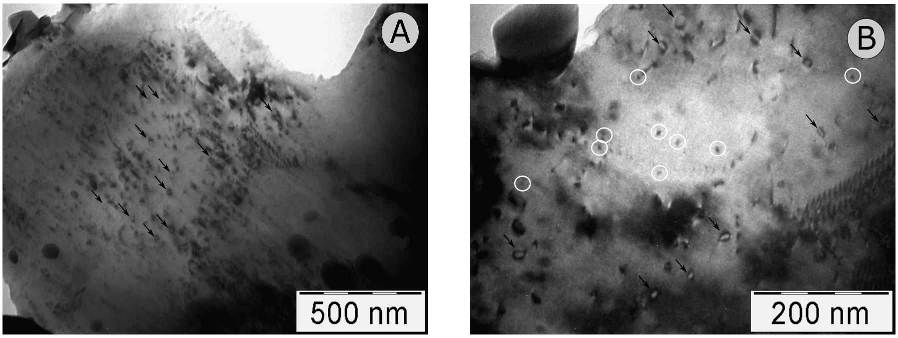

Figure 6.6 *Details of the microstructure of 1.9 dpa and 573 K neutron irradiated Eurofer97. Images A and B are taken inside a lath. The irradiation induced damage is observed as black dots and dislocation loops. The black dots are circled in white and the dislocation lines are pointed with a back arrow.*

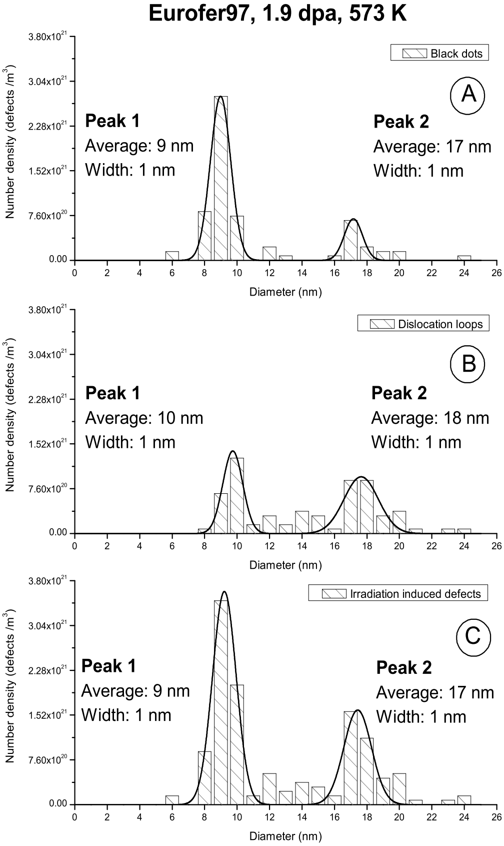

Figure 6.7 *Size distribution of irradiation induced defects in Eurofer97, 1.9 dpa, 573 K. Bi-modal size distribution is observed. A – black dots, average sizes of peak 1 and peak 2 are 9 nm and 17 nm, respectively; B – dislocation loops average sizes of peak 1 and peak 2 are 10 nm and 18 nm, respectively; C – all defects observed, average sizes of peak 1 and peak 2 are 9 nm and 17 nm, respectively.*

6.2.4 Microstructure of Eurofer97 neutron irradiated at 8.0 dpa and 573 K

Figure 6.8 shows a low magnification TEM image of Eurofer97 that was neutron irradiated at 8.0 dpa and 573 K. In the figure 6.8A the pre-existing martensitic lath structure is observed, with precipitates around the grain boundaries and inside the grains. Radiation damage is found uniformly distributed throughout the material and can be observed in figure 6.8B.

A detailed observation of a damaged grain is shown in figure 6.9. Two types of radiation damage are distinguishable, black dots and dislocation loops. The size distribution of these defects is presented in figure 6.10 for an analyzed area of 1.9 x 10^{-13} m^2. The black dots have an average size of 4 nm with a distribution width of 1 nm (figure 6.10A), and the dislocation loops of 5 nm with a distribution width of 2 nm (figure 6.10B). The average size of irradiation induced defects for this sample is 4 nm with a distribution width of 1 nm, and the defect density is 7.0 x 10^{14} m^{-2} (figure 6.10C).

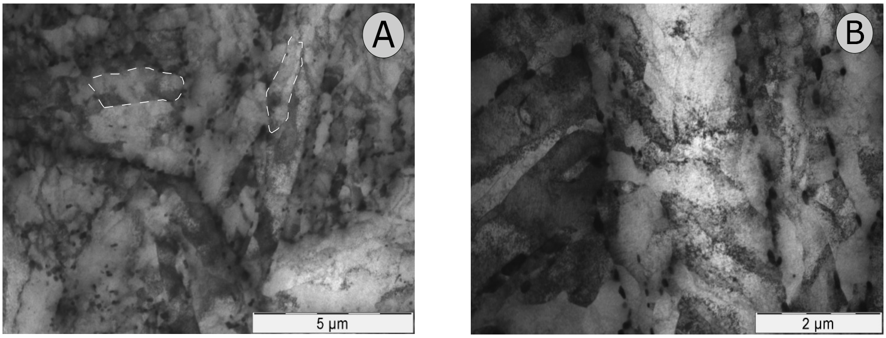

Figure 6.8 *Overview of the microstructure of 8.0 dpa, 573 K neutron irradiated Eurofer97 irradiated at HFR. Radiation damage is spread throughout the sample. A: overview of the irradiated microstructure. Laths are marked in white dashes. B: Detail of the inside of a lath. Radiation damage is observed throughout the grain.*

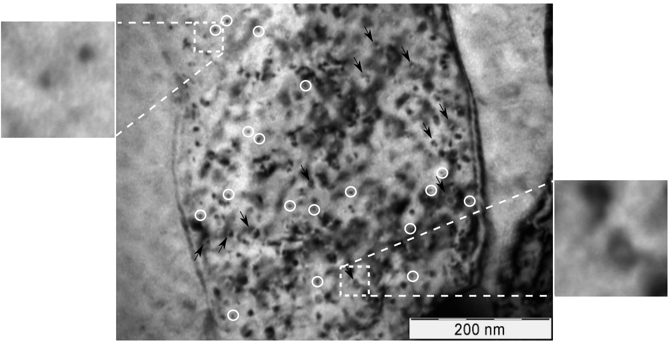

Figure 6.9 *A: Detail of the microstructure of 8.0 dpa, 573 K neutron irradiated Eurofer97*

showing the irradiation induced defects. The irradiation induced damage is observed as black dots and dislocation loops. The black dots are circled in white and the dislocation lines are pointed with a back arrow.

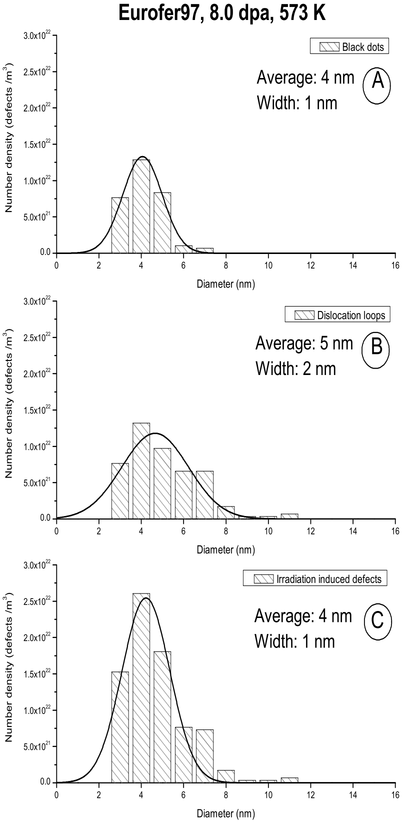

Figure 6.10 *Size distribution of irradiation induced defects in Eurofer97, 8.0 dpa, 573 K. A – black dots, average size of 4 nm; B – dislocation loops, average size of 5 nm; C – all defects observed, average size of 4 nm.*

6.2.5 Discussion of TEM observations

Table 6.3 summarizes the TEM observations discussed in section 6.2. In this table, as well as for the work related to irradiation hardening shown in section 6.3, the character of the radiation damage is not distinguished, i.e. black dots and dislocation loops are defects, independently of their character. The decision to not distinguish the two types of defects was taken to compensate possible misidentifications of dislocation loops as black dots.

The histogram of the defects size observed for the irradiation at 1.9 dpa and 573 K shows a bi-modal distribution (figure 6.7). The bi-modal distribution is observed in the histogram obtained for black dots, for dislocation loops and, consequently, for the overall defects observed. In the case of the black dots (figure 6.7A), the presence of the second peak size can be attributed to the misidentification of the dislocation loops as black dots due to their orientation in regard to the electron beam. Furthermore, a TEM analysis with higher magnification would help sorting black dots from loops - perhaps the magnification chosen for the micrographs analyzed is not enough to clearly identify the central hole of the dislocation loops. The mechanism behind the bi-modal distribution of the histogram regarding the dislocation loops (figure 6.7B) is not known at the moment.

The defect sizes measured for the first two irradiation conditions (2.4 dpa, 333 K and 1.9 dpa, 573 K) point to the conclusion that the defect size increases with increasing temperature. From the first to the second irradiation conditions, the dpa level is reduced and the irradiation temperature increased. Even so, the TEM observed defects for the irradiation at 2.4 dpa and 333 K are smaller than those of the irradiation at 1.9 dpa and 573 K. The increase of defect size is explained by the coalescence of defects and by the aggregation of newly formed Frenkel pairs to existing defects, both phenomena being promoted by the higher irradiation temperature. This observation is in agreement with the work of other authors [18,19].

The second and third irradiation conditions clearly show that there is a decrease of size and increase of density of defects with increasing dose, for the same irradiation temperature. A higher dose is proportional to a higher number of Frenkel pairs formed in the matrix. The diffusion of Frenkel pairs is promoted by the high irradiation temperature. Although black dots and dislocation loops are formed, these can decrease their size and/or annihilate due to the diffusion of vacancies and interstitials. For a higher irradiation dose, this effect is stronger. Similar observations have been done by other authors [19,20], that report a completion between the formation of new loops and the annihilation of existing loops.

Table 6.3 *Summary of TEM observations. The irradiation induced defects are quantified independently of their character (no distinction is made between black dots and dislocation loops). The TEM sample thickness is assumed to be 15 nm (chapter 3).*

		2.4 dpa, 333 K	**1.9 dpa, 573 K**	**8.0 dpa, 573 K**
Area analyzed (m^2)		1.1 x 10^{-12} ± 1 x 10^{-13}	8.8 x 10^{-13} ± 9 x 10^{-13}	1.9 x 10^{-13} ± 2 x 10^{-13}
Number of analyzed defects[1]		209	163	135
Projected defect density, ρ (m^{-2}) [1]		1.9 x 10^{14} ± 2 x 10^{13}	1.8 x 10^{14} ± 2 x 10^{13}	7.0 x 10^{14} ± 7 x 10^{13}
Volume defect density, N (m^{-3}) [1]		1.2 x 10^{22} ± 1 x 10^{21}	1.2 x 10^{22} ± 1 x 10^{21}	4.7 x 10^{22} ± 5 x 10^{21}
Defect size, *d* (nm)	**Black dots**	7 ± 2 [2]	9 ± 1 [2] 17 ± 1 [2]	4 ± 1 [2]
	Dislocation loops	—	10 ± 1 [2] 18 ± 1 [2]	5 ± 2 [2]
	Overall	7 ± 2 [2]	9 ± 1 [2] 17 ± 1 [2]	4 ± 1 [2]

[1] – value obtained independently of the defect character (no distinction is made between black dots and dislocation loops).
[2] – width of the distribution.

6.3 Irradiation hardening

Irradiation hardening is a consequence of the creation of defect structures when a material is neutron irradiated. In this section the correlation between the TEM observations discussed in section 6.2. and previously reported tensile measurements [4,5,7] is established. The tensile measurements were done on specimens irradiated with similar conditions to those of the discussed TEM samples. The interpretation of the tensile measurements is based solely on the presence of black dots and dislocation loops as irradiation induced defects.

As the material is put under stress, dislocations glide through the matrix. When the dislocations find pinning obstacles, their further gliding is prevented. The strength of the obstacles in stopping the dislocation gliding (how effectively the dislocations are stopped) is inversely proportional to the distance between obstacles. The irradiation hardening ($\Delta\sigma_y$)after neutron irradiation (see chapter 2 for more information on this equation) is given by

$$\Delta\sigma_y = {}^{\alpha M\mu b}\!/_{l} \qquad (6.1)$$

where α is the obstacle strength, M is the Taylor factor (3.06 for bcc steels [21]), μ is the shear modulus (82 GPa), b is the length of the Burgers vector (2.5 x 10^{-10} m) and l is the inter-obstacle spacing [22]. The parameter α is an aspect of discussion [22], as it depends on the nature of the obstacle. While some authors defend that it is a mere fitting factor with a defined value depending on the obstacle type, other argue that it reflects the effectiveness of the obstacle in stopping a dislocation in motion. Following the latter idea, it is considered [22,23] that perfect barriers will have the maximum α value of 1. The irradiation hardening effect is calculated considering the average inter-obstacle spacing.

The questions of interest for section 6.3. are:

- Can the observed defect density explain the hardening values? Or are other defects present, such as helium bubbles that could not be observed with TEM?

- What is the correct equation to calculate the inter-obstacle spacing l, present in the hardening equation, from the defect density *N* and the obstacle diameter *d*: $l = {}^{1}\!/_{\sqrt{Nd}}$ or $l = {}^{1}\!/_{\sqrt[3]{N}}$? (chapter 2, section 2.4.)

- What is the value of the parameter α (obstacle strength) of the irradiation induced obstacles observed in the TEM study?

6.3.1 Tensile tests

Figure 6.11 shows the tensile curves corresponding to the three nominal irradiation conditions – 2.5 dpa and 333 K (figure 6.11A), 2.0 dpa and 573 K (figure 6.11B) and 8.0 dpa and 573 K (figure 6.11C) – measured at 300 K and at the irradiation temperature [4,5,7]. In the irradiation campaigns lead by NRG, multiple tensile specimens were irradiated [4,5,7]. It is expected that, due to the neutron flux profile in the HFR, the tensile specimens are not always irradiated to the exact same target dose. The differences between nominal and achieved dose are accounted for during the preparation of the irradiation program so that all samples irradiated with the same nominal dose are comparable (see chapter 3 for more information on achieved and nominal dose). The specimens used for the tensile tests shown in this section have the same nominal dose as the TEM samples discussed in section 6.2. The strain rate used was 5 x 10^{-4} s^{-1}. The tensile curves are plotted starting at the onset of the plastic region. This onset was based on the yield strength (YS) offset value for 0.2 % elongation. The elastic region of the curves is not shown as it was affected by the compliance of the tensile testing machine used for the measurements and it is not relevant for this analysis. The tensile results of unirradiated Eurofer97 are shown for comparison. Table 6.4 shows the tensile properties for unirradiated and irradiated steel. In table 6.4 the YS, ultimate tensile strength (UTS) and elongation values representative of the achieved dose of the TEM samples are based solely on one measurement. Because of that the standard error of the unirradiated condition was used.

The reference curve of Eurofer97 shows a long plastic region before necking (blue line represented in figures 6.11A,B,C for comparison). The uniform elongation of the irradiated materials is practically zero and the total elongation has significantly decreased. The irradiation induced defects observed with TEM – black dots and dislocation loops - are envisaged to be responsible for the increase in YS and UTS after irradiation in both test temperature conditions (table 6.4). In the tensile tests performed at 300 K the black dots, dislocation loops and precipitates act as obstacles for dislocation movement. In the tests done at the irradiation temperature, the YS is lower because of thermally activated dislocation gliding that is promoted by the increased temperature (table 6.4). Annihilation of defects is unlikely to be related to the lower YS and UTS of this test curve as the test temperature did not surpass the irradiation temperature and the time at elevated temperature was very limited. The standard errors of the reference unirradiated condition were calculated based on a set of Eurofer97 tested samples. Further information on these samples can be found in reference [4]. Because the YS, UTS and elongation values of the irradiated samples are based solely on one measurement, the standard errors of the unirradiated condition were used in these cases.

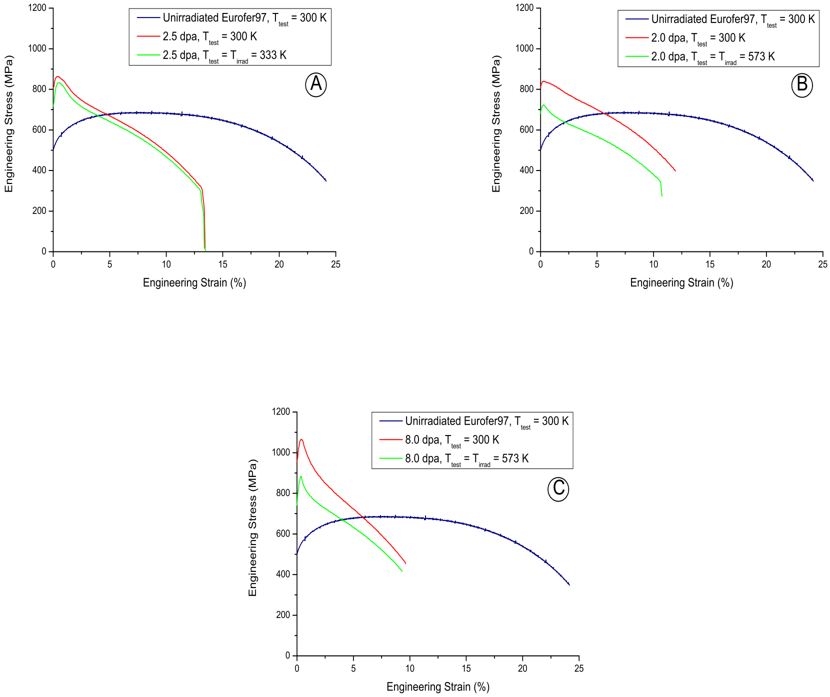

Figure 6.11 *Tensile tests of irradiated Eurofer97. A – nominal dose of 2.5 dpa, 333 K; B – nominal dose of 2.0 dpa, 573 K; C – nominal dose of 8.0 dpa, 573 K. The blue lines correspond to the unirradiated conditions, the red lines to the tests done at 300 K and the green lines to the tests done at the irradiation temperature.*

Table 6.4 *Tensile properties of irradiated Eurofer97. Irradiation conditions of tensile specimens and of TEM samples. Tensile tests have been done at 300 K (T_{test}) and at the irradiation temperature (T_{irrad}).*

		Unirradiated Eurofer97	**Neutron irradiated Eurofer97**					
		T_{test} = 300 K	T_{test} = 300 K	T_{test} = T_{irrad}	T_{test} = 300 K	T_{test} = T_{irrad}	T_{test} = 300 K	T_{test} = T_{irrad}
Tensile specimens	**Nominal dose (dpa)**	—	**2.5**		**2.0**		**8.0**	
	Irradiation temperature (K)	—	**333**		**573**		**573**	
	YS0.2% (MPa)	541 ± 13[1]	859 ± 13[2]	831 ± 13[2]	839 ± 13[1]	720 ± 13[1]	1047 ± 13[1]	883 ± 13[1]
	UTS (MPa)	664 ± 15[1]	863 ± 13[2]	832 ± 15[2]	840 ± 15[1]	723 ± 15[1]	1047 ± 15[1]	883 ± 15[1]
	Total elongation (%)	23.9 ± 1.6[1]	14.8 ± 1.6[2]	14.8 ± 1.6[2]	13.3 ± 1.6[2]	12.2 ± 1.6[2]	11.5 ± 1.6[2]	10.8 ± 1.6[2]
	Uniform elongation (%)	5.8 ± 0.8[1]	0.3 ± 0.8[2]	0.2 ± 0.8[2]	0.3 ± 0.8[2]	0.2 ± 0.8[2]	0.1 ± 0.8[2]	0.1 ± 0.8[2]
TEM samples	**Achieved dose (dpa)**	—	**2.4**		**2.0**		**8.0**	
	Irradiation temperature (K)	—	**333**		**573**		**573**	

[1] **–** value of the standard error of a set of unirradiated Eurofer97 specimens.

[2] – value of the standard error for the unirradiated condition.

6.3.2 Irradiation hardening vs. TEM observations

Within the several Eurofer97 tensile specimens that were irradiated at HFR, some have reached very similar doses (achieved doses) to those of the TEM samples discussed in section 6.2. To improve the statistics on the YS and UTS values, specimens with the same nominal dose of the TEM samples are considered in this section. This section distinguishes and discusses two situations: the tensile specimens with a similar achieved dose to that of the TEM samples, and the tensile specimens with the same nominal dose as the TEM samples (see chapter 3 for more information on achieved and nominal doses). The YS values measured at 300 K for unirradiated and irradiated samples are presented in table 6.5. The YS values for the unirradiated condition and for irradiations at the nominal doses of the TEM samples were obtained from a series of tests. The scattering of the YS leads to the standard errors presented. Because the YS representative of the achieved dose of the TEM samples are based solely on one measurement, the standard error of the unirradiated condition was used in these cases.

Table 6.5 *Yield strength and increase of yield strength measured for Eurofer97 specimens at* T_{test} *= 300 K.*

TEM sample conditions	**Tensile specimens conditions**	**YS (MPa)**	**ΔYS (MPa)**
Unirradiated	Unirradiated	541 ± 13[2]	—
2.4 dpa, 333 K	achieved dose 2.4 dpa, 333 K[1]	859 ± 13[2]	320 ± 20
	nominal dose 2.5 dpa, 333 K	848 ± 15	310 ± 20
1.9 dpa, 573 K	achieved dose 2.0 dpa, 573 K[1]	839 ± 13[2]	300 ± 20
	nominal dose 2.0 dpa, 573 K	880 ± 30	340 ± 40
8.0 dpa, 573 K	achieved dose 7.5 dpa, 573 K[1]	1047 ± 13[2]	510 ± 20
	nominal dose 8.0 dpa, 573 K	1040 ± 30	500 ± 40

[1] – tensile specimens with an achieved dose similar to that of the TEM samples discussed in section 6.2.

[2] – value of the standard error for the unirradiated condition.

The increase in YS as a function of dose for irradiations at 333 K and 573 K is plotted in figures 6.12 and 6.13, respectively, and originally presented in [4]. In both graphs a line fitted to trace the trend of the data measured is plotted [4].

Figure 6.12 shows that the increase of YS due to irradiation at 333 K reaches a saturation at doses of ~ 0.3 dpa up until the tested dose of 2.5 dpa. The irradiation damage achieved at ~ 0.3 dpa reflects an increase in YS of ~ 325 MPa. The TEM micrographs shown in figure 6.3, obtained from a sample irradiated at 2.4 dpa and 333 K, support the conclusion that the hardening observed is related to the presence of black dots. When a material is neutron irradiated, a sequence of events takes place: collision, thermal spike, quenching and annealing [22]. The first event is the collision of neutrons with the atoms in the matrix and the creation of displacements (Frenkel pairs). Although Frenkel pairs are created, by the end of this stage stable defects (the defects present in the microstructure by the end of the irradiation) did not have time to form. The displaced atoms share their energy with the surrounding atoms (thermal spike), and the structural arrangement of the lattice in this region is lost [22]. At this point the arrangement of atoms resemble a molten material. As the energy is dissipated, the local temperature quickly decreases (quenching) and the structure of the material is recovered, although containing stable lattice defects. The number of stable defects created is lower than the amount of displaced atoms in the neutron collision [22]. Finally, the annealing stage is defined by the escape of defects from the cascade region. Although the stages above mention describe the sequence of events expected during one neutron irradiation, in real conditions multiple irradiations (from multiple neutrons) will take place in parallel and sequentially [22]. A possible explanation for the hardening plateau observed for irradiations above ~ 0.3 dpa is that this damage level is the starting point at which the thermal spike is not enough to allow recovery of the material, leading to a saturation of defects in the lattice and to the observation of a plateau in figure 6.12.

The yield stress measured for specimens irradiated at 573 K (figure 6.13) shows an increase of YS at a lower rate than for irradiations at 333 K. The fact that no hardening saturation is observed up to ~ 10 dpa is explained by the increased irradiation temperature that promotes thermally activated recombination of defects and allows partial recovery of the material.

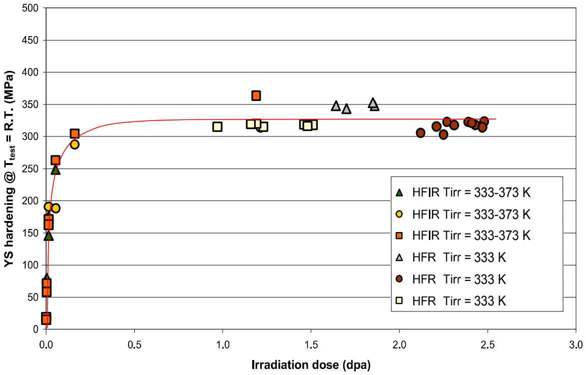

Figure 6.12 *Increase in YS of samples with T_{irrad} = 333 K, measured at room temperature and as a function of dose [4]. The samples discussed in this work that are irradiated with 2.4 dpa, 333 K are here represented by red circles. HFIR refers to the High Flux Isotope Reactor, located in the United States. The solid line represents the trend observed by the data points.*

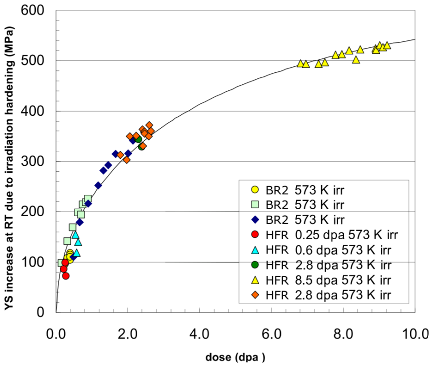

Figure 6.13 *Increase in YS of samples with Tirrad = 573 K, measured at room temperature and as a function of dose [4]. The 1.9 dpa, 573 K sample is related to the orange lozenges. The 8.0 dpa, 573 K sample is related to the yellow triangles. BR2 refers to the Belgium Reactor 2. The solid line represents the trend observed by the data points.*

The tensile tests shown in figures 6.12 and 6.13 clearly show that the irradiation temperature strongly affects the hardening rate. As discussed for the TEM observations (section 6.2), the irradiation induced defects observed can be either black dots or dislocation loops. If all black dots evolve into dislocation loops, it can be considered that all irradiation conditions induce defects of the same type. The TEM study presented in section 6.2. allowed the identification of defect types, densities and sizes. But can the experimentally measured increase of hardening be explained purely by the presence of the TEM observed defects? Or are small voids or He bubbles that were not clearly observed in the micrographs contributing to the irradiation hardening?

Three parameters are of interest when analyzing defects: the size, the density and the obstacle strength value. As discussed before (and shown in table 6.3), the average size of the defects increases for higher irradiation temperature and a similar irradiation dose (2.4 dpa, 333 K vs. 1.9 dpa, 573 K) and decreases with an increasing dose and the same irradiation temperature (1.9 dpa, 573 K vs. 8.0 dpa, 573 K). As for the defect densities, the samples irradiated at 2.4 dpa, 333 K and 1.9 dpa, 573 K have a similar defect density, which increases when irradiating at 8.0 dpa, 573 K. But do the irradiation induced defects have a constant obstacle strength for all irradiation conditions? If so, what is that value? If not, how does the obstacle's size affect *α*? These questions led to a study to correlate the obstacle size and density (table 6.3) to the experimentally obtained irradiation hardening (table 6.4). As discussed in chapter 2, section 2.4, the inter-obstacle spacing (l) can be calculated based on the dispersed barrier hardening (DBH) model, given by

$$l = {}^{1}\!/_{\sqrt{Nd}} \qquad (6.2)$$

or based on the effective inter-particle spacing, given by

$$l = {}^{1}\!/_{\sqrt[3]{N}} \qquad (6.3)$$

The validity of equation 6.3 is based on the fact that the inter-obstacle length is much larger than the defect diameter ($l \gg d$). For both equations *N* is the obstacle density in units of m^{-3} and *d* is the obstacle diameter in units of m.

To explain the results of the correlation between obstacle size and density and irradiation hardening, the following assumptions must be considered:

1. The *α* parameter is dependent of the nature of the defect.

2. α is independent of the size of the obstacle
3. If a perfectly hard barrier has an α value of 1 [22,23], the same parameter of weaker obstacles should be smaller than 1.
4. The obstacle diameter used in calculations is represented by the average diameter of all defects observed in the TEM micrographs.
5. The inter-obstacle spacing used for the following calculations reflects the average distance between irradiation induced defects.

In order to determine the obstacle strength value of the defects observed with TEM, the irradiation hardening according to equation 6.1 was plotted, figure 6.14, with the calculated values of $\Delta\sigma_y$ for α values in the range 0.10 – 0.65. The inter-obstacle length parameter, l, was calculated using equations 6.2 (red lines and symbols) and 6.3 (blue lines and symbols). The defect densities and sizes values used were the ones obtained from the TEM observations (table 6.3). Although a bi-modal size distribution was observed for the sample irradiated with 1.9 dpa, 573 K, the average size of all defects (the first peak located at 9 nm, the second peak located at 17 nm, average of 13 nm) was considered for these calculations. The outcome of equation 6.1 is compared with the experimentally obtained values of $\Delta\sigma_y$ (table 6.4). The orange lines represent the increase in YS measured for samples with the same irradiation conditions as those for the samples observed with TEM. The green lines represent the increase in YS measured for samples with the same nominal irradiation dose and irradiation temperature as that of the TEM samples. The highlighted areas (in orange and green) around the horizontal line representing the measured $\Delta\sigma_y$ represent the error of the tensile measurement.

By comparing the experimentally measured $\Delta\sigma_y$ and its fitted α values, conclusions can be drawn about the validity of the two methods to calculate l. Let us start by analyzing the outcome of equation 6.1 when using equation 6.2 for calculating the inter-obstacle spacing. The irradiation conditions of 2.4 dpa and 333 K yield an average α value of 0.34 (range 0.33 – 0.35, figure 6.14A). The higher implantation temperature of 573 K and the nominal irradiation dose of 1.9 dpa yield an average α value of 0.43 (range 0.38 – 0.48, figure 6.14B). Finally, the irradiation conditions of 8.0 dpa and 573 K yield an average *α* value of 0.53 (range 0.50 – 0.56, figure 6.14C).

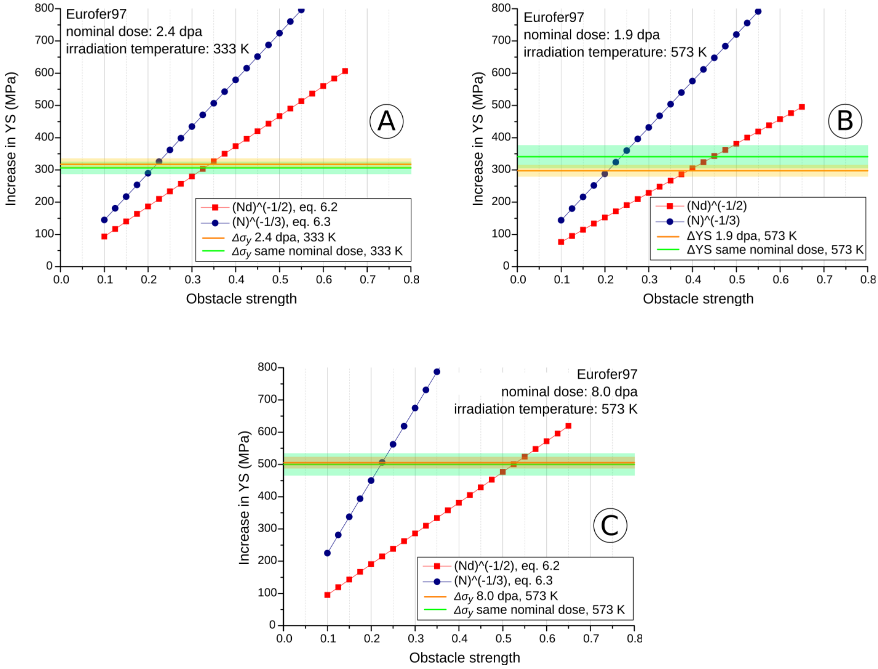

Figure 6.14 *Calculated increase of YS after neutron irradiation vs. obstacle strength according to equations 6.1, 6.2 and 6.3. A: nominal dose of 2.5 dpa, 333 K. B: nominal dose of 2.0 dpa, 573 K. C: nominal dose of 8.0 dpa, 573 K. Two methods to calculate the inter-obstacle spacing are plotted:* $\boldsymbol{l} = \mathbf{1}/\sqrt{\boldsymbol{Nd}}$ *(equation 6.2., red squares) and* $\boldsymbol{l} = \mathbf{1}/\sqrt[3]{\boldsymbol{N}}$ *(equation 6.3, blue circles). The experimental YS is plotted for the specimens with the same achieved dose as the TEM samples (orange lines) and for specimens with the same nominal dose (green lines). The horizontal colored regions refer to the standard deviation of the measured YS values.*

The substitution of equation 6.3 in equation 6.1 shows that the irradiation conditions of 2.4 dpa and 333 K yield an average *α* value of 0.21 (range 0.20 – 0.23, figure 6.14A). The irradiation conditions of 1.9 dpa and 8.0 dpa, both at the irradiation temperature of 573 K, yield the same average *α* value of 0.23 (range 0.20 – 0.25 for figure 6.14B, while figure 6.14C shows only the point of 0.23 in the highlighted region).

By comparing the outcome of equations 6.2 and 6.3, it is noticed that the latter will lead to a fairly constant α parameter throughout the different irradiation conditions, with an average value of 0.22. The value 0.22 is agreement with the observations by other authors for the same parameter [23]. This result demonstrates that, if equation 6.3 is valid and for the irradiation conditions studied, the size of the obstacle to the dislocation motion (up to obstacle sizes of 13 nm) does not affect the obstacle strength.

But can the obstacle strength value of 0.22 be used to fit whole range of $\Delta\sigma_y$ (T_{test} = 300 K) expected between 2 and 10 dpa, for irradiations conducted at 573 K? Figure 6.16 shows the experimentally measured values of $\Delta\sigma_y$ obtained from irradiated Eurofer in the range 2 – 10 dpa, at 573 K. The lines represent the calculated $\Delta\sigma_y$ (equation 6.1) for three possible α values: 0.21, 0.22 and 0.23. The defect densities used in the calculations of $\Delta\sigma_y$ for the whole dpa range were obtained with

$$N_{dpa} = N_{1.9} + \frac{(N_{8.0} - N_{1.9})}{8.0 - 1.9} \cdot (\phi - 1.9) \qquad (6.4)$$

where N_{dpa} is the calculated defect density correspondent to a dose ϕ, and $N_{1.9}$ and $N_{8.0}$ are the known defect densities for the samples irradiated with 1.9 dpa and 8.0 dpa, both a 573 K (table 6.3). Using the least square method of fitting it is concluded that the optimal obstacle strength is 0.22 for the irradiations done at 573 K. The fitting in figure 6.15 shows that the equation 6.1, used to calculate the irradiation hardening, is very sensitive to the value α.

A similar procedure cannot be applied to the 333 K irradiation as the matrix reflects a saturation of irradiation induced defects at 1.9 dpa. The linear interpolation used to calculate defect densities for different dpa’s cannot be applied for irradiation doses above ~ 0.3 dpa and T_{irrad} of 333 K. At the moment there is no experimental data available of Eurofer97 tensile specimens irradiated at 333 K and doses below ~ 0.3 dpa, and tested at 300 K.

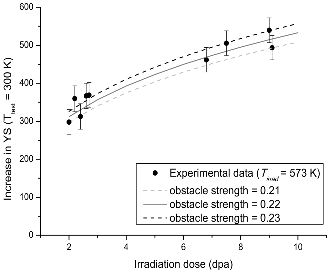

Figure 6.15 *Calculation of the irradiation hardening for three possible obstacle strength values: 0.21, 0.22 and 0.23. The experimental data refers to neutron irradiated Eurofer97 at a temperature 573 K. The tensile tests of the irradiated Eurofer97 were performed at a temperature of 300 K. The α value of 0.22 yields the optimal fit.*

6.4 Helium bubbles

When Eurofer97 steel is neutron irradiated, helium is expected to transmute in the matrix from Nickel and Boron. As no helium bubbles were observed in the micrographs obtained with TEM (section 6.2), the density of bubbles that could eventually form and be observed in a TEM sample was calculated based on the density of transmuted He for Eurofer97 for the discussed irradiation conditions. In this section, the first results on the TDS measurements on neutron irradiated Eurofer97 steel are discussed.

6.4.1 He bubbles TEM

Neutron irradiation will lead to the transmutation of helium in the matrix. Due to the low solubility of helium, bubbles are expected to form. Although other authors have identified helium bubbles or deduced their presence by the changes observed in the mechanical properties of irradiated Eurofer97 [24–31], this was not the case in this work. But should helium bubbles be expected in these irradiation conditions? If so, which density of bubbles should be expected considering the density of transmuted helium?

TEM discs have an average weight of 2.6 mg. Assuming that the solubility of He in Fe is zero and with the help of the ideal gas law, given by

$$PV = N_{He}^{bubble} RT_{irrad} \tag{6.5}$$

it is possible to calculate the number of He atoms present in a bubble in equilibrium in an iron matrix, assuming that the bubble would have a diameter smaller than 3 nm (the diameter of the bubbles should be smaller than the detection limit of the TEM). In equation 6.5 P is the pressure of the bubble, V is the volume of the bubble with the value of 1.4 x 10^{-26} m^3, N_{He}^{bubble} is the number of helium atoms present in a bubble, R is the gas constant with the value of 1.4 x 10^{-9} Pa, and T_{irrad} is the irradiation temperature at which the bubbles are formed. The pressure P is given by

$$P = \frac{2\gamma}{r} \tag{6.6}$$

where γ is surface tension with the value of 1.9 N/m, and r is the radius of the bubble with the value of 1.5 x 10^{-9} m. Table 6.6 shows the calculated number of He bubbles expected in the TEM samples, for the different irradiation conditions. The He concentrations for the different irradiation conditions were obtained from a comparison to those of ODS Eurofer [31]. It is assumed that all the transmuted He is trapped in the irradiated Eurofer sample.

Table 6.6 *Expected amount of He atoms per TEM sample and per formed bubble.*

	TEM samples		
Irradiation dose (dpa)	2.4	1.9	8.0
Irradiation temperature, T_{irrad} (K)	333	573	573
Fraction of He atoms per TEM sample (appm)	13.3	10.5	12.8
Number of He atoms in a bubble, N_{He}^{bubble} (atoms)	7.9 x 10^3	4.5 x 10^3	4.5 x 10^3
Number of He atoms in a bubble (atoms/cm^3)	1.1 x 0^{18}	8.9 x 10^{17}	1.1 x 10^{18}
Number of formed bubbles (bubbles/cm^3)	1.5 x 10^{14}	2.0 x 10^{14}	2.4 x 10^{14}
Number of bubbles possible to observe in an volume of 1.5 x 10^{-14} cm^2	2.2	3.0	3.6

The expected number of bubbles per TEM area of 1.5 x 10^{-14} cm^2 ranges from 2.2 to 3.6, depending on the irradiation conditions. But how realistic is it to expect that all the He will form bubbles? If the transmuted He is located at an interstitial position it will have a migration energy (E^m) of ~ 0.05 - 0.08 eV [32,33] and will not be present at room temperature. Furthermore, it is likely that with increasing irradiation temperature some of the helium-vacancy clusters that would develop into bubbles dissociate (as their dissociation energy is reached) before reaching equilibrium and do not grow further. Although no He bubbles were observed with TEM, the fact that a low density of bubbles is expected even for the highest irradiation dose indicates the low likelihood that the bubbles would be observed with microscopy - the low density of He bubbles makes them hard to find in a limited number of micrographs.

6.4.2 TDS on neutron irradiated Eurofer97

With the goal of comparing the TDS results obtained from He implanted Eurofer97 steel (chapter 5) with TDS measurements done in neutron irradiated Eurofer97, the TDS system was moved from TUDelft to NRG in April 2013. The parallel between the measurements would allow a direct conclusion on the effectiveness of implantations to reproduce the damage created during irradiations. The move was followed by a long period of safety improvements and adaptation of the system to measure neutron irradiated samples. By May 2015 the first measurements of He desorption in neutron irradiated Eurofer97 were performed at NRG. Although there is not yet a clear interpretation of the desorption spectra, these measurements are a milestone for the fusion community as they show the actual He trapping of Eurofer97 in a neutron environment and can help bridging the gaps when it comes to comparing experimental work done with He implanted and neutron irradiated materials.

During the neutron irradiation of Eurofer97, helium is transmuted from Nickel and Boron. As discussed in section 6.4.1, it is not realistic to expect a 100 % trapping rate in the matrix; He has a low E^m of ~ 0.05 - 0.08 eV [32,33] and will leave the material quickly. The migration of helium is enhanced due to the irradiation temperature. Helium can be retained in the matrix in He_nV_m clusters or in bubbles (bubbles are defined as large helium-vacancy clusters), affecting the mechanical properties of Eurofer97, such as the irradiation hardening. The percentage of helium retention is not known but, with the help of a desorption spectroscopy system, possible to be estimated.

The TDS spectra of neutron irradiated Eurofer97 at 573 K with a dose of 1.9 dpa and 8.0 dpa are shown in figure 6.16 and 6.17, respectively. To obtain the spectra, TEM discs were annealed up to 1600 K, at a rate of 0.33 K/s. Both spectra were obtained without bake-out prior to the measurements.

Chronologically, the first measurement to be performed is the one with the 8.0 dpa irradiated sample, shown in figure 6.17. For this spectrum a sudden increase of helium release is noticed starting at 400 K, reaching a plateau at 600 K. This behavior in helium release was unexpected and thought to be related to poor cooling of the system, at this point done with cool water. A TDS spectrum obtained in the same conditions but with an empty oven (without a Eurofer97 piece inside) is also shown in figure 6.17. The shape of this spectrum (the sudden increase of He release around 400 K) confirms the idea that the cooling conditions available were not enough to obtain a good quality measurement.

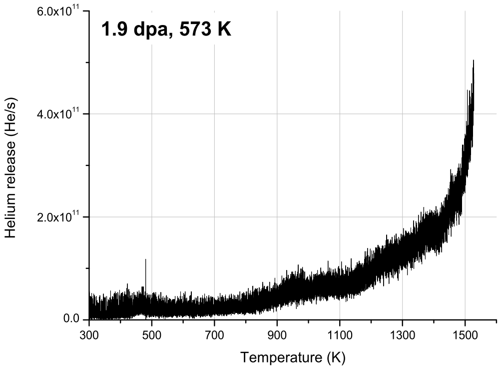

Figure 6.16 *TDS spectrum of neutron irradiated Eurofer97 with 1.9 dpa, 573 K.*

The measurement of the 1.9 dpa sample was done with an additional system cooling of liquid nitrogen. As is seen in figure 6.17, there is no increase of helium release at 400 K.

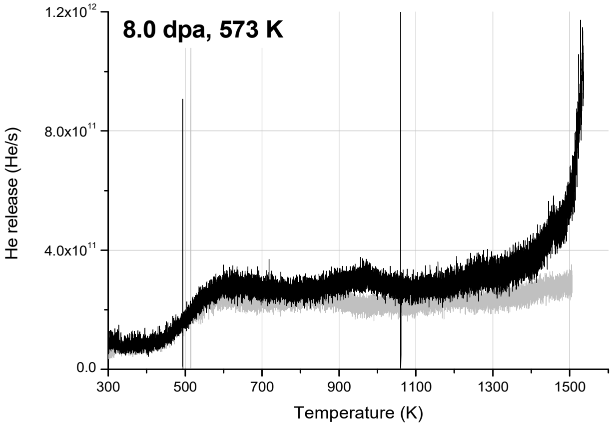

Figure 6.17 *TDS spectrum of neutron irradiated Eurofer97 with a dose of 8.0 dpa, 573 K (in black). In grey: measurement of He release exclusively from the system, without a Eurofer97 piece inside the oven.*

Table 6.7 shows the calculated He content of the 1.9 dpa sample (in terms of concentrations and number of atoms) and the measured number of He atoms desorbed (calculated from the spectra and considering a calibration volume with a known concentration of He atoms). Assuming that all the He measured by the system's quadrupole is related to the release of He from the sample, the amount of desorbed gas is ~ 43 % of the expected amount of the transmuted He. This must be considered as an upper limit since during the measurements the quadrupole sensed peak from hydrogen (related to the humidity present in the system) will partially overlap with from the peak from helium. This reasoning allows the conclusion that less than 43 % of the transmuted helium in Eurofer97 is retained in the sample after neutron irradiation. This conclusion is in accordance to the idea that Eurofer97 is a step forward in the development of radiation resistant structural steels.

Table 6.7 *Relevant He values related to the TDS measurement of the 1.9 dpa, 573 K neutron irradiated Eurofer97.*

Weight of desorbed Eurofer97	5.7 mg
He concentration (appm)	10.5
Absolute number of He atoms in sample	6.5 x 10^{14}
Number of He atoms observed in TDS spectrum	2.8 x 10^{14}

6.5 Conclusions

Eurofer97 was irradiated at three different conditions: 2.4 dpa and 333 K, 1.9 dpa and 573 K, and 8.0 dpa and 573 K. After irradiation, pieces of neutron irradiated Eurofer97 steel were studied with TEM with the goal of identifying the type of defects induced by neutron irradiation and its evolution of with increasing temperature and dose.

For the three irradiation conditions the irradiation induced defects were identified. The TEM investigation of the sample irradiated with 2.4 dpa at 333 K shows black dots as irradiation damage. The irradiation of Eurofer with 1.9 dpa at 573 K reveals the presence of black dots and dislocation loops. The defect sizes measured for the first two irradiation conditions point to the conclusion that the defect size increases with increasing temperature. The increase of defect size is explained by the coalescence of defects and by the aggregation of newly formed Frenkel pairs to existing defects, both phenomena being promoted by the higher irradiation temperature of the irradiation at 573 K.

For the third irradiation condition, 8.0 dpa and 573 K, the defects observed are black dots and dislocation loops. However, for the irradiation at 8.0 dpa the average size of the defects decreases, in comparison to that of the irradiation at 1.9 dpa (both at 573 K). The higher 8.0 dpa dose is proportional to a higher number of formed Frenkel pairs, of which the diffusion is promoted by the 573 K irradiation temperature. Although black dots and dislocation loops are formed, these can decrease their size and/or annihilate due to the diffusion of vacancies and interstitials. For a higher irradiation dose, this effect is stronger.

In order to determine the obstacle strength value of the defects observed with TEM in stopping the dislocation gliding, the increase of yield strength after irradiation was calculated using two methods to determine the inter-obstacle strength: one based on the dispersed barrier hardening model and the other based on the effective inter-particle spacing. The present analysis leads to a consistent description of the evolution of the yield strength of irradiated material. The results indicate that dislocation loops and black dots have a similar effect on the mechanical behaviour, even though the specific character of black dots can still not be identified. In order to evaluate the effect of the size of irradiation defects more detailed observations are necessary, like in-situ observation of the interaction of dislocations with defects during plastic deformation.By plotting the calculated yield strength for various obstacle strength values and comparing the outcome with experimentally obtained hardening values, it is concluded that the effective inter-particle spacing method leads to stable values of the obstacle strength parameter. This observation agrees with the idea that, for the irradiation conditions under discussion, the parameter α is neither dependent on the size of the obstacle (up to a size of 13 nm) nor of the damage level of the sample. For the three irradiation conditions studied, α takes an average fitted value of 0.22.

The presence of He bubbles in the irradiated material was speculated, as these are detrimental for the mechanical properties of Eurofer97. The TEM observations do not reveal the presence of bubbles in Eurofer. Using the ideal gas law, the number of He bubbles expected in a TEM sample was calculated. For the sample irradiated with 8.0 dpa at 573 K, which has the higher transmutation rate, the number of 3.6 bubbles was obtained. Considering that some of the defects trapping helium will dissociate at the irradiation temperature, the lack of bubbles in the TEM observations seems to be correct.

To further investigate the presence of He in the neutron irradiated Eurofer, TDS measurements were carried out using TEM samples. Although the background signal interfered with the measurement of the 8.0 dpa, 573 K sample, it was possible to conclude that for the 1.9 dpa, 573 K sample less than 43 % of the transmuted helium during neutron irradiation is retained. This conclusion is in agreement with the idea that Eurofer97 is a step forward in the development of radiation resistance steels.

Nomenclature

B	Length of the Burgers vector	m
D	Defect diameter	nm
E^m	Migration energy	eV
He	Helium	
l	Inter-obstacle spacing	nm
M	Taylor factor	

N	Defect density	m^{-3}
$N_{1.9}$	Defect density of the TEM sample irradiated at 1.9 dpa	m^{-3}
$N_{8.0}$	Defect density of the TEM sample irradiated at 8.0 dpa	m^{-3}
N_{He}^{bubble}	Number of He atoms present in a bubble	
N_{dpa}	Defect density correspondent to a dose	m^{-3}
P	Pressure of a bubble	Pa
R	Gas constant	J.mole^{-1}.K^{-1}
R	Bubble radius	nm
T_{irrad}	Irradiation temperature	K
T_{test}	Test temperature	K
V	Vacancy	
V	Volume of a bubble	nm^{3}
α	Obstacle strength	
γ	Surface tension	N/m
μ	Shear modulus	GPa
ρ	Projected defect density	m^{-2}
$\Delta\sigma_y$	Irradiation hardening	MPa
ϕ	Dose	dpa
DBH	Dispersed barrier hardening	
DEMO	Demonstration power plant	
dpa	Displacements per atom	
HFR	High flux reactor	
SIA	Self interstitial atom	
TDS	Thermal desorption spectroscopy	
TEM	Transmission electron microscopy	
UTS	Ultimate tensile strength	MPa
YS	Yield strength	MPa

References

[1] M.R. Gilbert, S.L. Dudarev, D. Nguyen-Manh, S. Zheng, L.W. Packer, J.C. Sublet, J. Nucl. Mater. 442 (2013) S755–S760. doi:10.1016/j.jnucmat.2013.03.085.

[2] R.E. Stoller, J. Nucl. Mater. 174 (1990) 289–310. doi:10.1016/0022-3115(90)90242-F.

[3] M.R. Gilbert, S.L. Dudarev, S. Zheng, L.W. Packer, J.-C. Sublet, Nucl. Fusion. 52 (2012) 083019. doi:10.1088/0029-5515/52/8/083019.

[4] J.W. Rensman, NRG Irradiation Testing: Report on 300 °C and 60 °C Irradiated RAFM Steels, 2005. doi:20023/05.68497/P.

[5] N. Luzginova, J.W. Rensman, M. Jong, P. ten Pierick, T. Bakker, H. Nolles, J. Nucl. Mater. 455 (2014) 24–25.

[6] J. Rensman, H.E. Hofmans, E.W. Schuring, J. Van Hoepen, J.B.M. Bakker, R. Den Boef, et al., J. Nucl. Mater. 307-311 (2002) 250–255. doi:10.1016/S0022-3115(02)01036-X.

[7] J. Rensman, E. Lucon, J. Boskeljon, J. Van Hoepen, R. Den Boef, P. Ten Pierick, IJ. Nucl. Mater. 329-333 (2004) 1113–1116. doi:10.1016/j.jnucmat.2004.04.033.

[8] European Comission, High Flux Reactor (HFR) Petten, Characteristics of the installation and the irradiation facilities, EUR 15151E, Comission of the European Communities, 1993.

[9] R. Lässer, N. Baluc, J.L. Boutard, E. Diegele, S. Dudarev, M. Gasparotto, et al., Fusion Eng. Des. 82 (2007) 511–520. doi:10.1016/j.fusengdes.2007.06.031.

[10] P. Vladimirov, A. Möslang, J. Nucl. Mater. 329-333 (2004) 233–237. doi:10.1016/j.jnucmat.2004.04.030.

[11] S.J. Zinkle, A. Möslang, Fusion Eng. Des. 88 (2013) 472–482. doi:10.1016/j.fusengdes.2013.02.081.

[12] M. Kolluri, P.D. Edmondson, N.V. Luzginova, F.A. v. d. Berg, Mater. Sci. Eng. A. 597 (2014) 111–116. doi:10.1016/j.msea.2013.12.074.

[13] R. Konings, ed., Comprehensive Nuclear Materials, 1st ed., Elsevier Ltd, 2012.

[14] P. Fernández, A.M. Lancha, J. Lapeña, M. Serrano, M. Hernández-Mayoral, J. Nucl. Mater. 307-311 (2002) 495–499. doi:10.1016/S0022-3115(02)01013-9.

[15] M. Klimenkov, R. Lindau, E. Materna-Morris, A. Möslang, Prog. Nucl. Energy. 57 (2012) 8–13. doi:10.1016/j.pnucene.2011.10.006.

[16] C. Dethloff, E. Gaganidze, J. Aktaa, J. Nucl. Mater. 454 (2014) 323–331. doi:10.1016/j.jnucmat.2014.07.078.

[17] J. Jonnet, P. Van Uffelen, T. Wiss, D. Staicu, B. Remy, J. Rest, Proc. Fourteenth Int. Conf. Radiat. Eff. Insul., 2008: pp. 3008 – 3012.

[18] C. Onofri, C. Sabathier, H. Palancher, G. Carlot, S. Miro, Y. Serruys, et al., Nucl. Instruments Methods Phys. Res. Sect. B Beam Interact. with Mater. Atoms. In Press (2015). doi:10.1016/j.nimb.2015.08.091.

[19] A.D. Whapham, B.E. Sheldon, Philos. Mag. 12 (1965) 1179–1192.

[20] R.E. Stoller, S.J. Zinkle, J. Nucl. Mater. 283-287 (2000) 349–352.

[21] G. Was, Fundamentals of Radiation Materials Science, Springer Berlin Heidelberg,

2007.

[22] G.E. Lucas, J. Nucl. Mater. 206 (1993) 287–305. doi:10.1016/0022-3115(93)90129-M.

[23] T. Zhang, C. Vieh, K. Wang, Y. Dai, J. Nucl. Mater. 450 (2014) 48–53. doi:10.1016/j.jnucmat.2013.12.007.

[24] R. Lindau, A. Möslang, M. Rieth, M. Klimiankou, E. Materna-Morris, A. Alamo, et al., Fusion Eng. Des. 75-79 (2005) 989–996. doi:10.1016/j.fusengdes.2005.06.186.

[25] E. Gaganidze, C. Petersen, E. Materna-Morris, C. Dethloff, O.J. Weiß, J. Aktaa, et al., J. Nucl. Mater. 417 (2011) 93–98. doi:10.1016/j.jnucmat.2010.12.047.

[26] E. Gaganidze, C. Dethloff, Quantitative TEM investigation of neutron irradiated EUROFER97 from WTZ and ARBOR1 Objectives for Work Programme 2012, (2012).

[27] E. Gaganidze, J. Aktaa, Fusion Eng. Des. 88 (2013) 118–128. doi:10.1016/j.fusengdes.2012.11.020.

[28] O.J. Weiß, E. Gaganidze, J. Aktaa, J. Nucl. Mater. 426 (2012) 52–58. doi:10.1016/j.jnucmat.2012.03.027.

[29] R. Schäublin, J. Henry, Y. Dai, Comptes Rendus Phys. 9 (2008) 389–400. doi:10.1016/j.crhy.2008.01.003.

[30] R.L. Klueh, a. T. Nelson, FJ. Nucl. Mater. 371 (2007) 37–52. doi:10.1016/j.jnucmat.2007.05.005.

[31] F.F. Charpin, SUMO 320-11 - Nuclear Analysis, 2007. doi:21642/07.80606/I.

[32] K. Morishita, R. Sugano, B.D. Wirth, J. Nucl. Mater. 323 (2003) 243–250. doi:10.1016/j.jnucmat.2003.08.019.

[33] K. Morishita, R. Sugano, B.D. Wirth, T. Diaz de la Rubia, Nucl. Instruments Methods Phys. Res. Sect. B Beam Interact. with Mater. Atoms. 202 (2003) 76–81. doi:10.1016/S0168-583X(02)01832-3.

Acknowledgements

When I was a child I wanted to be a shepherd, obviously. Every time I saw one, whether it was in a painting or a movie, they were sitting under a tree, chewing on some straw and reading a book. And as a child, all I wanted to do was to read books. Whichever book I could grab, I would read. All-day-long. So whenever the topic came up with my parents, grandparents or extended family, I was more than willing to share my dream job. Then, as now, my family always made me feel like I could do *whatever I set my mind to*. Although my life goals have changed since that time, the love, care and support I got from my family has never stopped. And for that I would like to thank them very much.

In 2009 I attended CERN as a summer student. Well, I will keep it short and sweet by saying there were parties, lots of them. And this is where I met Menno. Some people are lucky enough to fall in love and I am one of them. I've met someone who is as happy with instant-noodles as with fancy restaurants. Who often makes me laugh until I cry. Who respects and praises me for exactly who I am and by whom I feel the same. Without Menno, I would have doubted the whole PhD idea many more times than I did. For that and much more I say thank you, Menno. Living wouldn’t be as much fun without you.

Supervision is essential for successful PhD research. As a PhD student you have the freedom to set your own path, but good advice is invaluable along the way. That said, the day I met Henk is one I will never forget. Our meeting was scheduled to be in the morning but I had to print something at a shop near the Delft’s train station. I decided to go there without a map, thinking 'how hard could it be to find my way back to TUD'. By the time I was finished I was running late and I had to run to RID. Now, let me tell you something about the Reactor Institute Delft: no one knows where it is. Against all odd I managed to reach TUD without a map and, by what I now know to be the Aula, I asked a student if he could point me the way to the Reactor Institute Delft - "I have no idea where that is", he said. After a few more similar answers I finally found someone who would tell me to keep on walking straight ahead for 20 min until I reached the end of the street (RID is pretty much isolated from the other buildings). And so I ran. And worried about being *VERY* late for my first in person interview. And ran some more. Finally I met Henk who, when I apologized for appearing more than 30 minutes late, responded with a simple "oh, it's ok, many people can't find RID" and put an end to my worries. So simple, so eloquent, and after so much running. During the first two years of research I was mostly under Henk's supervision. Throughout that period I found out first hand that Henk is an excellent and gifted teacher. He will try his absolute best to make you understand. Positron annihilation is not an easy topic but you, Henk, managed to make me understand the basics of it. For that and for giving me guidance through this research you have my gratitude and acknowledgement. A big thank you, Henk.

In the same day, I met Jilt. I could say lot about how kind you were, showing me the research you did, asking me about mine, but what stuck in my mind the most was the ringtone of your phone, which rang sometime during the visit to the 3mE labs. To be honest I forgot which song it was exactly, but I recall it was a well-known rock song and that I was very pleased we shared our taste in music. Although our closest contact was during the last two years, when the pressure to write the thesis was high and I had a stream of questions about the mechanical properties of materials, you have always kept a sharp eye on the work as a whole and gave me some good advice, both work related and not. I see in you the qualities of a leader and I hope that one day I can be as wise as you are. Thank you for being supportive, thank you for answering my infinite amount of questions and thank you for leading me towards a successful finishing of the PhD. Jilt, a sincere thank you.

A few days later I visited NRG and met Natalia and Sasha. While for the other interviews I was asked about my master thesis work, here I was asked about what I could predict of the TDS measurements that I would be doing on irradiated steel. And I had no idea about that. Fortunately Natalia and Sasha already had some good ideas of how things would go and could shed some light on it. The conversation went on and later I was allowed to try to manipulate some (empty!) capsules in the cells of the HCL, which I thought was the coolest thing. By the end of the day I was very much looking forward to being accepted for the position - I wanted to see things as you did and perhaps even try the manipulators again.

Natalia, it has been a pleasure working with you. Not only do you never cease to amaze me with your knowledge regarding everything fusion energy related, you are always incredibly straight forward, not hesitating to say ‘I do not know that’ or ‘you are not being clear at all’. I highly value these are characteristics of yours and I would like to have for myself. Thank you for all the support, even after you left you managed to find some time for my questions.

Sasha, with you I have travelled around Europe to attend EFDA meetings. Firstly, thank you for inviting to attend those meetings, where I could extend my knowledge regarding fusion related research, and for trusting me to present my work there. This was very important to build confidence in myself, my work and to polish my presentation skills. Plus, the dinners after the meetings were often great and we even shared some more exciting times, such as when the hotel we were staying at in Slovenia was on fire (no one got hurt, but we did have to evacuate at 3am). Besides all this, you have helped me in two transitional periods: when I started to work at NRG and during the dark period of late 2013. Both times you have helped me to make the most out of it. Thank you for the support.

Other than my supervisors, many others were instrumental to bring this research to its successful end. One can read a million of articles about the topic in question, but when the turbo pumps fail, when the electronics are not working and when the electron beam of the microscopy suddenly shuts down, who can help solving the problem swiftly and sharply? Well, if you worked at RID when I did I would recommend talking to Jan de Rood and Freek Labohm. Both of them were invaluable helping me with the plasma implantations, the positron beam and the TDS. Thank you for all your patience and quick responses! Also at NRG I also had some incredible help. I would like to warmly thank Frans van de Berg, Marcel Stijkel, Aad van Lierop, Paul Lameree and Norman Schalk. All of you have helped me so much! I could always go to you with all sorts of technical problems and you would (almost) always find an answer or an alternative. Thank you.

As it is clear by now, my time was divided between RID (2011- 2012) and NRG (2013-2015). Doing a PhD is much more than doing research - the environment and the people around you matter greatly. From the RID side, a special thanks goes to Romain Blondé, José Leitão, Shasha Zhang, Yibole Hargen, Fenqjiao Qian, Miao Xue-Fei, Anca Anastasopol, Anton Lefering and Jimmy Melskens. Anca stood out from this group and became a very close friend. With her I shared an average of 30 min per week sitting on a sofa by an RID window, looking at the traffic and talking about whatever would cross our minds. Plus, when she was pregnant and we were travelling, it was fun to help her skip the lines and quickly get a table at restaurants. Anca, thank you for listening, for caring and for sharing.

During my time in Delft I also attended a master course where I met two great, positive and cheerful master students: Julia Stikkelman and Pieter Burgel. I'm grateful to have met you, thank you!

Besides these colleagues, I would like to thank the FAME and NPM2 groups, as well as the secretaries Ilse van der Kraaij and Nicole Banga. Although we were working on different topics, it has nice to have a coffee pause and cake with you. Thank you all.

As I've mentioned, my time at NRG was not always bright and sunny. In 2013 the lab were I was working had to close for safety improvements and the working force had to be reduced. This moment had a deep impact on me. Even so, the people at building 420 made it enjoyable to keep on going back to work. To cite a few, but being entirely sure I am forgetting others, I would like to thank Arjan Vreeling, Bouke Jonker (thank you for always finding the money!), Liesbeth van Dompselaar, Gael Ménard, Frank Oud, Frans van de Berg, Jessica Bruin, Lida Magielsen, Murthy Kolluri, Arjan de Jong, Ralph Hania, Monica Jong, Henk Nolles, Steven Knol, Tjark van Staveren, Maurits Heijna, Frodo Klaassen, Willem Molijn, Tien Pham, Paul van Idsert, Pieter ten Pierick, Theo Bakker, Aad van Lierop, Marcel Stijkel, Sander van Til and Oene Zwaagstra. A sincere thank you to all.

Here I must take a moment to acknowledge Frans and Murthy in particular. Since Frans taught me everything I know about how to use the TEM, we ended up spending many hours together. Frans, being kind as he is, was always in a good mood which made working with him so much more enjoyable. Murthy was my office mate for little over a year. This ended up being great: not only could we talk about work related topics, but because he was further on with his career and life I could ask him advice on all sorts of topics. Frans, Murthy, thank you for everything.

Truth be told, my first PhD related contact was with M2i. Monica Reulink was the kind voice on the phone who promised me to try to match my CV with one of the vacancies available at M2i. It really did cause an positive impression that my first contact was someone so open and ready to help. Later on, I met Gitty Bouman, Marjolein Blankstein, Briggite van Uden and Janneke Curovic, people that I could always go to when help was needed. A big thank you to all the ladies. Also from M2i, I would like to thank Irina Bruckner - thank you for the excellent advice in a tough situation. However, this paragraph cannot end without me saying a big thanks to all the M2i people, including the colleagues from other research clusters. It was great being a part of the group, thank you for having me.

It wasn’t (and I fear that it will never be) easy to be away from my family and what I have known as home for so long. That said, I would like to thank Menno’s family, his friends ─ Daan, Rojan, Zsuzsu and Lotte ─, and the friends I managed to make in the Netherlands ─ Anca, Nicoleta and Paula ─, for giving me a home away from home. Thank you so much. Your kindness means a lot to me.

Inês

Curriculum vitae

02/2011 – 09/2016 **PhD Material Science / Applied physics**

Steels for fusion reactors: Eurofer97

Supervision: Prof. J. Sietsma, Dr. H. Schut, Dr. A. Fedorov, Dr. N. Luzginova

12/2013 **International School in Nuclear Engineering**

- "Course 4 – Materials for Nuclear Reactors, Fuels and Structures", Saclay Nuclear Research Centre (CEA), Gif-sur-Yvette, France

09/2011 **Ion irradiation Workshop**

- Department of Materials, University of Oxford, United Kingdom

04/2011 **Health physics level 5B**

- Diploma for safe handling of radioactive sources and radiation producing equipment with a limited radiation risk

09/2005 – 12/2010 **Master of Science (Msc.) in Physics Engineering**

University of Aveiro, Portugal

- Master thesis: material growth and characterization techniques, "Study of structural and magnetic properties of thin films of LaBaMnO3 grown in different substrates by sputtering technique"
- 3rd year project partially developed at ISOLDE / CERN (Switzerland) – implantation of ^{111}Cd radioactive isotopes in manganites thin films, *Hyperfine Interactions in Manganites*

Attendance of international schools, including:

- ERASMUS Intensive Programme "Eng. and Characterisation of Nanostructures by Photon, Ion Beam and Nuclear Methods", Rheinische Friedrich-Wilhelms-Universität (2009), Germany
- CERN Summer School (2009), Switzerland

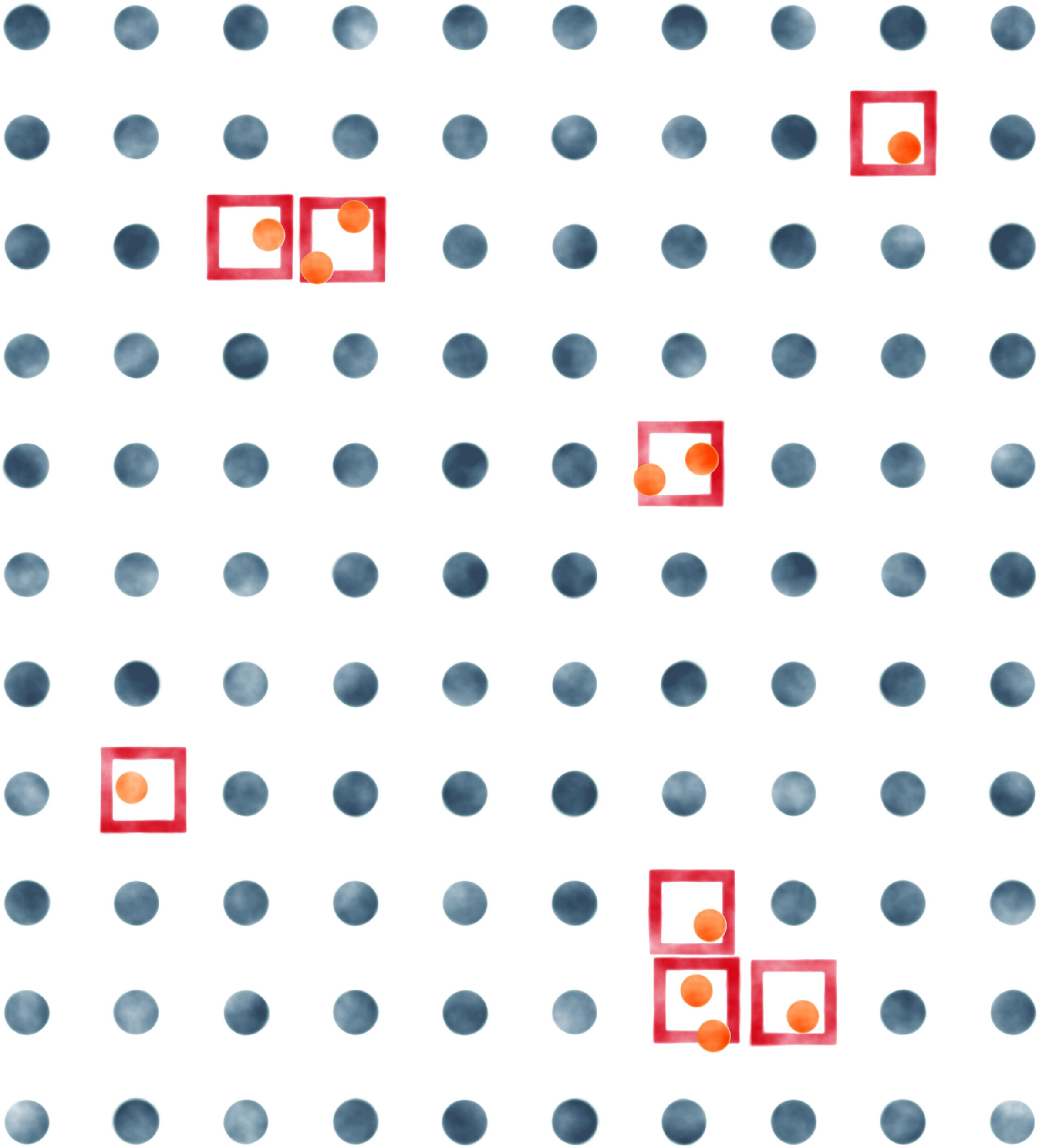

ISBN 978-94-91909-40-5